SPECIAL REPORT 96-27

Glaciers, Ice Sheets and Volcanoes: A Tribute to Mark F. Meier

Samuel C. Colbeck, Editor

October 1996

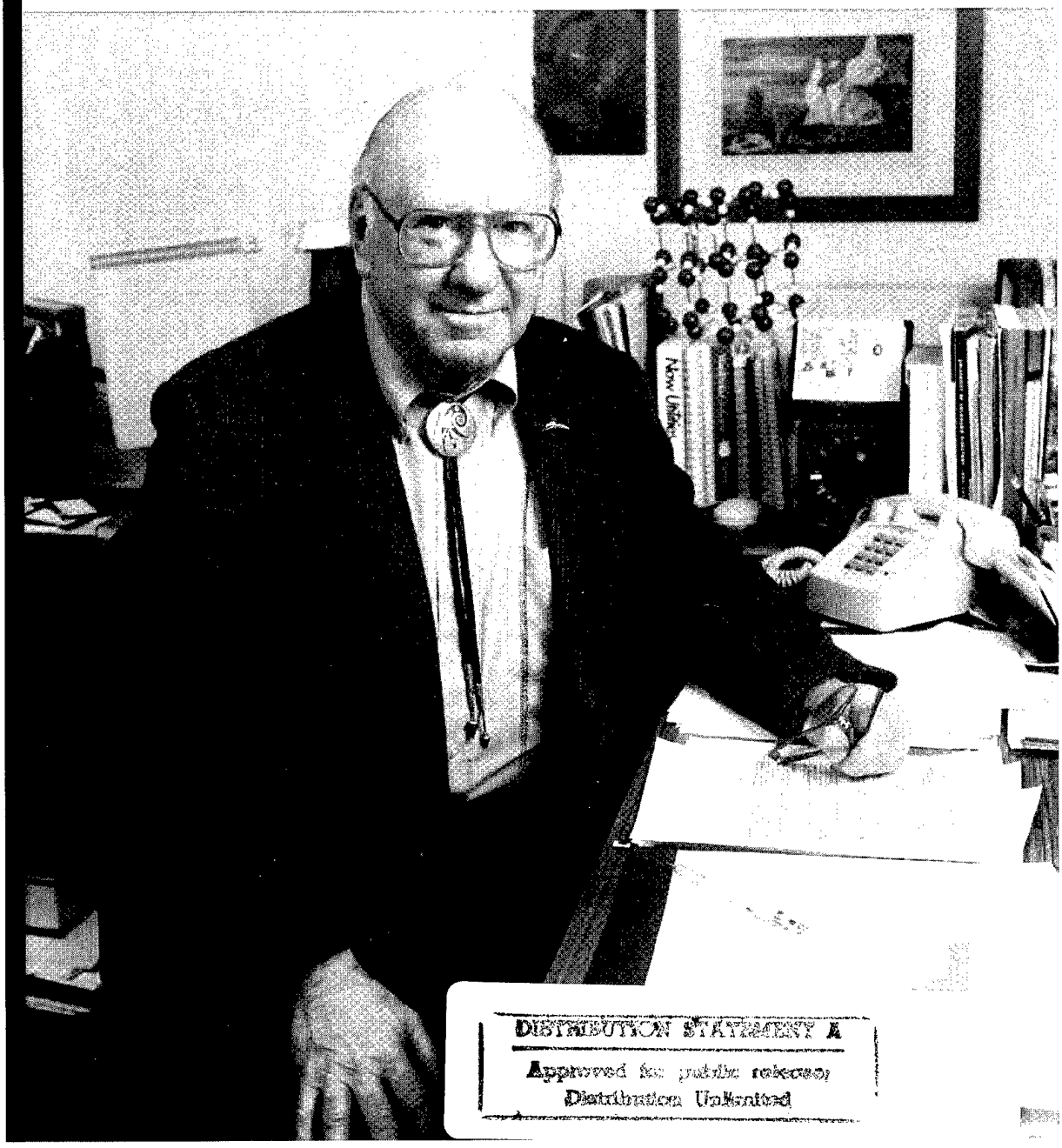

Abstract: This volume is dedicated to the professional contributions of Mark Meier. It contains a mixture of papers on snow, glaciers, ice sheets and volcanoes, and therefore reflects his interests and research contributions. The papers were presented at the 1995 Fall Meeting of the American Geophysical Union.

Cover: Photograph by Ken Abbott, University of Colorado.

How to get copies of CRREL technical publications:

Department of Defense personnel and contractors may order reports through the Defense Technical Information Center:

DTIC-BR SUITE 0944
8725 JOHN J KINGMAN RD
FT BELVOIR VA 22060-6218
Telephone 1 800 225 3842
E-mail help@dtic.mil
msorders@dtic.mil
WWW http://www.dtic.dla.mil/

All others may order reports through the National Technical Information Service:

NTIS
5285 PORT ROYAL RD
SPRINGFIELD VA 22161
Telephone 1 703 487 4650
1 703 487 4639 (TDD for the hearing-impaired)
E-mail orders@ntis.fedworld.gov
WWW http://www.fedworld.gov/ntis/ntishome.html

A complete list of all CRREL technical publications is available from:

USACRREL (CECRL-TL)
72 LYME RD
HANOVER NH 03755-1290
Telephone 1 603 646 4338
E-mail techpubs@crrel.usace.army.mil

For information on all aspects of the Cold Regions Research and Engineering Laboratory, visit our World Wide Web site: http://www.crrel.usace.army.mil

DISCLAIMER NOTICE

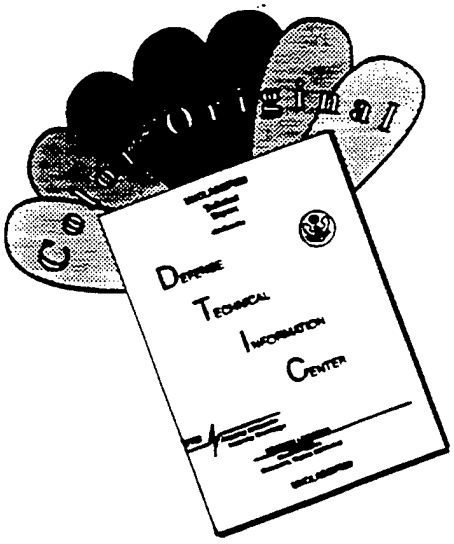

THIS DOCUMENT IS BEST QUALITY AVAILABLE. THE COPY FURNISHED TO DTIC CONTAINED A SIGNIFICANT NUMBER OF COLOR PAGES WHICH DO NOT REPRODUCE LEGIBLY ON BLACK AND WHITE MICROFICHE.

Special Report 96-27

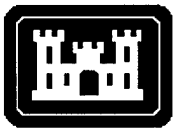

U.S. Army Corps of Engineers
Cold Regions Research & Engineering Laboratory

Glaciers, Ice Sheets and Volcanoes: A Tribute to Mark F. Meier

Samuel C. Colbeck

October 1996

FOREWORD

These papers were among those presented at special sessions at the 1995 Fall Meeting of the American Geophysical Union in honor of Mark Meier. The tribute to Mark was made in recognition of his many contributions to glaciology and of his personal involvement in the development of both the science and the scientists over more than 40 years. Like many others, I enjoyed the benefit of his support at an early stage in my career when it mattered the most to me personally and to the achievement of the work that I was pursuing.

Mark grew up in an academic environment in Iowa, and received his first degree there, in Electrical Engineering. He soon entered glaciology, however, completing a masters thesis on the glaciers in the Wind River Range in Wyoming before moving on to Cal Tech and the world of Bob Sharp. This led to the production of a classic piece of field work in glaciology, *The Mode of Flow of Saskatchewan Glacier, Alberta, Canada,* which is still one of the defining studies of the basic characteristics of glaciers. Upon completing his studies and a Fulbright in Innsbruck to work with Friedl Hoinkes, he established the USGS Project Office—Glaciology in Tacoma, Washington, and a field station on the South Cascade Glacier in the northern Cascades. This provided a new direction to his work, since this simple glacier was chosen for research on glacier–climate interactions and hydrology, as well as glacier dynamics, and a staff was recruited for broad studies of this glacier and, by extension, snow and ice in the Northwest. He established other sites in California and Alaska, and brought in Austin Post who documented the status of glaciers by aerial photography throughout this huge area.

In these same years, Mark established himself as an internationally recognized figure in the world for both his contributions to glaciology and to the profession as a whole. He became involved with organizations like the International Commission on Snow and Ice, became its president and then became the only glaciologist to head its parent organization, the International Association of Hydrological Sciences. While heading an office dedicated to glacier studies in the Northwest, he expanded his scientific interests to include remote sensing of the snow cover, represented the USGS in areas of natural hazards in the Northwest, especially the ice-on-volcanoes problem, and helped develop the glaciology option in the Geophysics Program at the University of Washington. Mark and his Tacoma team organized field and model studies of the Columbia Glacier, Alaska, to allow the first quantitative understanding of the dynamics of an iceberg-calving glacier, and successfully predicted its sudden retreat. Before completing his service with the USGS, Mark began an interest in the role of glacier retreat on sea level, which continues to this day.

It would be remarkable if some one with such a record did not serve on a number of committees and panels, but Mark may be the only one who represented the interests of the snow and glacier communities simultaneously. He served on the Academy committee that defined the Global Change Program, and, more recently, on the Intergovernmental Panel on Climate Change.

Mark was recruited in 1985 to direct the Institute of Arctic and Alpine Research at the University of Colorado, where he pursued his interests in glaciers and climate, sea-level change, and iceberg calving, as well as new initiatives such as the fate of melting water on cold ice sheets. In 1994 he stepped down as Director, but remains a member of the faculty and now has more time to pursue his research interests.

Sam Colbeck

The Effect of Mark Meier on Tidewater Glaciers

ANDREW G. FOUNTAIN
U.S. Geological Survey, PO Box 25046 MS-412, Denver, CO 80225

Mark Meier is the leading authority on the dynamics of tidewater glaciers and has authored a relatively large fraction of reports currently (1995) published on the subject. Despite this detailed examination of tidewater glaciers, one important process has been overlooked—the effect of Dr. Meier himself on the retreat of tidewater glaciers. I believe this effect to be significant, although the reasons remain elusive. Figure 1a shows the relation between Meier's initial presence at the glacier and the change in length (retreat) of the glacier. I concede that the initiation of annual variations in the retreat and advance of Columbia Glacier may be the result of sampling rate and not that of Meier's presence. However, the drastic retreat of the glacier several years later does seem unusually concidental.

A more definitive field test of Meier's presence occurred in 1985, when Dr. Meier retired from the U.S. Geological Survey, thus terminating his study of Columbia Glacier. As Figure 1b shows, the drastic retreat of Columbia Glacier ceased and the glacier resumed its former annual cycling of retreat and advance. In 1987, Meier resumed his studies of Columbia Glacier from his new position with the Institute of Arctic and Alpine Research at the University of Colorado. As can be seen in Figure 1b, Columbia Glacier reentered its drastic retreat, which continues at this present time.

The correlation with the presence–absence of Dr. Mark Meier and the rate of retreat of Columbia Glacier is quite compelling. The ratio of Dr. Meier's mass and volume to that of the glacier, although not constant, is insignificant (<10–10). Although we do not yet understand the physical principles underlying the effect of Mark Meier, modelers should consider adapting to their calving boundary condition a kronecker delta function to account for the presence–absence of Mark Meier. The implications of this conclusion are profound and of immediate importance. Should Dr. Meier be allowed to visit the ice streams of the Antarctic and Greenland?

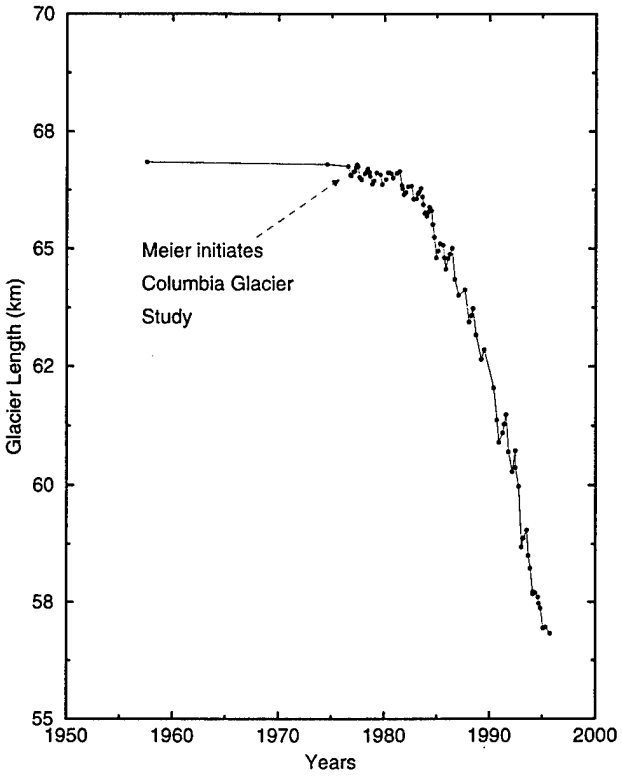

a.

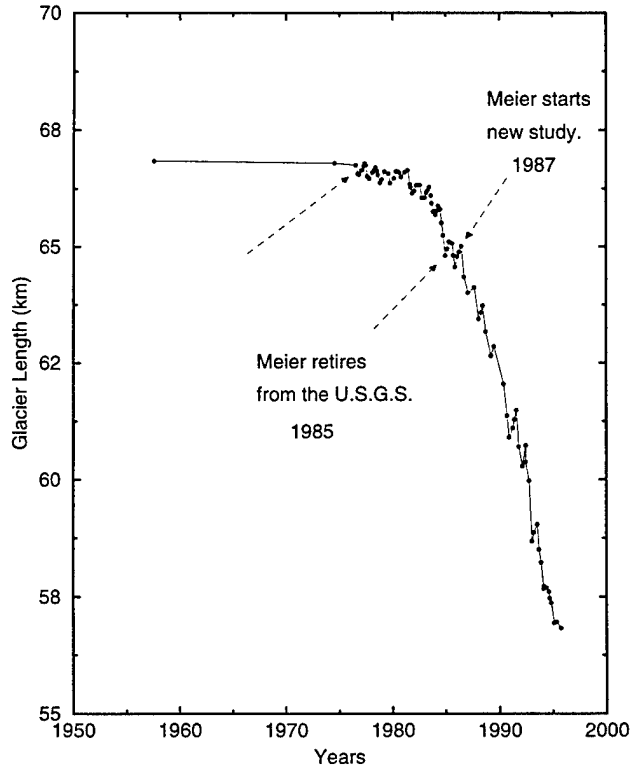

b.

Figure 1. Retreat of Coliumbia Glacier.

CONTENTS

Properties and Processes Affecting Sublimation Rates in Layered Firn

MARY R. ALBERT
U.S. Army Cold Regions Research and Engineering Laboratory
Hanover, NH 03755

INTRODUCTION

The sublimation of snow and firn is driven by the local meteorology, but it is also affected by the physical characteristics of the snow and the nature of the transport processes within the snow. It is well known that forced air flow can greatly increase mass transfer rates, when compared with diffusion, in processes such as evaporation, condensation, and sublimation. It is likely that ventilation of snow (air flow through the snow itself) will have an effect on sublimation rates for glaciers and other snow masses. In addition, the layered nature of snow and firn controls many of the physical processes that occur in the near-surface firn, including vapor transport and sublimation rates. This paper briefly discusses some recent results on ventilation of layered snow and presents implications for vapor transport rates in snow. Field measurements of permeability obtained at Summit, Greenland, in the summer of 1995 are presented. These values are used in model calculations of air flow through layered snow to examine the effect of layering on air flow rates, and it is shown that channeling (increased horizontal and net air flow within a layer) can occur even if the microstructure of the layer is isotropic. A surface wind pack can greatly reduce the air flow velocities in the underlying firn, yet significant subsurface flow can still occur. Air flow rates greatly affect sublimation rates.

FIELD MEASUREMENTS

Field measurements of permeability, stratigraphy, grain size, and density were made at Summit, Greenland, in the summer of 1995. Permeability is the key parameter that controls the amount of air that can flow through snow or firn. Permeabilities were measured by cutting a sample of snow or firn in a cylindrical sampler (Shimizu 1970), then pumping air through the sample while measuring flow rates and pressure drops using the method described by Chacho and Johnson (1987). Darcy's law is used to infer permeability from measured air flow rates and pressure drops.

Permeability and density measurements taken in the top 3 m are shown in Figure 1. These measurements were taken on vertical firn samples, and the lengths of the lines in the figure represent the thickness of the sample; in some instances, the sample encompasses more than one layer. It is evident that the permeability varies by at least a factor of ten over the top 3 m, with the surface wind pack in general having much lower permeability than the underlying firn. In general the permeability does not follow the firn density profile, but is closely tied to the geometry of the pore space. In model results discussed below, a "mesoscale" layering is considered. The current year's accumulation (top 0.6 m) is considered one layer with permeability 8×10^{-10} m^2, as depicted in Figure 1. Underlying layers adopt higher representative permeabilities, as shown in the figure.

MODEL RESULTS

A two-dimensional finite element model (Albert and McGilvary 1992, Albert, in press) is employed to simulate multidimensional air flow through porous media with adective and diffusive heat and mass transfer. For the simulations presented here, a steady sinusoidal surface pressure forcing is used, with amplitude 5 Pa and wavelength 3.3 m for the surface boundary condition. The amplitude and wavelength fall within the range of those measured over sastrugi at the site. Figure 2 shows typical air flow vectors for uniform firn attributable to the sinusoidal surface pressure forcing.

To investigate layering effects, the model was run with three different assumptions on the firn permeability: the first run assumed a uniform permeability equal to the measured permeability representative of the surface wind pack (8×10^{-10} m^2),

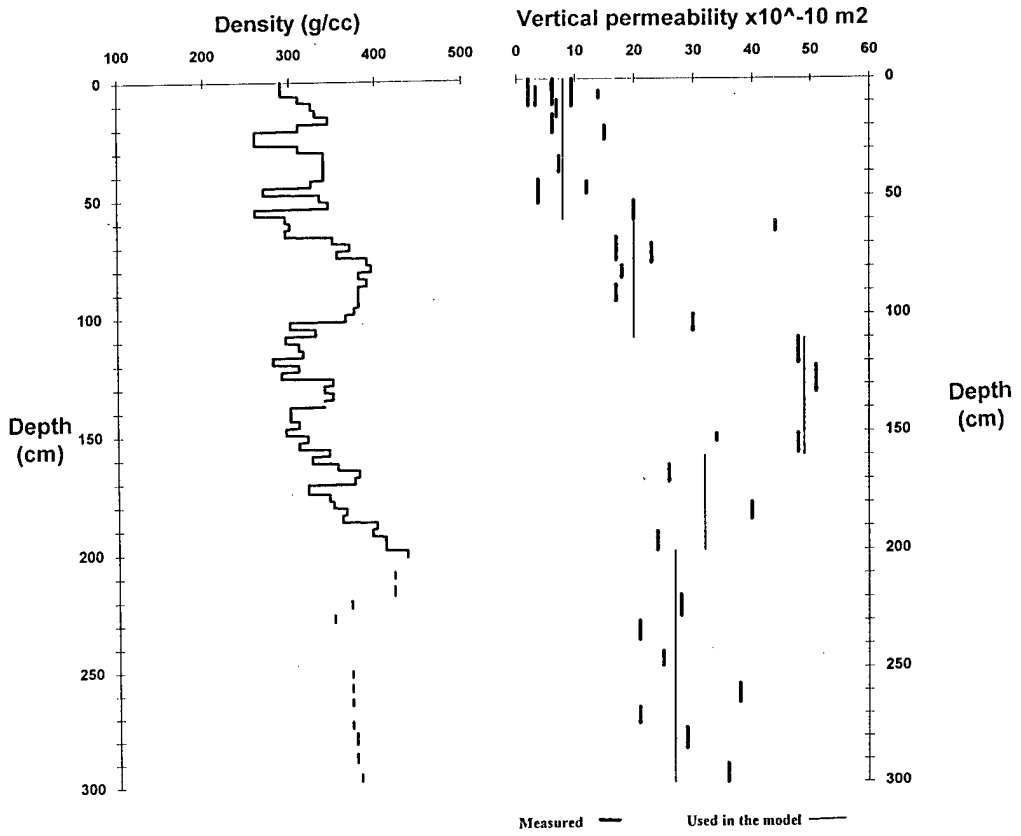

Figure 1. Measured density and permeability in the top 3 m of firn at Summit, Greenland.

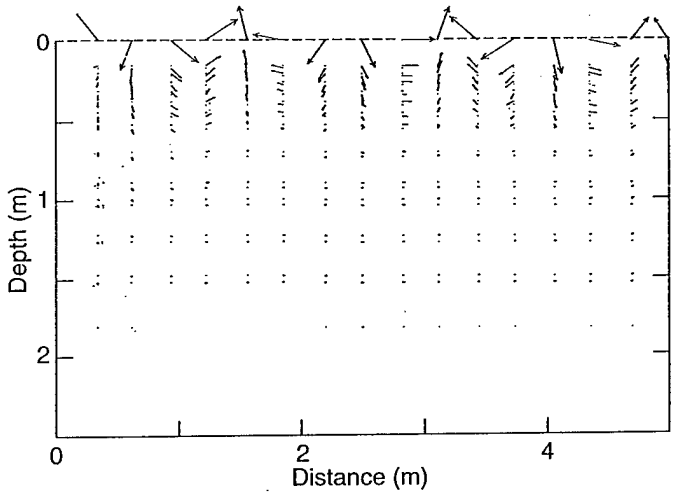

Figure 2. Typical air flow vectors through uniform snow resulting from a sinusoidal surface pressure forcing.

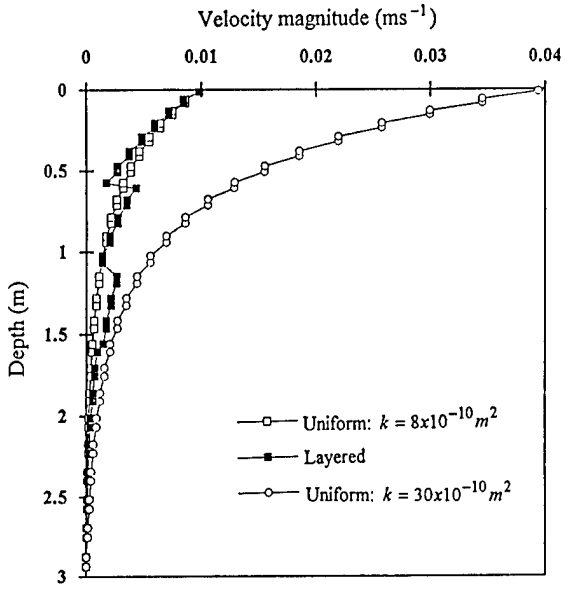

Figure 3. Calculated air flow velocity magnitudes through uniform and layered snow, exhibiting channeling in buried layers of higher permeability.

the second assumed layered permeabilities as in Figure 1, and the third assumed uniform permeability representative of the entire top 3 m (30×10^{-10} m^2). In Figure 3 the calculated air flow velocities are shown as a function of depth for the three cases. The results show that the surface windpack can greatly reduce the air flow velocities in the underlying firn, compared to a situation where the permeability is assumed to be homogeneous and equal to a "representative" value for the entire top 3 m.

It is also evident from Figure 3 that velocities in a more-permeable buried layer can be higher than in the less-permeable layer that lies above it, as evidenced by the rises in velocity magnitudes at depths between 0.6 and 1.1 m, and between 1.1 and 1.6 m. Thus, channeling (increased horizontal and net air flow within a layer) can occur even if the microstructure of that layer is isotropic. Variations in permeability allow variations in flow. This effect is most pronounced for a steady-state surface pressure forcing, and so would most likely occur in the field when winds are sustained. At Summit and many other polar sites, once windy conditions develop they can last for days. Although the surface features such as sastrugi migrate over periods of days, they generally make up the top 10 cm or so of snow; the more permeable layers involved with channeling here do not move in time. Further discussions can be found in Albert (in prep.).

Work is underway to incorporate ventilation effects in the sublimation modeling. In calculations of air flow through a single layer, preliminary work shows a possible increase in sublimation rates ascribable to ventilation several times larger than those calculated from standard diffusion modeling. This effect is depicted in Figure 4. The air flow velocities in this figure are very modest compared to typical velocities calculated very near the snow/air interface, and so it is possible that sublimation rates could occur that are much higher than shown in the figure.

CONCLUSIONS

Although neglected in previous models of wind pumping, layering of snow and firn is important for transfer processes. Summer field measurements at Summit, Greenland, show permeability variations by at least a factor of ten over the top 3 m, with the surface wind pack having lower permeability than the underlying firn. Channeling, or increased air flow in a buried layer, can occur even if the microstructure of each layer is assumed to be isotropic. A surface wind pack can greatly reduce the air flux in the underlying firn, yet significant subsurface flow can still occur. Ventilation

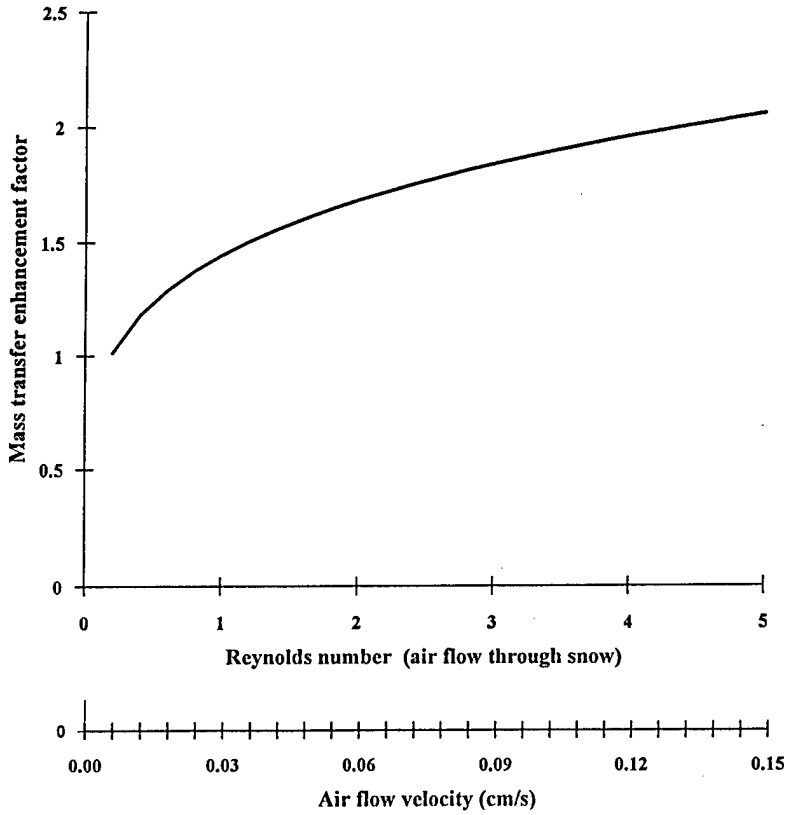

Figure 4. Theoretical increase in mass (vapor) transfer rate in the firn attributable to ventilation.

affects mass transfer, and may be important in sublimation of snow masses and glaciers.

LITERATURE CITED

Chacho, E.F. and J.B. Johnson (1987) Air permeability of snow. *EOS Trans. AGU 68*, 1271.

Albert, M.R. and W.R. McGilvary (1992) Thermal effects due to air flow and vapor transport in dry snow. *Journal of Glaciology*, **38**(120): 273–281.

Albert, M.R. (in press) Modeling heat, mass, and chemical species transport in polar firn. *Annals of Glaciology*.

Albert, M.R. (in prep) Layering effects on ventilation and transfer processes in polar firn.

Shimizu, H. (1970) Air permeability of deposited snow. *Contributions from the Institute of Low Temperature Science, Hokkaido University, Sapporo, Japan*, **A** (22): 1–32.

A Comparison of Passive Microwave Techniques for Detecting Snowpack Melt on the Greenland Ice Sheet

MARK R. ANDERSON
University of Nebraska–Lincoln

THOMAS MOTE
University of Georgia

WALEED ABDALATI
CIRES, University of Colorado

INTRODUCTION

Snowpack melt occurrences detected using passive microwave data have been used to examine climate variability on the Greenland ice sheet. This study compares two techniques to detect snowpack melt using passive microwave data. The first approach (Mote and Anderson 1995) uses thresholds of 37-Ghz, horizontally polarized brightness temperatures to determine when melt is occurring. The thresholds vary by grid cell and are a function of the spring brightness temperatures. Observed brightness temperatures are compared to modeled brightness temperatures associated with the onset of melt. The second method (Abdalati and Steffen 1995) uses a cross-polarized gradient ratio (XPGR), which is the normalized difference of the 19-Ghz, horizontally polarized, and the 37-Ghz, vertically polarized brightness temperatures. Abdalati and Steffen (1995) determined a threshold for the XPGR from field observations. Thresholds chosen for both methods corresponded to a 1% liquid water content in the snowpack.

The comparison was conducted for the entire Greenland ice sheet using orbital SSM/I brightness temperatures from 1990. To maintain consistency, the orbital data were gridded into morning and afternoon passes and then into a daily composite. The same mask was used to exclude land and water areas near the ice sheet margin. Orbital SSM/I brightness temperatures from 1993 were compared with surface observations and energy-balance model results from Dye 2.

RESULTS

The results of this study indicate strong correlations between the daily spatial extent of surface melt (melt area) identified by the two methodologies using the gridded brightness temperatures. The melt occurrences identified by the two approaches were generally similar in both extent and duration (Fig. 1 and 2). However, some differences between the techniques were observed (Fig. 3). The XPGR approach (Abdalati and Steffen 1995) produces a slightly higher overall melt area than the single-channel technique (Mote and Anderson 1995) when the melt areas are accumulated over the entire season, 1.34 and 1.17×10^8 km^2, respectively. Time series of daily melt area for both approaches (Fig. 4) and the differences between the approaches (Fig. 5) were also generated. The single-channel approach indicates more daily fluctuations than the XPGR approach. This difference is most likely attributable to the stronger dependence of the 37-GHz channel used in the single-channel approach on liquid water in the top few centimeters of the snowpack. During the end of the season, the XPGR approach indicates more melt.

A difference in the timing of the snowpack melt between the two approaches is also apparent. The two time series of daily melt area were cross-correlated with lags of 1 to 10 days. The highest cross-correlation between the time series was with the single-channel approach, leading the XPGR approach by 7 days (Fig. 6). The cross-correlation coefficients are:

1. No adjustments to either time series, $r = 0.64$;
2. The single-channel approach lagged seven days, $r = 0.75$;
3. The single-channel approach lagged 7 days and smoothed with a 10-day centered moving average, $r = 0.84$.

Although a lag is clearly present between the time series, it appears that the lag develops during the melt season. During May and June there is very little lag between the time series, but a lag becomes very apparent in July and August. The

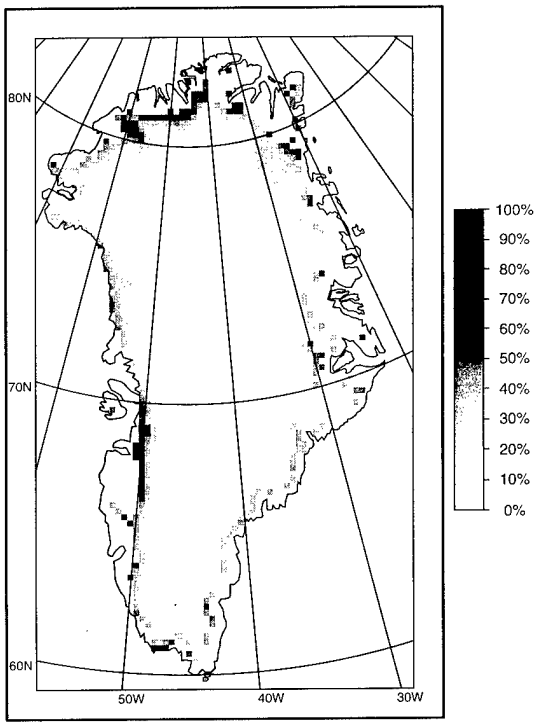

Figure 1. Frequency of melt (in days) identified by the single-channel approach.

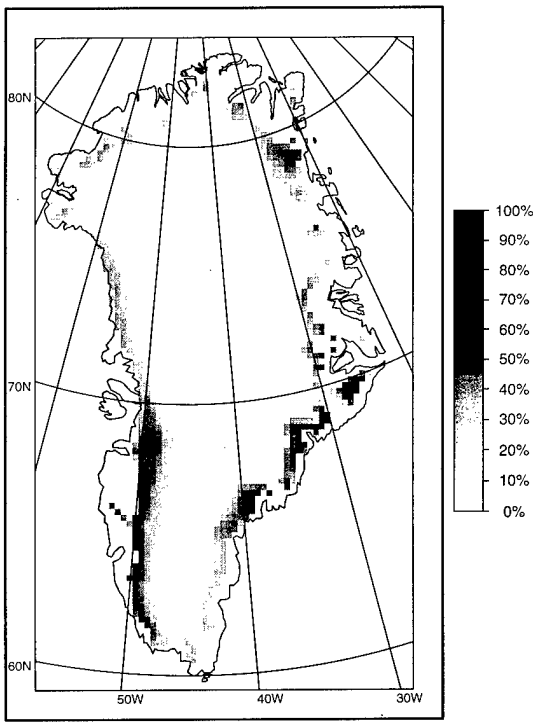

Figure 2. Frequency of melt (in days) identified by the XPGR approach.

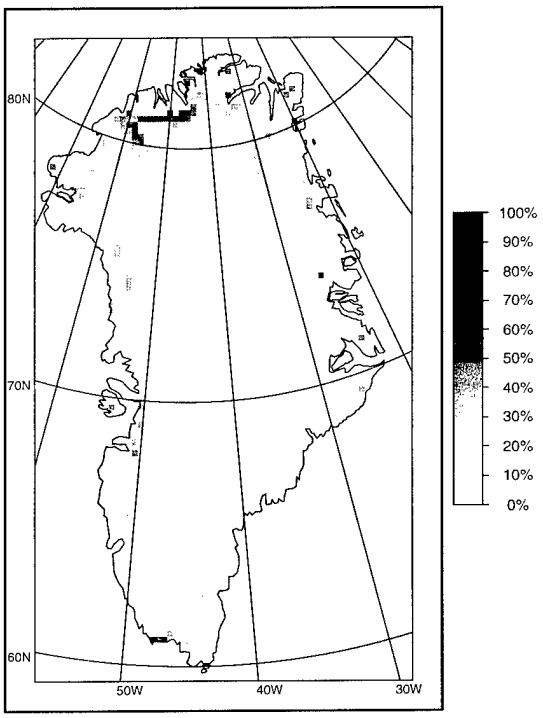

a. When the single-channel shows a higher melt frequency (a positive difference).

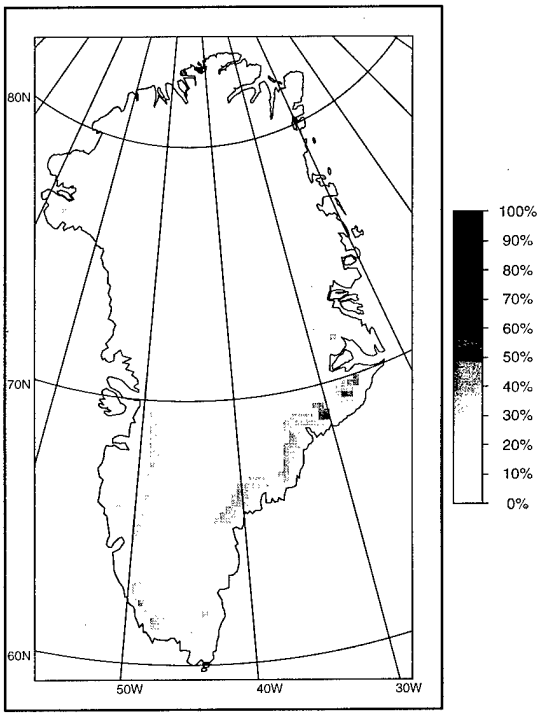

b. When the XPGR displays a higher melt frequency (a negative difference).

Figure 3. The difference in frequency of melt (in days) identified by the single-channel minus the XPGR approach.

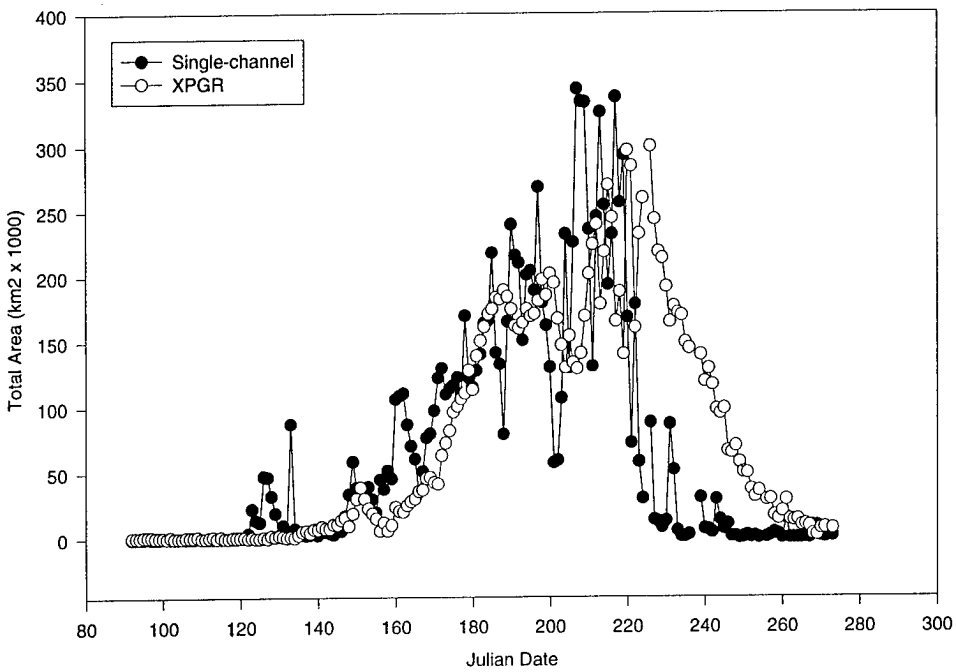

Figure 4. Time series of daily melt for the single-channel and XPGR approaches.

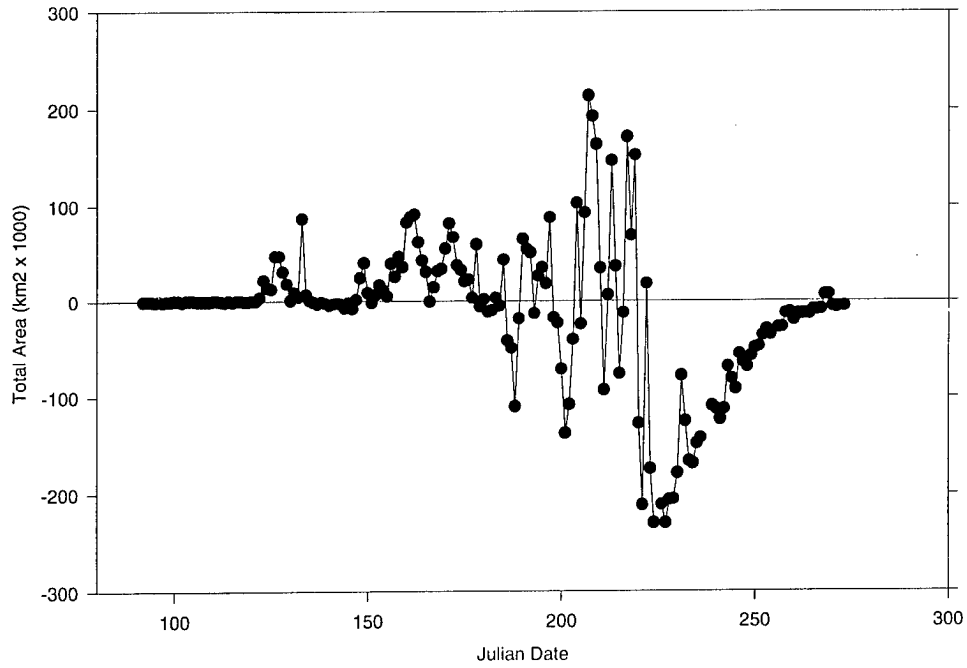

Figure 5. Differences in the time series of daily melt for the single-channel minus XPGR approaches.

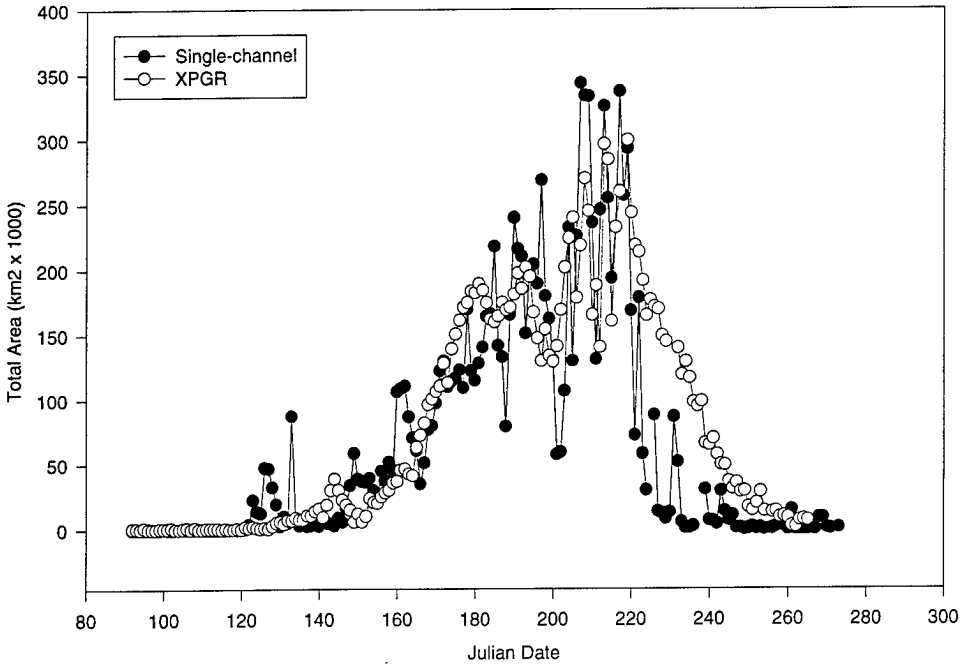

Figure 6. Time series of daily melt for the single-channel and XPGR lagged 7 days.

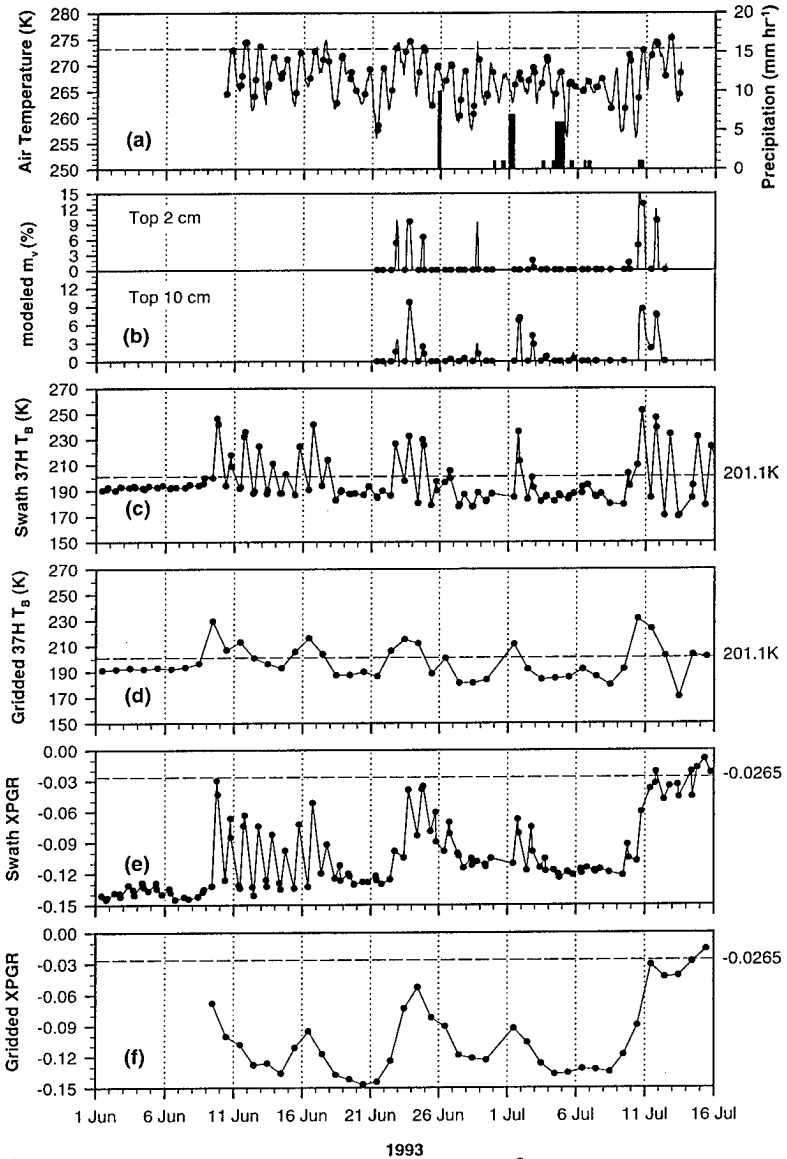

Figure 7. Time series for Dye 2, Greenland, representing surface observations, energy-balance model results, and swath brightness temperature data.

lag may even be greater than 7 days late in the melt season. This change in the lag during the melt season possibly is caused by the lack of penetration of liquid water into the snowpack early in the season. Later in the melt season, the XPGR approach may be indicating meltwater a few centimeters into the snowack as a residual from a previous day's melting. The single-channel approach's thresholds need to be adjusted lower late in the melt season to account for lower non-melt brightness temperatures that result from larger snow grain sizes after metamorphism. If this is the case, the single-channel approach is underestimating melt late in the season. The XPGR approach may also be overestimating melt late in the summer by identifying highly metamorphosed snow as melt.

Similar results were found when a more detailed study of the swath brightness temperatures for Dye 2 were analyzed for 1993 (Fig. 7). The swath data were also gridded for comparison. The single-channel approach indicates melt during periods with temperatures above 0°C and when the modeled liquid water content is above 1%. The XPGR approach only reaches its melt threshold after prolonged melt has occurred, near the end of the period. The single-channel approach identifies more melt events and identifies them earlier in the melt season. Both approaches show reduced response to melt owing to the temporal averaging of the swath data.

CONCLUSIONS

Monitoring surface snowmelt and melt frequency from passive microwave data needs to be continued to establish a longer period of record for use in climate change studies and to aid in understanding the energy balance responses of the Greenland ice sheet. The research presented demonstrates that the two approaches detect similar extents and durations of melt occurrences. The results also indicate that both approaches do have differences in detection of snowmelt, most likely attributable to how melt occurs in the snowpack and its representation by passive microwave radiation. The potential exists for combining the techniques to get some indication of the vertical extent of melt. Even though passive microwave sensors and their calibrations have changed in the past and will continue to change in the future, the approaches used to determine melt are important, allowing long time series of daily melt extent to be established. From these time series, annual variations in the extent of melt can be determined, advancing our knowledge of how the Greenland ice sheet might respond to future climate changes.

ACKNOWLEDGMENTS

This work was supported at the University of Nebraska by NASA grant NAGW-1266 and training grant NAGW-3685, and at the University of Colorado by NASA grant NAGW-2158 and from the Swiss National Foundation for Scientific Research grants 21-27449.89 and 20-36396.92. The SSM/I gridded brightness temperatures obtained on CD-ROM were from the National Snow and Ice Data Center, Boulder, Colorado.

LITERATURE CITED

Abdalati, W. and K. Steffen (1995) Passive microwave-derived snow melt regions on the Greenland ice sheet. *Geophy. Res. Let.*, **22**(7): 787–790.

Mote, T.L. and M.R. Anderson (1995) Variations in snowpack melt on the Greenland ice sheet based on passive microwave measurements. *Journal of Glaciology*, **41**(137): 51–60.

Hysteresis in the Relationship Between Glacier Sliding Velocities and Basal Water Pressure

D.B. BAHR
CIRES, University of Colorado, Boulder, CO 80309

J.B. RUNDLE
Department of Geological Sciences and CIRES,
University of Colorado, Boulder, CO 80309

ABSTRACT

Previous analyses have elucidated many of the different processes that control movement at the bed of glaciers and ice sheets. These processes have been studied as agents that act independently of other physics that might control sliding on nearby regions of the glacier bed. However, observations suggest that basal processes are heterogeneously (effectively randomly) distributed, and, therefore, a large-scale picture of sliding requires a statistical treatment of the many simultaneously interacting basal processes. We have developed two models of sliding, an elastic slider-block and a visco-elastic lattice Boltzmann model, both of which use random distributions of effective basal friction to simulate the randomly distributed sliding processes. Results from both models suggest that the interactions among multiple basal processes cause hysteresis in the relationship between basal water pressure and sliding velocities. In other words, the sliding velocity is a function of both the current water pressure and the water pressure history. Statistical, mechanical analyses of the elastic slider-block simulation data also show that, under steady-state conditions, fluctuations in the sliding velocities occur at the bed but will be too small to be observed by standard surface surveying techniques.

The Physical Basis for Glacier Volume–Area Scaling and Implications for Mass Balance Profiles

D.B. BAHR
CIRES, University of Colorado, Boulder, CO 80309

M.F. MEIER
INSTAAR and Department of Geological Sciences,
University of Colorado, Boulder, CO 80309

S.D. PECKHAM
CIRES, University of Colorado, Boulder, CO 80309

ABSTRACT

Detailed mass balance rate profiles are known on only a few of the hundreds of thousands of glaciers world-wide, but they are an important component of many climate, sea level, and ice dynamics studies. The few known profiles indicate that balance rates are probably nonlinear along a glacier's length, perhaps with a characteristic parabolic shape. Observations of Accumulation Area Ratios (AARs) between 0.55 and 0.7 suggest that many glaciers may have similar mass balance distributions, but theoretical arguments for similar distributions have been lacking. We show from first principles (conservation of mass and momentum, and Glen's constitutive law) that balance rate profiles, accumulation area ratios, and volume–surface area scaling are intimately related. Given one, the other two are fixed. In our case, we have data from a number of the world's temperate glaciers showing that ice volume, V, scales with surface area, S, with an exponent of roughly 1.36 (i.e., $V = cS^{1.36}$). From the theoretical developments, this exponent predicts a characteristic mass balance rate profile that is parabolic and also predicts an AAR of 0.58, well within the range of AARs observed for small glaciers believed to be in a "healthy" steady-state. Although most of the existing data are for small and accessible temperate glaciers, our theoretical arguments are more generally valid and apply to large ice sheets as well. Ice from the Antarctic Ice Sheet is lost primarily by calving at the margin, implying an AAR of approximately one. Using AAR = 1, the theory predicts a characteristic balance rate profile that is roughly constant, except for a discontinuity at the margin. This, in turn, shows that volume scales as surface area, with an exponent of 1.25, virtually identical to observations of 1.23. Regional estimates of AARs are relatively easy to measure using aerial photography and remote sensing, so the theory gives a useful technique for estimating characteristic balance rate profiles and volume of ice in a given region of the world with a minimum of field expense.

Analysis of Mass Balance Indicators in the New Glacier Inventory of the Former Soviet Union

D.P. BEDFORD, R.G. BARRY, C. HAGGERTY
World Data Center-A for Glaciology, University of Colorado, Boulder, CO 80309-0449,
email dbedford@nsidc2.colorado.edu

INTRODUCTION

Understanding the climate–glacier relationship has acquired a new urgency as a result of increasing concern that human activities may produce global climate change. Use of glaciers as climate indicators can provide information valuable for the detection of such change from regions that lack more conventional climate data. Analysis of mass balance, either directly or through proxy indicators, is the principal technique for gaining climate information from glaciers.

However, using glaciers as climate indicators at scales greater than the single glacier–local climate requires data from many glaciers over a wide area. Detailed mass balance measurements are typically unavailable at such scales, and simple glacier inventories are now gaining recognition as valuable databases for more wide-ranging climate–glacier studies (Haeberli and Hoelzle 1995). Unfortunately, such inventories were largely unavailable for sizable parts of the Earth's land surface until recently because of political differences. The National Snow and Ice Data Center (NSIDC)/ World Data Center-A (WDC-A) for Glaciology has recently acquired a digitized glacier inventory for the territory of the former Soviet Union, developed at the Institute of Geography, RAS, Moscow, under the leadership of Professor V.M. Kotlyakov, comprising records for 21,651 glaciers and providing a major increase in the global cryospheric database. The work presented here uses the new inventory to examine spatial and temporal variations in indicators of mass balance in the territory of the former Soviet Union.

MASS BALANCE INDICATORS

Glacier inventories rarely provide data from detailed mass balance studies. Consequently, proxy indicators must be used, drawn from the available data. On the basis of data availability, two approaches to the study of mass balance are adopted. One approach examines spatial variations in Accumulation Area Ratio (AAR), while the other examines spatial and temporal variations in Equilibrium Line Altitude (ELA). AAR is calculated as the ratio of accumulation area to total area; thus, the theoretical basis for the use of AAR as a mass balance indicator is that AAR identifies the proportion of the glacier over which net accumulation is taking place. Glaciers in steady state have AARs between about 0.5 and 0.8 (Nesje 1992), although a steady-state AAR of about 0.65 to 0.7 is also commonly cited (Paterson 1994). Lower AARs indicate negative mass balance, higher AARs indicate positive mass balance. On this basis, changes in AAR over space and time can be used to identify changes in net mass balance.

Use of ELA as a mass balance indicator hinges on the fact that the ELA marks the point on the glacier at which net mass balance equals zero. Changes in ELA, therefore, indicate mass balance changes—a reduced ELA indicates a greater proportion of the glacier area above the ELA, and, therefore, an increase in mass balance. The reverse is true for increased ELA.

Sufficient data were available in the glacier inventory for both of these parameters (AAR and ELA) to be calculated for many glaciers in the former Soviet Union. 8393 glaciers were used in the AAR analysis, and 1302 glaciers were used in the ELA analysis, representing 39% and 6% of the total inventory respectively.

AAR ANALYSIS

The 8393 glaciers in the inventory with data for both total area and ablation area were used in the AAR analysis. These glaciers covered six regions of the Eurasian land mass: Franz Joseph Land, Novaya Zemlaya, the Kamchatka Peninsula, central Asia, and the northern and southern Caucasus. Several steps were involved in the AAR analysis:

1. The AAR was calculated for each glacier, using AAR = (total area – ablation area)/total area,

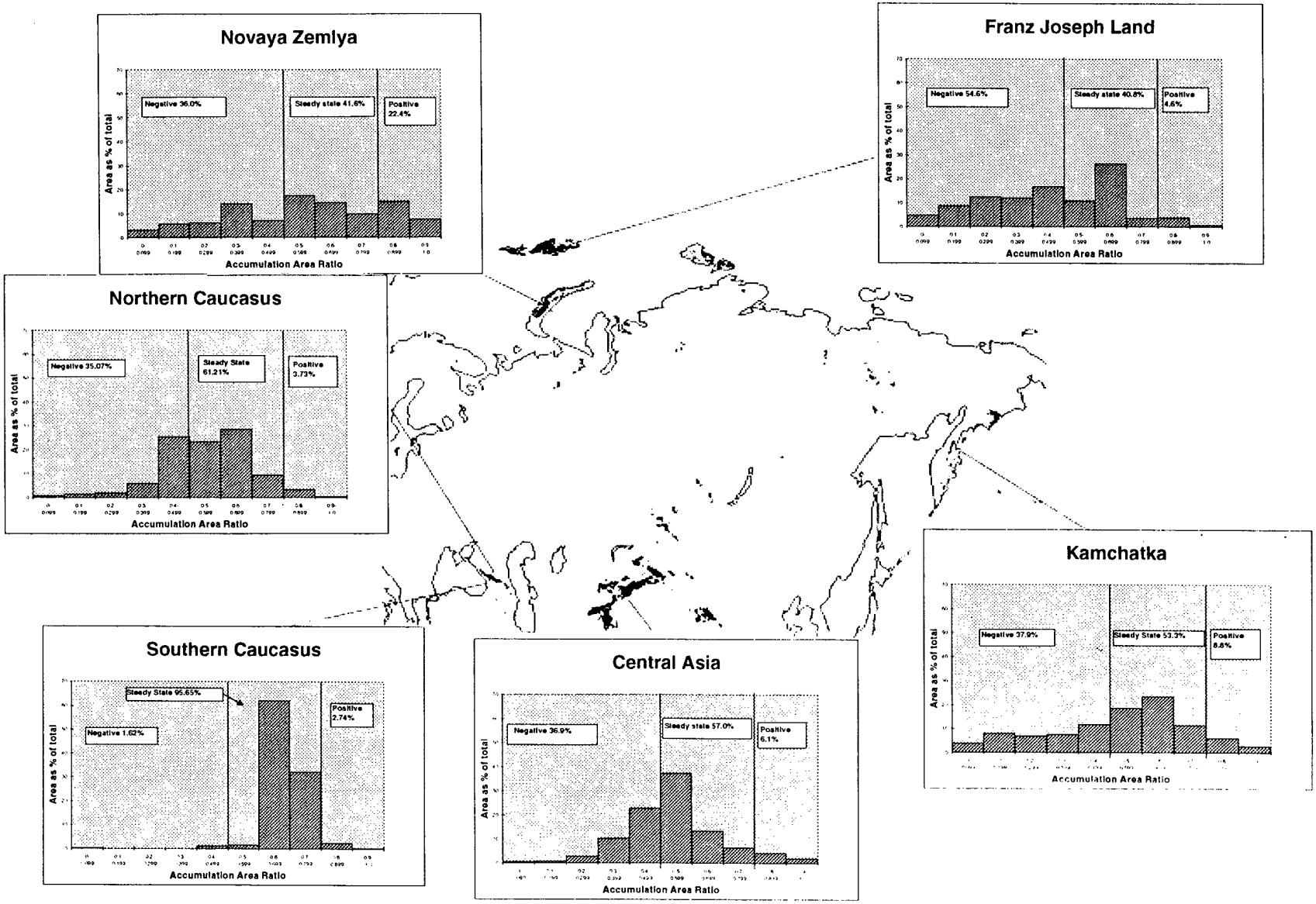

Figure 1. Frequency distributions for accumulation area ratios by region, displayed as percentage of regional glacier area per accumulation area ratio category. Locations of regions are shown on the map.

Table 1. Total and mean areas of glaciers used in AAR analysis, by region.

Region	Total glacier area (km^2)	Mean glacier area (km^2)
Franz Joseph Land	10,824.60	18.20
Novaya Zemlaya	5,236.90	24.36
Kamchatka Peninsula	565.80	3.14
Northern Caucasus	1,374.40	1.45
Southern Caucasus	520.55	3.97
Central Asia	8,422.01	1.33

on the rationale that accumulation area = total area – ablation area.

2. The glaciers were grouped by region, based on their identification numbers, so that spatial variations in AAR could be examined.

3. The glaciers in each region were grouped into categories of AAR, ranging from 0.0 to 1.0, at intervals of 0.1. Thus, categories are 0.00 to 0.09, 0.10 to 0.19, 0.20 to 0.29, and so on. This allowed AAR frequency distributions to be compared among regions.

4. For each region, the total glacier area in each AAR category was determined.

5. For each region, the glacier area in each AAR category was recalculated as a percentage of the total glacier area in the region; standardized for glacier area, this further facilitated inter-regional comparison.

The results of this analysis are displayed in Figure 1, indicating the distributions of glacier area by AAR category for the six regions studied. A clear difference in the shape of these distributions between higher latitude and lower latitude regions can be seen in Figure 1. Higher latitude regions seem to have a "broad and flat" (platykurtic) distribution, in which there is little variation in the percentage of glacier area between AAR categories. This can be seen clearly for Franz Joseph Land and Novaya Zemlaya, and to a lesser extent for the Kamchatka Peninsula. Lower latitude regions, on the other hand, tend to have "narrow and sharp" (leptokurtic) distributions, in which glacier area is concentrated in three or four key AAR categories, typically between about 0.4 and 0.7. This can be seen clearly for the northern and southern Caucasus, and Central Asia.

Climatic differences may well be the cause of this difference, although another possible explanation can be found in the distribution of glacier areas in the samples taken from the various regions. As shown in Table 1, the lower latitude glaciers used in this study tend to be smaller, on average, than the higher latitude ones, reflecting in part the different geographical characteristics and in part the biases in field studies and the available samples. Glaciers of different size tend to have different mass balance profiles. Thus, the size composition of the glacier samples could affect the AAR distributions.

One consequence of the difference in AAR distribution is that lower-latitude glaciers should be more responsive to long-term changes in mass balance, in that relatively small mass balance shifts would move greater fractions of the regions' glacier areas out of steady state and into positive or negative mass balance.

ELA ANALYSIS

The ELA analysis was conducted on the basis that the ELA can be identified by the Snow Line Elevation (SLE) at the end of summer (Paterson 1994). A data subset was chosen using glaciers with SLE measurements taken in the last week of August or the first week of September. Suitable data were found only for Central Asia (1045 glaciers, 7% of the regional total) and the Caucasus mountains (257 glaciers, 17% of the regional total), spanning the period from 1946 and 1955, respectively, up to 1967, although observations were not made every year. Thus, the period of record is discontinuous, fairly short, and the number of observations in any single year is often quite small. With these shortcomings in mind, the ELA analysis proceeded using several steps:

1. Glaciers were grouped by region (Central Asia or Caucasus) and by year of observation.

2. SLEs were standardized for glacier elevation by subtracting from mean elevation. Haeberli and Hoelzle (1995) use mean elevation as a crude proxy for ELA; thus, the method used here compares the SLE-derived proxy ELA with a baseline ELA derived from mean elevation.

3. Means of mean elevation minus SLE were calculated for each region and each year with available data.

Results are shown in Figure 2. 1958 appears as an anomalously high snow year in Central Asia, and this is partially supported by precipitation data from the Global Historical Climate Network (see Vose et al. 1992) for foothills stations at Djizak and Chimkent, which show a very wet spring.

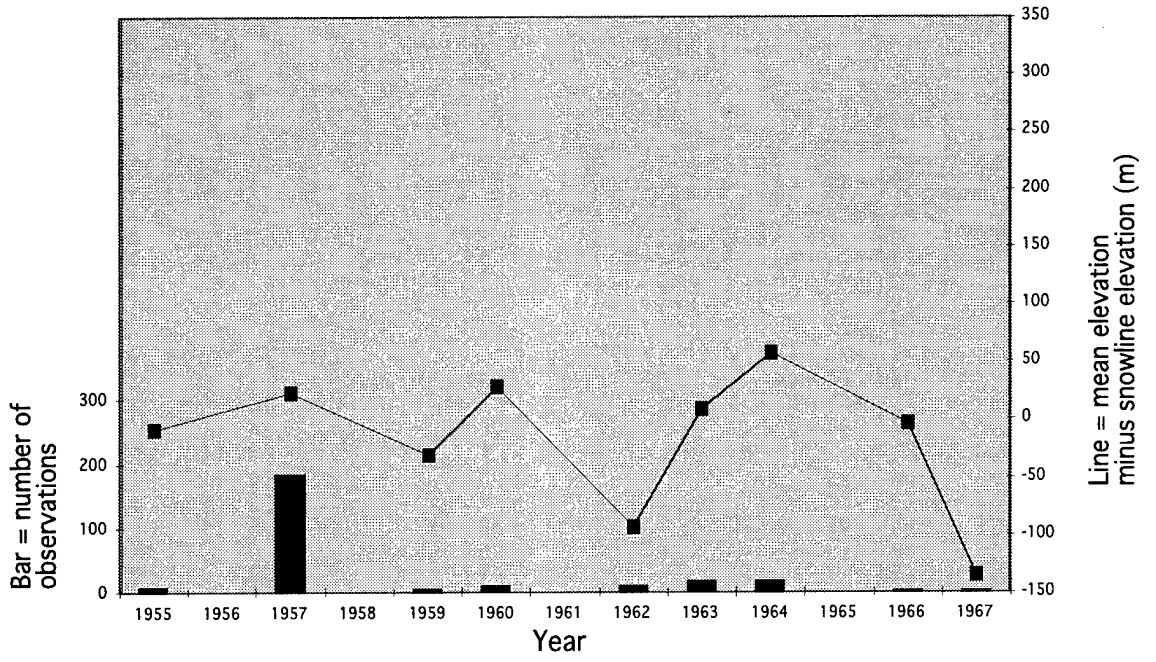

a. Caucasus Mountains.

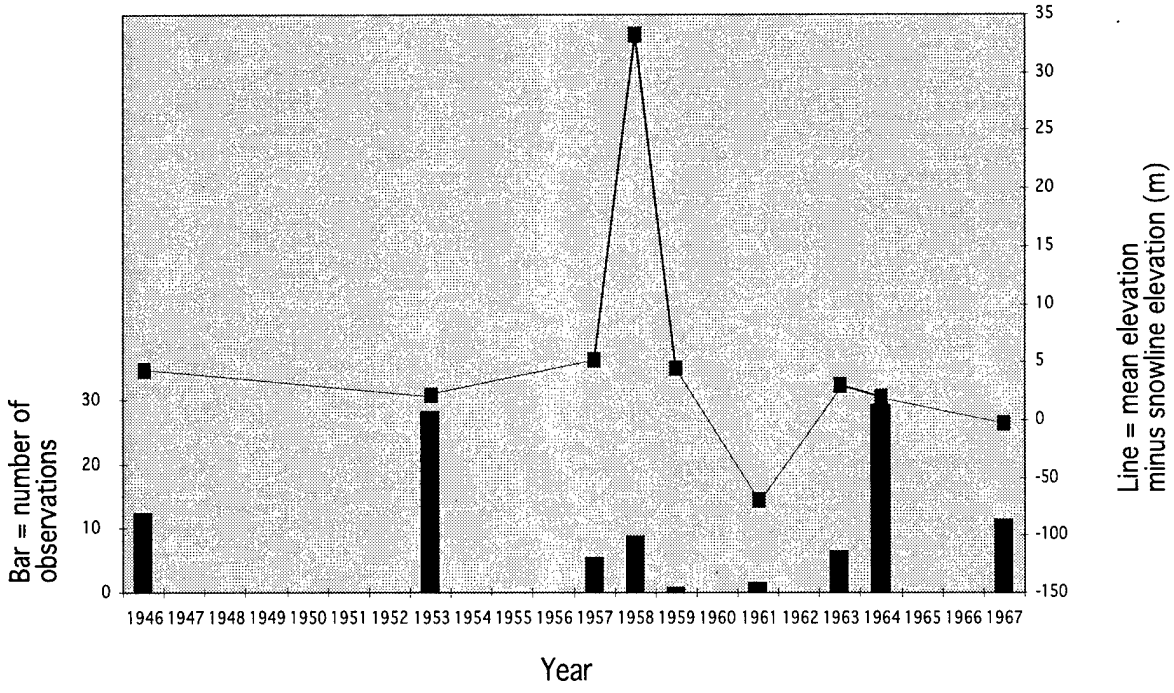

b. Central Asia.

Figure 2. Mean elevation minus snowline elevation over time for glaciers in the Caucasus Mountains and Central Asia, along with number of observations in each year. Note the time scales are different for the two graphs.

However, the overall trend is for a decrease in mean elevation minus SLE. Thus, SLE is increasing relative to mean elevation over time, indicating reduced mass balance. For the Caucasus, this result is supported by earlier work that identified a glacier retreat trend beginning around 1976–77 (Bedford and Barry 1995). Under the assumption of a typically decadal-scale mountain glacier response time, the reduced mass balance identified here for 1966–67 could produce a glacier retreat response by 1976–77.

CONCLUSIONS

Attempts to extract mass balance indicators from the new Eurasian glacier inventory resulted in fairly small data subsets, with consequent problems of representativeness. However, both the AAR and ELA analyses produced interesting results, and the techniques used appear to show some promise. Overall, it would seem that lower-latitude glaciers are likely to act as more sensitive indicators of long-term mass balance change (hence also climate change) than are higher-latitude glaciers. ELA analysis for some of these lower-latitude glaciers suggests a general trend towards reduced mass balance up to 1967, a conclusion supported by the subsequent trend towards glacier retreat identified for the Caucasus mountains (Bedford and Barry 1995). Further confirmation of this trend must be sought in analysis of climate data. In addition, several techniques for glacier inventory analysis have recently emerged. These include simulation of glacier response to climate forcing (Haeberli and Hoelzle 1995) and relating glacier area to volume (Meier and Bahr 1995). Future work may involve application of those techniques to the Eurasian glacier inventory.

ACKNOWLEDGMENTS

The inventory of former Soviet Union glaciers was kindly provided by Professor V.M. Kotlyakov, Institute of Geography, RAS, Moscow, via WDC-B for Glaciology. The project is supported by NOAA/ESDIM through the CIRES/NOAA Cooperative Agreement, NOAA number NA37RJ0201.

LITERATURE CITED

Bedford, D.P. and R.G. Barry (1995) Glacier trends in the Caucasus, 1960s to 1980s. *Physical Geography*, **15**(5): 414–424.

Haeberli, W. and M. Hoelzle (1995) Application of inventory data for estimating characteristics of and regional climate change effects on mountain glaciers: a pilot study with the European Alps. *Annals of Glaciology*, **21:** 206–212.

Meier, M.F. and D.B. Bahr (1995) Counting glaciers: use of scaling methods to estimate the number, size, and thickness distribution of the glaciers of the world. *AGU 1995 Fall Meeting: Abstract Supplement to Eos*, Abstract H11D-1, p. F183.

Nesje, A. (1992) Topographical effects on the equilibrium-line altitude on glaciers. *GeoJournal*, **27**(4): 383–391.

Paterson, W.S.B. (1994) *The Physics of Glaciers*, 3rd edition. London, New York and Tokyo: Pergamon/Elsevier Science Ltd.

Vose, R.S., R.L. Schmoyer, P.M. Steurer, T.C. Peterson, R. Heim, T.R. Karl and J.K. Eischeid (1992) *The Global Historical Climatology Network: Long-term monthly temperature, precipitation, sea level pressure, and station pressure data.* ORNL/CDIAC-53, NDP-041. Carbon Dioxide Analysis Center, 100 p.

Borehole Video from Multiple Sites across the Haut Glacier d'Arolla, Switzerland

LUKE COPLAND, JON HARBOR
Department of Earth and Atmospheric Sciences,
Purdue University, West Lafayette, IN 47907, USA
luke@geo.purdue.edu; jharbor@geo.purdue.edu

SHULAMIT GORDON, MARTIN SHARP
Department of Earth and Atmospheric Sciences,
University of Alberta, Edmonton, AB T6G 2E3, Canada
gordons@geog.ualberta.ca; msharp@geog.ualberta.ca

ABSTRACT

Twenty-five boreholes were drilled to the base of the Haut Glacier d'Arolla, Switzerland, in summer 1995. The boreholes were distributed across a half-section of the glacier, with closest spacing towards the glacier margin. The boreholes ranged in depth from less than 30 m near the edge of the glacier, to almost 140 m near the center of the glacier. A miniature color video camera was lowered down 11 boreholes, and this provided direct, real-time observation of the interior and basal conditions of this temperate valley glacier.

The video logs showed distinct changes in ice conditions with depth in the glacier. This included vertical and horizontal ice foliations, and changes in ice bubble content and color (Copland et al., in press). The glacier bed was observed in three boreholes, and consisted of clasts in a matrix of unconsolidated fine sediment (Fig. 1). A basal ice zone characterized by sediment-laden, bubble-poor ice was observed in the boreholes in which the bed was seen. The basal ice zone was vertically more

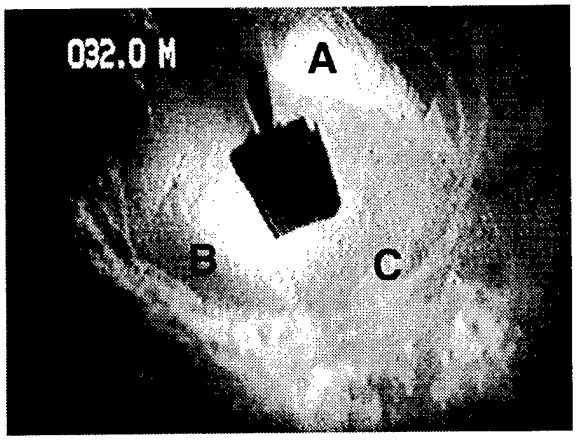

Figure 1. Video image of the glacier bed observed in borehole 95/10 at a depth of 32.0 m. The borehole is approximately 12 cm in diameter. Marker A is a clast projecting out into the borehole a few centimeters above the bed; B is a clast resting on the base of the borehole; and C is a clast resting on the base of the borehole and partially frozen into the surrounding ice.

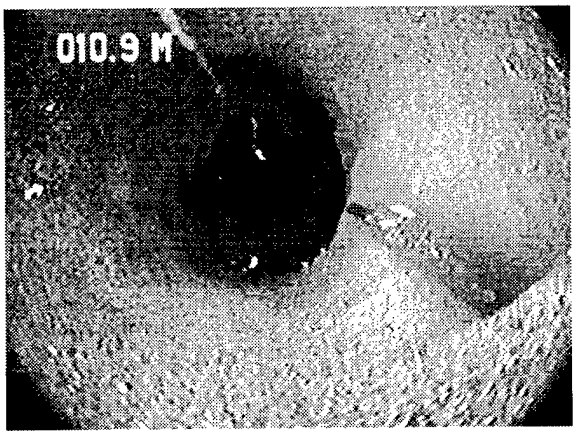

Figure 2. Video image of the englacial channel observed entering borehole 95/15 at a depth of 10.9 m. The channel opening is 'keyhole' shaped, and approximately 15 cm high and 4 cm wide. The borehole is approximately 10 cm in diameter.

extensive towards the center of the glacier, reaching a thickness of approximately 20 m in the deepest borehole. The video also helped confirm that borehole profiles determined by borehole inclinometry were correct.

Borehole video also proved useful in determining the englacial and subglacial hydrology of the Haut Glacier d'Arolla (Copland et al., in review). The water level in the boreholes was clearly identifiable, and distinct changes in water turbidity were correlated with electrical conductivity measurements to provide information on the likely origin of borehole water inputs. In addition, a total of five different englacial channels were observed in the borehole walls. Clear water was observed entering a borehole from two englacial channels above the water level, and turbid water appeared to enter a borehole from an englacial channel below the water level. The most clearly defined englacial channel had a distinct 'keyhole' shape, and was approximately 15 cm high and 4 cm wide (Fig. 2). It occurred above the borehole water level, and there was no detectable water flow through it. It appears that the keyhole shape results from an initially high water level followed by low water flow (Shreve 1972). This is because high water levels are likely to produce an initially circular channel that is deepened by preferential melting of the channel base during periods of low water flow.

Overall, video recordings provide useful qualitative and semi-quantitative data that enhance our ability to provide logical explanations of a range of physical and chemical parameters measured in boreholes. A 23-minute composite videotape of the "highlights" of the Haut Glacier d'Arolla video recordings has also been produced for educational and research use. A copy of this video can be obtained by contacting Copland.

LITERATURE CITED

Copland, L., J. Harbor and M. Sharp (in press) Borehole video observation of englacial and basal ice conditions in a temperate valley glacier. *Annals of Glaciology,* **24**.

Copland, L., J. Harbor, S. Gordon and M. Sharp (in review) The use of borehole video in investigating the hydrology of a temperate glacier. *Hydrological Processes.*

Shreve, R.L. (1972) Movement of water in glaciers. *Journal of Glaciology,* **11:** 205–214.

Mapping Ice Sheet Topography with Laser Altimetry in Greenland

BEÁTA M. CSATHÓ
Byrd Polar Research Center, The Ohio State University, Columbus, OH 43210

ROBERT H. THOMAS
Code YS, NASA HQ, Washington, DC 20546

WILLIAM B. KRABILL
Laboratory of Hydrospheric Processes,
NASA/Goddard Space Flight Center, Wallops Island, VA 23337

INTRODUCTION

The vast ice sheets of Antarctica and Greenland cover almost 10% of the Earth's land surface. Together with sea ice they have a significant influence on local and global climate. Moreover, the mass balance of polar ice masses is a sensitive indicator of global climate changes. There is a growing concern that some ice fluctuation may occur at a rapid rate with an associated effect on the global sea level. Thus, it is imperative to monitor the ice sheets on a global scale, assess their mass balance, and predict their future behavior.

Laser altimetry provides a solution for precise mapping and monitoring of polar regions. The Airborne Topographic Mapper (ATM)—a scanning laser altimeter—has been developed and tested by NASA for measuring ice sheet elevations to an accuracy needed to detect meaningful changes. Results from flight data demonstrate that the ice sheet elevation can be reliably measured to an accuracy of 20 cm (possibly 10 cm) over baselines of more than 700 km (Krabill et al. 1995).

The laser scanner covers a 130- to 200-m-wide swath with a set of overlapping spirals, providing a dense data set along the flight lines suitable for mapping ice sheet topography to unprecedented accuracy and detail. This continuous and accurate topographic mapping capability has major potential for mass balance studies. Although this high accuracy is achieved only along the aircraft flight lines, the resulting elevation profiles can also be used for investigating specific processes, such as the relationship between surface and bed topography. Moreover, they provide quality checks and validation of other, more spatially intensive, elevation data sets, such as those derived from aerial photogrammetry, SAR interferometry, and satellite radar and laser altimeters.

The purpose of this paper is to describe the studies that have been carried out to derive Digital Elevation Models (DEMs) and topographic maps from ATM data. The huge and irregularly distributed data sets are not easily manageable. Triangulated Irregular Network (TIN) model-based interpolation schemes were selected for data interpolation because they work well for irregularly distributed data. A simple but efficient thinning technique, developed for reducing the redundancy of the large data sets, proved also suitable for removing the blunders. Fourier transform, scale-space analysis, and other methods were used for analyzing the resulting elevation models and for extracting ice sheet features. For satellite altimetry simulation, parallel strips were bridged together providing 4-km-wide and 50- to 100-km-long DEMs.

In the second part of the paper, examples illustrate the variety of applications of airborne laser altimetry. Wind generated surface roughness is mapped in detail. Undulations related to bottom topography are derived from the DEMs created by merging the parallel strips. Surface lakes located near the equilibrium line are delineated and their temporal changes are studied by using repeat laser altimetry and aerial photographs. Ice velocity is estimated from the geometry of the ripples accompanying the lakes.

MEASUREMENTS

With the advent of GPS and laser technology in recent years, laser altimetry becomes an increas-

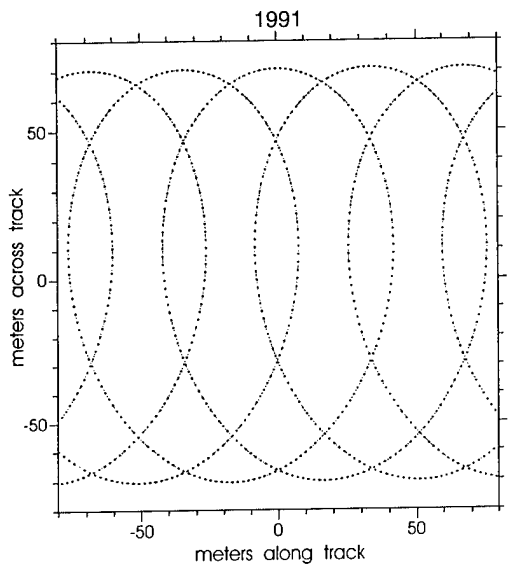

a. 1991 system specification.

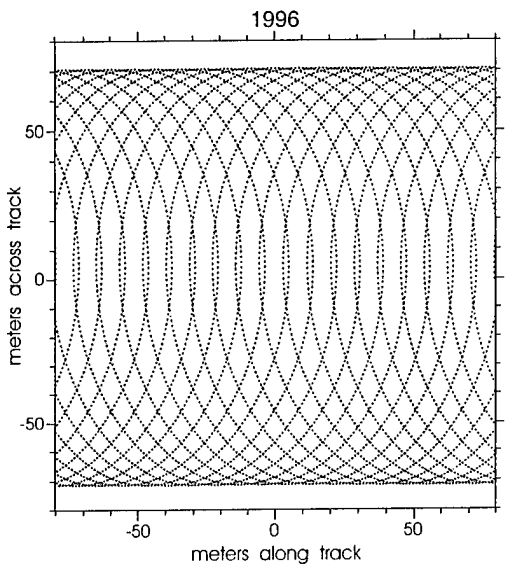

b. Present (1996) system specifications.

Figure 1. Scan pattern produced by ATM system.

ingly important mapping tool. NASA has developed several different airborne laser systems, including the Airborne Oceanographic Lidar (Krabill and Swift 1985) and the Airborne Topographic Mapper. The latter system was developed for the sole purpose of topographic mapping, particularly for NASA's Greenland mapping program.

The transmitter for the ATM system is a pulsed laser that operates in the visible part of the spectrum. The laser beam is directed along an oval shaped pattern with the help of a nutating mirror, producing a set of overlapping spirals (Fig. 1). In 1991 the aircraft flew 400 m above the ground, yielding a laser spot on the surface of approximately 0.6 m in diameter. With a laser pulse rate of 800 s^{-1} and with 5 conical scans s^{-1}, the maximum along-track separation between the laser footprints was 20 m, and the cross-track separation was less than 4 m (system specifications in 1991, Fig. 1a). Ranges are calculated from the round-trip travel time of the laser pulse between the aircraft and the surface, measured by a threshold detector, and are subsequently corrected for thresholding effects ("range walk"), using return signal peak amplitude data.

To provide higher data density, the laser pulse rate and the scanner rotation rate have gradually been increased. The present system uses a laser pulse rate of 5000 s^{-1} with 20 conical scans s^{-1}, giving a very dense data array (Fig. 1b).

The ATM system is mounted on a P-3 aircraft. The aircraft location is determined using differential GPS techniques, requiring simultaneous acquisition of GPS data aboard the aircraft and at a fixed location. The attitude information is obtained from an Inertial Navigation System.

Principal sources of errors are in laser ranging, and in aircraft position and attitude. Numerous tests by NASA, including comparison of data where flight lines cross and from repeat flights, indicate an accuracy of 10–20 cm (RMS) (Krabill et al. 1995).

DATA PROCESSING

During data processing, the data measured by the individual sensors are integrated, and various corrections of systematic errors, as determined by ground and in flight calibration procedures, are made. The following parameters are available after the data processing: geographic latitude, lon-

gitude, and elevation of the laser footprint (referred to WGS-84 ellipsoid), scan azimuth, pitch and roll of the aircraft, and GPS time of the measurements.

The ATM data sets are very large* and not easily manageable. Spatial distribution is quite irregular, with redundant data near edges and small gaps in the middle of the swath. Outliers are caused by the reflection of the laser beam from clouds, ice fog or blowing snow, or measurement errors.

We briefly describe here efforts to derive DEMs from the raw ATM data. For details the reader should refer to Csathó et al. (1996). The recommended processing steps are as follows:

1. Transformation of the ellipsoidal coordinates into a suitable projection system.
2. Blunder removal and optional data thinning.
3. Creation of TIN (Triangulated Irregular Network) model.
4. Interactive editing and smoothing of the TIN model (optional).
5. Interpolation of the TIN model.

In our study the geographical coordinates were transformed into the Universal Transverse Mercator (UTM) projection system. Blunders were removed by interactive editing or by using the procedure described in the next paragraph. The TIN models were created by Delauney triangulation and optionally smoothed by least squares. A neighborhood-based planar interpolation was used to create the DEMs and contour maps. The contour lines of the final maps were smoothed by a weighted average method, and drawn by B-splines. The data were processed on an Intergraph workstation using the MGE (Modular GIS Environment) Modeler software package from Intergraph Inc.

The original data can be used to generate large scale contour maps of small areas. For creating DEMs covering large areas, the ATM data sets first should be pre-processed, including blunder detection and thinning. Ice sheet surfaces are typically very smooth and they can be approximated by small planar patches. A patch size of 25 m was selected on the basis of the a priori analysis of the surfaces and the scanning geometry (Fig. 1). Because the largest distance between the consecutive ellipses of the scan pattern is approximately 20 m, every grid cell should contain at least one scan line. After transforming the original ATM data into a suitable projection system, all points within a 25-m grid cell are used to determine a best-fitting plane by least squares. Blunders are removed and the elevation of the tilted plane at the cell's center is used as a representative point. Using the centroid of the grid cell as a representative point (first order approximation) also works well. The standard deviation, σ, obtained in this procedure comprises two errors: observation error of the ATM data points and approximation error. It follows that larger σ values are to be expected on heavily crevassed areas, on rocks, on the calving front of glaciers, or over fjords with floating icebergs. Data collected during bad weather (ice fog, blowing snow, etc.) also are characterized by higher σ values.

DEMs are particularly suitable for further analysis of the surface. By the application of well-known techniques such as Fourier transform, filtering, and scale-space theory, interesting features can be identified and delineated. Some experiments towards the automatic detection of lakes (or other features) from ATM data are presented in Csathó et al. (1995).

RESULTS

The ATM data used in this study were acquired in Greenland along the so called ERS-1 line in September 1991 (Fig. 2). Flights were also made on parallel tracks, offset from the main track by 1 and 2 km, thus mapping the surface topography within a 4-km band (Thomas et al. 1994).

Large scale mapping

Contour maps were created from the original, dense data over small areas to demonstrate the inherent potential of the ATM system for feature extraction. In Figure 3 the perspective view of a contour map shows a gently sloping surface. The elongated, low ridges located perpendicularly to the prevailing wind direction are most likely sastrugi.

Ice Stream North

The DEM derived from laser altimetry depicted in Figure 4a covers a 4- by 60-km area near the center of the ice sheet (Ice Stream N in Fig. 2). The area is close to the origin of a large flow feature (Fig. 2) that was identified using SAR (Synthetic Aperture Radar) imagery (Kwok and Fahnestock 1996). The large amplitude of the surface undula-

*For example, in 1991 a 1-hour flight rendered approximately 2,800,000 data points in a 400-km-long swath.

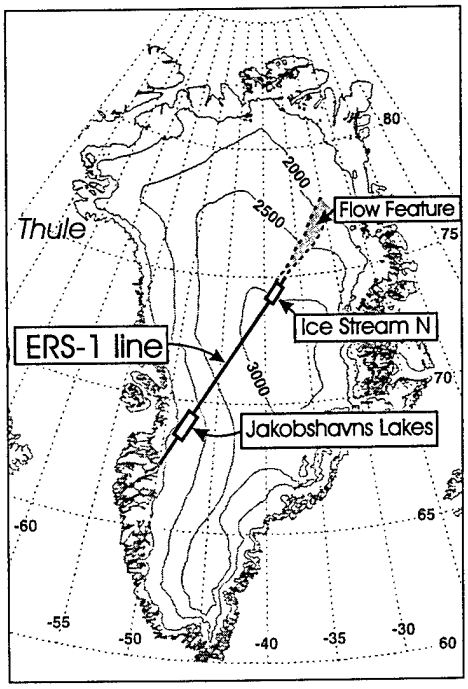

Figure 2. Location of the ERS-1 line in Greenland. Six parallel ATM flight lines were flown along the ERS-1 line and offset by 1 and 2 km in 19–21 September 1991. The parallel ATM swaths were bridged together to create DEMs on the Ice Stream North, and Jakobshavns Lakes areas. The elevation contours are from the DEM compiled by Simon Ekholm (National Survey and Cadastre, Denmark).

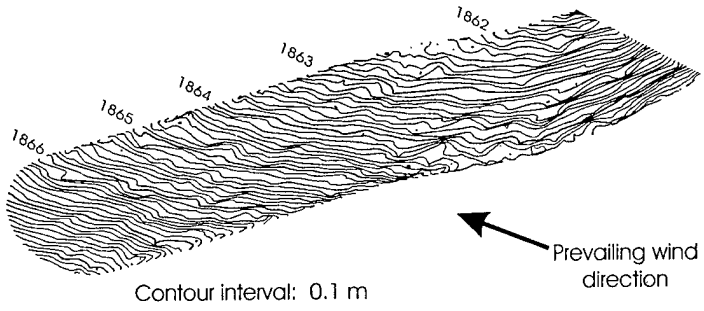

Figure 3. Perspective view of a large scale contour map (swath width is approximately 200 m). The elongated, low ridges are most likely sastrugi.

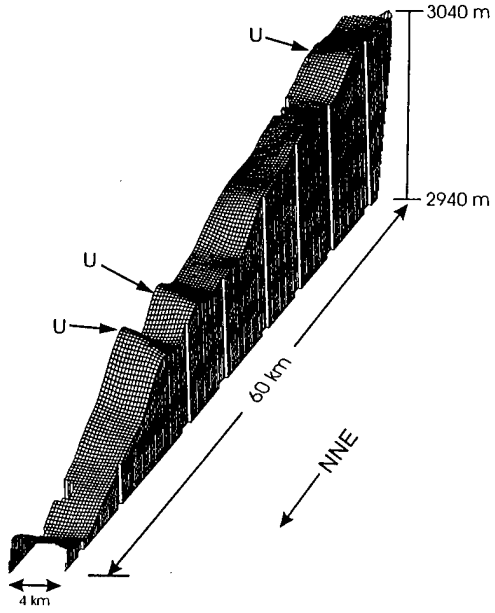

a. Perspective view of DEM (grid size: 100 m, vertically stretched).

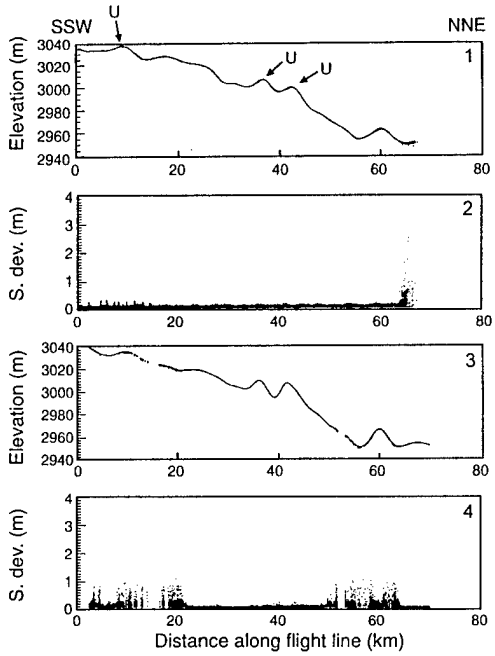

b. Surface elevation profile along the western (1), and the eastern boundary (3); standard deviation of surface elevations in 25- by 25-m grid cells before blunder removal along the western (2), and eastern boundary (4).

Figure 4. Ice Stream North DEM (for location see Fig. 2). The large surface undulations (U) are associated with basal topography.

tions, together with the low mean slope (≤ 0.1°), indicate a well-lubricated and fast flowing ice stream. The wavelength of the undulations is on the order of 6 to 12 km, about 2–4 times the ice thickness, suggesting that the undulations are associated with basal topography.

Five parallel ATM swaths were bridged together to create the DEM. The ATM data sets were thinned prior to the interpolation using the procedure described in the data processing section. The elevation profiles derived from the thinned laser altimetry data sets, together with the standard deviation determined before the blunder removal, are shown in Figure 4b. The large standard deviations (0.2–1.0 m) and the gaps on the elevation profiles are attributable to the effects of ice fog or blowing snow.

Jakobshavns Lakes

Another DEM was generated from the parallel swaths in the Jakobshavns drainage basin (Fig. 2, Jakobshavns Lakes). The velocity of the Jakobshavns glacier, which reaches 8 km/year at the floating terminus, is the highest recorded velocity of any non-surging glacier. Within the Jakobshavns drainage basin, at elevations lower than about 1400 m, there is considerable surface melting in summer, with fast-flowing melt streams cutting into the ice and large lakes of meltwater forming in depressions. The lakes are draining periodically through moulins at the bottom of the lakes or through rivers and streams on the ice sheet surface (Thomsen et al. 1989). The abundance of the surface features and the knowledge acquired during the years of extensive research make the Jakobshavns drainage basin an excellent test field. The laser altimetry derived DEMs and contour maps are analyzed in detail in Csathó et al. (1996).

Laser altimetry data and photogrammetrically derived DEM and orthophotos* were compared

*Aerial photographs were acquired on 7 July 1985 (Fastook et al. 1995).

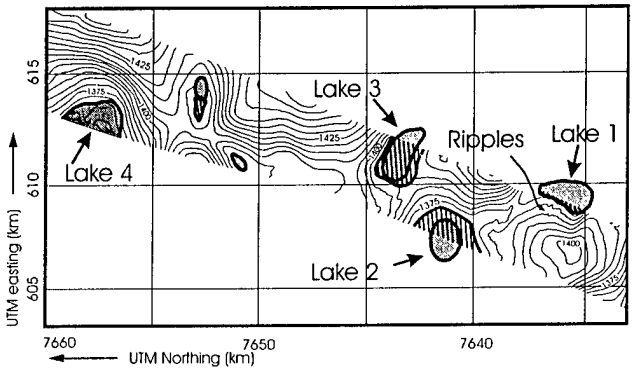

Figure 5. Contour map compiled from the Jakobshavns Lakes DEM (for location see Figure 2) around the elevation of 1400 m. Lakes were delineated using aerial photographs (shaded area, July 1985), and laser altimetry data (hatched area, September 1991).

to study the temporal changes of the lakes. The general agreement between the topography depicted by the two methods is good (Csathó et al. 1996). Because the ice on the lakes was melting during the photogrammetric flight mission, it was possible to delineate the lakes on the orthophotos. In addition, the smooth and horizontal lake surfaces can readily be identified from the laser altimetry data (Csathó et al. 1995). Figure 5 shows the laser-altimetry-derived contour map around the elevation of 1400 m, with the lake boundaries obtained from photogrammetry (1985) and laser altimetry (1991) superimposed on it. Although the ice sheet surface was moving with an estimated speed of 150–350 m/year to west-northwest (Echelmeyer et al. 1991), the position and the shape of the larger depressions did not change considerably between July 1985 and September 1991. It confirms that the larger surface depressions are tied to bedrock irregularities. Despite their proximity, the lakes do not drain at the same time. For example, Lake 4 had a high water level in July 1985 and drained completely in September 1991. Lake 2 and Lake 3 show an opposite trend, with a higher water level in September 1991. Lake 1 had the same water level both times. This behavior implies a complicated drainage mechanism. Detailed maps (not shown here) were derived to study the ripples following the shoreline downstream of Lake 1. Accepting the hypothesis that new ripples are formed in each year and that they are advecting with the moving ice (Echelmeyer et al. 1991), we can use them for determination of the ice velocity. In this case, the ice velocity and the flow direction inferred from the shape of the ripples are in good agreement with other estimates (e.g., Fastook et al. 1995).

LITERATURE CITED

Csathó, B., T.F. Schenk, R.H. Thomas and W.B. Krabill (1995) Topographic mapping by laser altimetry. *Proceedings of SPIE, Remote Sensing for Three-Dimensional Objects and Scenes* (T. F. Schenk, Ed.), Vol. 2572, p. 10–20.

Csatho, B., R.H. Thomas and W.B. Krabill (1996) Mapping ice sheet topography with laser altimetry in Greenland. BPRC Technical Report No-96-01. Columbus: Byrd Polar Research Center, The Ohio State University, 53 p.

Echelmeyer, K., T.S. Clarke and W.D. Harrison (1991) Surficial glaciology of Jakobshavns Isbræ, West Greenland: Part I. Surface morphology. *Journal of Glaciology,* **37**(127): 368–382.

Fastook, J. L., H.H. Brecher and T.J. Hughes (1995) Derived bedrock elevations, strain rates, and stresses from measured surface elevations and velocities: Jakobshavns Isbræ, Greenland. *Journal of Glaciology,* **41**(137): 161–173.

Krabill, W.B. and R.N. Swift (1985) Airborne lidar experiments at the Savannah River plant. NASA Technical Memo 4007, 91 p.

Krabill, W.B., R.H. Thomas, C.F. Martin, R.N. Swift and E.B. Frederick (1995) Accuracy of airborne laser altimetry over the Greenland ice sheet. *International Journal of Remote Sensing,* **16**(7): 1211–1222.

Kwok, R. and M.A. Fahnestock (1996) Ice sheet

motion and topography from radar interferometry. *IEEE Transactions on Geoscience and Remote Sensing*, **34**(1): 189–200.

Thomas, R.H., W. Krabill, S. Manizade, R. Swift and A. Brenner (1994) Comparison of radar-altimetry data over Greenland with surface topography derived from airborne laser altimetry. *Proceedings of Second ERS-1 Symposium—Space at the Service of Our Environment, Hamburg, Germany, 11–14 October 1993*, p. 165–169.

Thomsen, H.H., O.B. Olesen, R.J. Braithwaite and A. Weidick (1989) Greenland ice-margin programme, a pilot study at Pâkitsoq, northeast of Jakobshavns, central West Greenland. Gronlands Geologiske Undersogelse, Rapport 145, p. 50–53.

Bedrock Topography and Internal Stratigraphy of the Siple Dome Summit

A.M. FISHER, R.W. JACOBEL, N.M. SUNDELL
Physics Department, St. Olaf College, Northfield, MN 55057

A.M. GADES
Geophysics Program, University of Washington, Seattle, WA 98195

ABSTRACT

Radar studies of a 10-km square grid centered on the Siple Dome summit were conducted during the 1994–95 Antarctic field season as a part of a collaboration among the University of Washington, St. Olaf College and the University of Colorado (Fig. 1). The goals of this project are to use remote sensing, ground-based surveys, and ice-penetrating radar to study the ice dynamics and history of the region. The radar surveys show a maximum ice thickness is 1010 m, having a generally flat bed beneath. To first order, the internal stratigraphy reflects the surface topography, which is two-dimensional with slopes to the north and south of the ridge crest. We have produced contour and mesh maps of the bedrock, surface and two of the more prominent internal layers beneath the dome as a part of modeling studies being carried out at the University of Washington. The internal layers show an upwarping beneath the summit ridge that is slightly more pronounced at greater depth in accord with model calculations. There is also a pronounced asymmetry in the slope of the internal layers, with larger values toward the north, which may be related to differences in accumulation across the dome. These slopes, however, are not constant with depth, implying a possible change in the accumulation pattern with time.

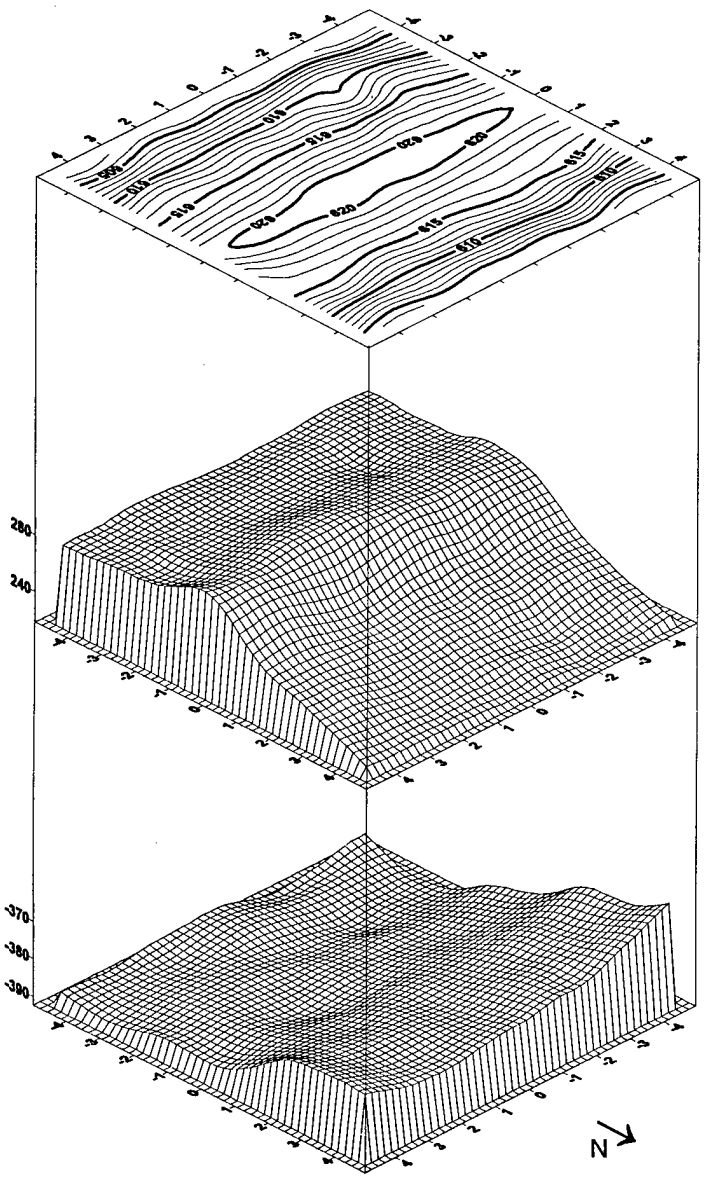

Figure 1. Surface and bedrock topography near the summit of Siple Dome as determined by radar profiling and GPS. Elevations are given in meters above (and below) sea level. Also depicted is the structure of one prominent internal reflector at approximately 40% of the ice thickness.

Mass Balance of the Glaciers in Taylor Valley, McMurdo Dry Valleys, Antarctica

ANDREW G. FOUNTAIN
U.S. Geological Survey, MS-412, PO Box 25046, Denver, CO 80225

GAYLE L. DANA
Desert Research Institute, 7010 Dandini Blvd, Reno, NV 89512

KAREN J. LEWIS
INSTAAR, Campus Box 450, University of Colorado, Boulder, CO 80309

ABSTRACT

Mark F. Meier established many fundamental methods and concepts for assessing the mass balance of glaciers. We applied these techniques to the mass balance of four glaciers within Taylor Valley (Fig. 2) one of the McMurdo Dry Valleys, Antarctica. The annual mass change of the glaciers in Taylor Valley is small, on the order of 10 cm water equivalent, averaged over the glacier surface. The small annual balance results from small exchanges of mass by accumulation and ablation. Ablation occurs during all seasons, with about two-thirds of the annual ablation taking place during the austral summer. Summer ablation is dominated by evaporation–sublimation, which accounted for roughly 70% of the mass loss during the 1994–1995 season. Much of the remaining ablation is meltwater, and calving from the margins accounts for perhaps 1–2%. Non-calving ablation from the ice cliffs, which form the margin of the glacier, is often three to five times the ablation from the top of the glacier. For accumulation, more snow falls during the winter season. Usually, accumulation during a single event does not exceed about 1 cm of snow, and a few major events during the year can compensate for the annual mass loss.

Spatial variation in the mass balance of the glaciers reflects their sensitivity to a spatially changing local climate (Fig. 1). This result is supported by the variation in long-term Equilibrium Line Altitude (ELA), which increases over the 50-km length of Taylor Valley. We believe that these changes result from a gradient of decreasing precipitation up-valley. Also, the ELA is higher for the north-facing glaciers in the Kukri Hills than for the south-facing glaciers across the valley in the Asgaard Range, which is probably related to differences in solar radiation caused by differences in the solar angle.

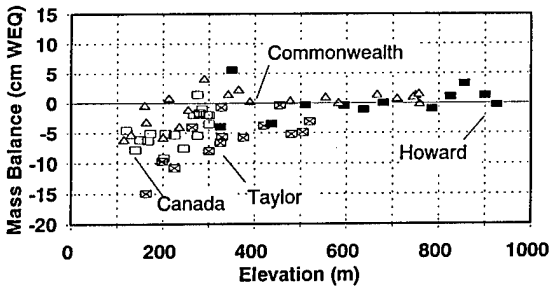

Figure 1. Summer (1994–1995) mass balance values for all the glaciers measured.

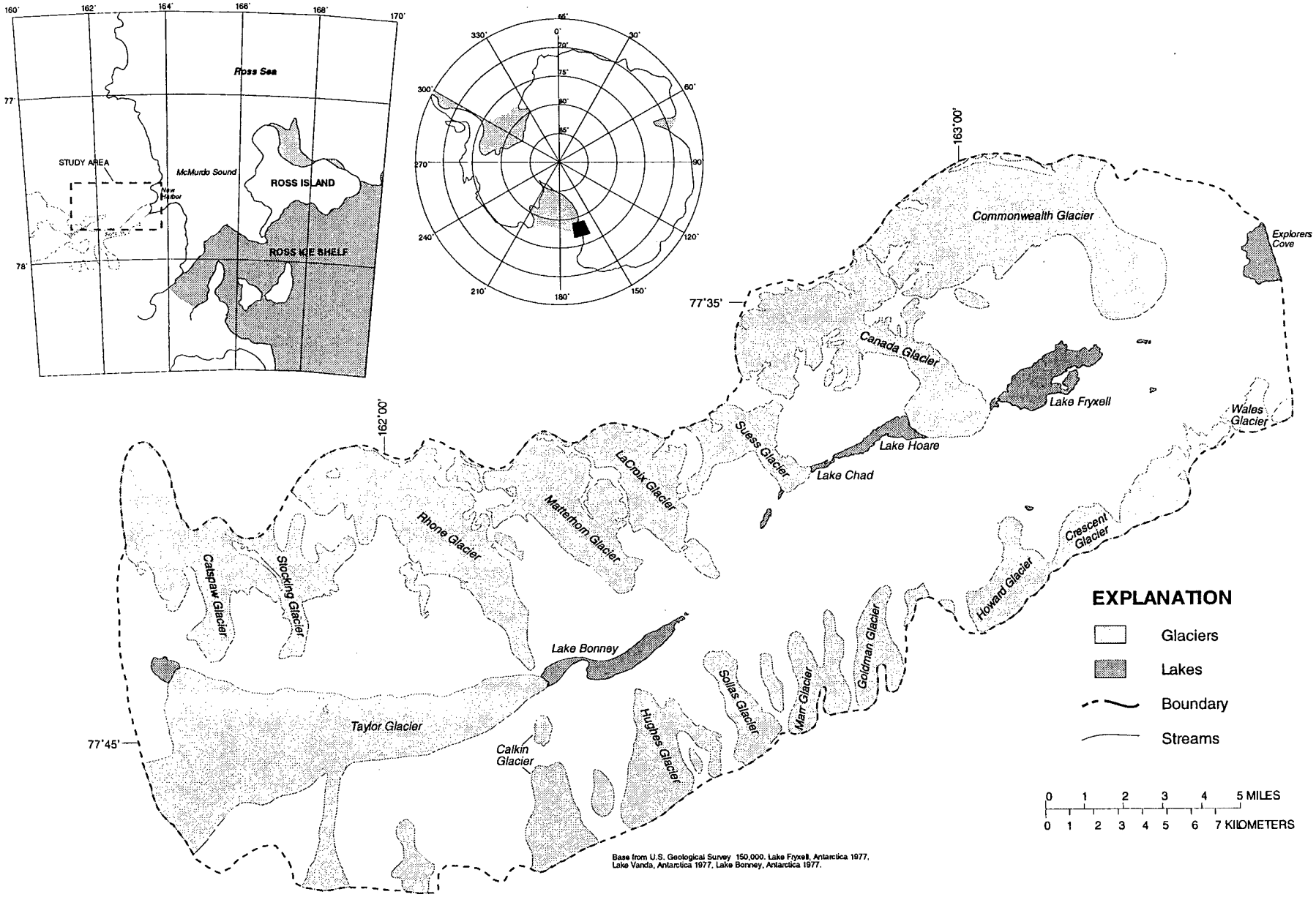

Figure 2. Base map and location of glaciers in Taylor Valley, Antarctica.

A Mechanism for the Generation of Flow Stripes on Ice Streams

G. HILMAR GUDMUNDSSON
VAW-ETHZentrum, Gloriastrasse 37/39, CH-8092 Zurich, Switzerland

ABSTRACT

An analytical model based on perturbation methods is used to calculate three-dimensional transient flow perturbations caused by either bedrock undulations or spatial variations in resistance to basal sliding. If the mean basal sliding velocity is a few thousand times larger than the mean deformational velocity, as is common for fast-moving ice streams, a long and narrow linear surface undulation is created in the wake of a local basal irregularity. This type of a surface undulation resembles closely the commonly observed flow stripes on the surfaces of fast flowing ice streams.

INTRODUCTION

Among the most striking surface features of many ice streams are long and narrow "flow stripes" that manifest themselves as linear surface undulations with relative elevations of a few meters (Bindschadler 1993). These features have also been called "flow lines," "flow traces" and "stream lines." Although a number of possible explanations have been put forward (see Merry and Whillans 1993), no flow model capable of generating flow stripes directly from some fundamental principles has, until now, been presented.

ANALYTICAL FLOW MODEL

Perturbation methods are used to calculate analytical transfer functions for three-dimensional transient perturbations in ice flow (Gudmundsson 1995). The perturbations can be caused by both bedrock protrusions as well as spatial variations in resistance to basal sliding. Derivation of the solutions is too lengthy to be included here.

Previous work using similar or related methods has focused on flow perturbations caused by basal undulations. Hutter (1983) calculated two-dimensional linear and nonlinear steady-state transfer functions. Reeh (1987) considered the three-dimensional steady-state problem for a linear ice rheology without basal sliding, and Johannesson (1992) calculated linear and nonlinear two-dimensional time-dependent transfer functions and linear three-dimensional steady-state transfer functions incorporating basal sliding. For prescribed basal sliding velocities along a straight bed-line, two-dimensional steady-state transfer functions for a linear medium have also been calculated (Balise and Raymond 1985).

In the model used here, a linear ice rheology with a constant viscosity is assumed. Since the actual rheological behavior is expected to be nonlinear with a strong depth-dependent effective viscosity, this set of assumptions makes it impossible to draw accurate quantitative conclusions from the results. The relevant physics controlling the genesis of flow stripes is presumably, nevertheless, included. The theory, for example, allows for high sliding velocities, and for stress variations over length scales comparable to the mean ice thickness.

The sliding law used is of the type $u_b = C(x, y)\tau_b$, where u_b is the basal flow velocity, τ_b is the basal shear stress, and (x, y) is a point on the glacier bed.

The perturbation solutions are valid for "small" perturbations, which restricts the amplitude of the basal undulations to a small fraction of the mean thickness. The amplitude of the variation in $c(x, y)$ must also be small compared to the mean value of $c(x, y)$.

Because of the use of the discrete inverse Fou-

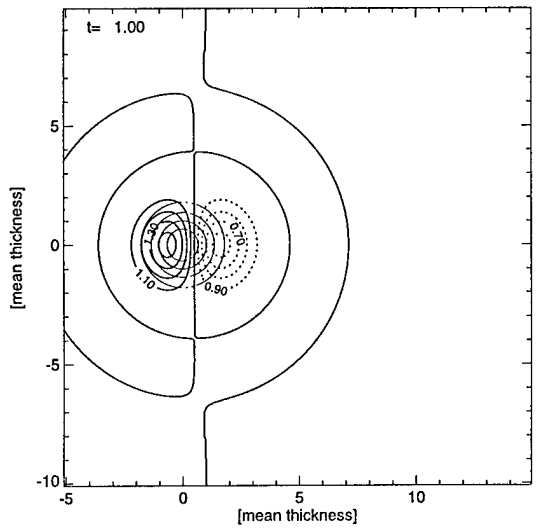

Figure 1. Transient surface amplitude in response to a three-dimensional flow over a Gaussian bump at the time t = 1. *At* t = 0 *the ice started to flow. The time unit is the ratio of the mean ice thickness to the mean surface velocity. The mean flow is from left to right. Contour intervals are 0.1. The solid contour lines represent higher than average surface elevation (that is, higher than 1), whereas the dotted ones represent lower than average elevation. The thin dash–dotted lines are the altitude lines of the Gaussian shaped basal peak responsible for the flow perturbations.*

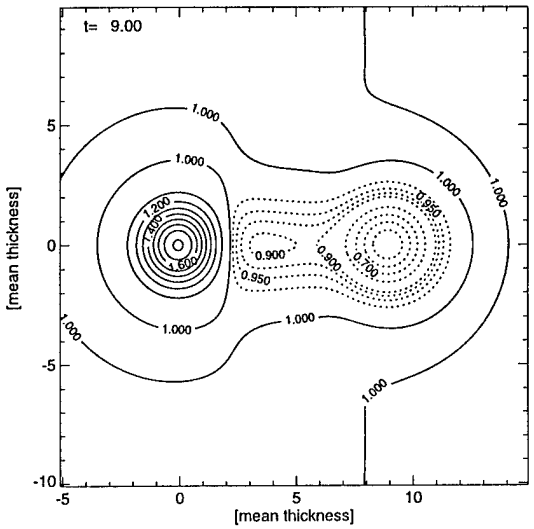

Figure 3. Steady-state surface elevation in response to a three-dimensional flow over a Gaussian bump (not shown) at the base. Contour intervals are 0.1 for values higher than 1 (solid lines), and 0.01 for values lower than 1 (dotted lines). The single dotted contour line at the up-flow side of the surface rise results from the periodicity of the model (caused by the use of the discrete Fourier transform). The calculated model is 2.56 times greater (in both spatial directions) than the part shown.

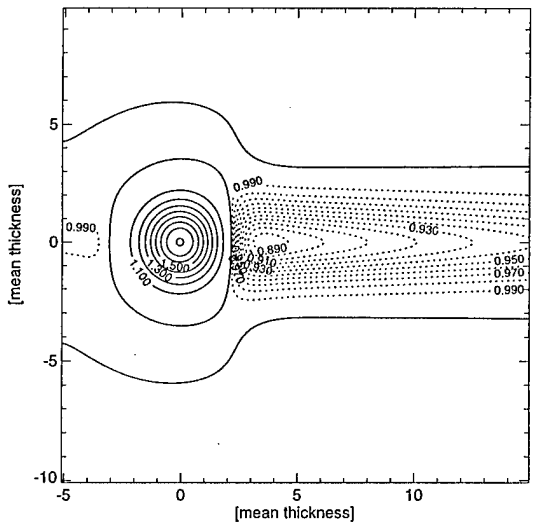

Figure 2. Surface elevation in response to a three-dimensional transient flow over a Gaussian bump (not shown) at the base at the time t = 9. *Contour intervals are 0.1, except for the range from 0.9 to 1.0, where the contour intervals are 0.25.*

rier transform in calculating the solutions, the region for which the flow is calculated becomes periodic and extends in periodic fashion to infinity in both spatial directions.

MODEL RESULTS

As an example of a generation of a flow stripe resulting from a flow over and around a basal undulation, the surface response to a flow over a Gaussian-shaped basal peak is given in Figures 1 to 3. All three figures correspond to the same set of flow parameters, thought to be typical of active ice streams. The mean basal sliding velocity is 5000 times larger than the mean surface deformational velocity, and the mean surface slope is taken to be 0.1°. The shape of the Gaussian bump together with the resulting surface undulations can be seen in Figure 1.

The mean ice thickness is set equal to one spatial unit, and all distance scales are in this unit. The mean surface velocity is also set equal to unity.

The amplitudes of the induced flow perturbations scale linearly with the amplitude of the Gaussian bump at the base, and its amplitude is arbitrarily set equal to the mean ice thickness. This means that for a Gaussian peak having, for example, an amplitude corresponding to 10% of the mean ice thickness, the amplitudes of all perturbations in Figures 1 to 3 have to be multiplied by the factor 0.1.

To illustrate the transient behavior, the ice stream is set to flow at the time $t = 0$. Figures 1 and 2 depict the resulting surface undulations 1 and 9 time units later. The time unit is the ratio of the mean thickness to the mean surface velocity. For an active Siple Coast ice stream, a typical time unit corresponds to about 2 years. Figure 3 gives the steady-state limit.

Figure 1 shows that a surface rise is created upstream of the basal bump, and that a surface trough is formed at the downstream side. In Figure 2 the surface trough has been advected downstream with a velocity almost identical to the mean surface velocity. A linear surface depression is left in the wake of the traveling surface trough. Eventually (Fig. 3), the surface trough vanishes by diffusion, and all that is left is the linear surface depression, which has a striking similarity to a flow stripe of the type observed on ice streams.

Note that reversing the amplitude of the basal peak will, instead of creating a flow stripe having a less than average elevation, create a flow stripe that rises above the surrounding ice.

DISCUSSION

A flow stripe will not form if a more moderate ratio of basal sliding to the internal deformational velocity (less than 100 for example) is used. This is in accordance with the observation that, in general, no flow stripes are found outside of ice stream margins. Flow stripes found on slow-flowing ice sheets or on inactive ice streams are presumably relics of a former flow regime.

There are two different time scales that control the transient behavior: a diffusion time scale t_d, and a propagation time scale t_p. t_d determines how fast the amplitude of a flow perturbation changes with time, and t_p is directly related to the time it takes for a sinusoidal perturbation to move a distance of one wavelength. Both time scales are functions of the longitudinal and the transversal wavelengths, as well as the relative amount of sliding with respect to internal deformation. It is the ratio t_p/t_d that determines how many wavelengths a sinusoidal flow perturbation travels before it decays through diffusion, therefore causing the appearance or the nonappearance of flow stripes of the type depicted in Figure 3. This ratio t_p/t_d does not depend on the nature of the externally applied perturbation. It is, for example, the same whether the surface undulation is caused by a spatial variation in resistance to basal sliding, or a basal bump. The shape of the resulting surface undulation does, however, depend on the nature of the basal irregularities causing the flow perturbations. For a sliding law of the form $u_b\ (x, y) = c(x, y)\tau_b\ (x, y)$, a Gaussian shaped variation in $c(x, y)$ (of the same form as the bedrock bump causing the flow perturbations seen in Fig. 1–3) creates flow perturbations having a much larger spatial extent.

The diffusion time scale is found to be strongly affected by short-scale stress gradients, in such a way that it becomes several orders of magnitudes larger than otherwise expected by extrapolating the long wavelength behavior to short distance scales. For two dimensions this theoretical result has previously been derived by Jóhannesson (1992). This fact could explain why flow stripes, such as those on Ice Stream C, exists for a long time after the ice stream has become inactive.

CONCLUSION

Flow stripes, of the type observed on the surface of many ice streams, are generated automatically whenever a viscous medium flows over some sufficiently strongly localized basal irregularities at high sliding velocities. Bedrock protuberances, as well as spatial variations in resistance to basal sliding over a flat bed, can generate such surface features. These subglacially induced flow stripes will only form if basal sliding velocities are at least a few hundredth times larger than deformational velocities, and are, therefore, not generated on ice caps and valley glaciers. Although the genesis of the flow stripes requires fast flow, the increase of the diffusion time scale at short wavelengths makes it possible for the flow stripes to exist for a significant time after an abrupt change in flow mode towards low flow velocities.

ACKNOWLEDGMENTS

Most of the theoretical work on which this paper is based was done during a one year visit

at the Geophysical Program, University of Washington. I benefited greatly from numerous discussions with C. F. Raymond. This work was supported by the Swiss Science Foundation grant 2-77-015-91.

LITERATURE CITED

Balise, M.J. and C.F. Raymond (1985) Transfer of basal sliding variations to the surface of a linearly viscous glacier. *Journal of Glaciology,* **31**(109): 308–318.

Bindschadler, R.A. (1993) Siple Coast project research of Crary Ice Rise and the mouths of Ice streams B and C, West Antarctica: Review and new perspectives. *Journal of Glaciology,* **39**(133): 538–552.

Gudmundsson, G.H. (1995) Effects of basal sliding variations on the topography and the surface velocity of ice streams. Final report for the Swiss National Science Foundation, unpublished.

Hutter, K. (1983) *Theoretical Glaciology: Material Science of Ice and the Mechanics of Glaciers and Ice Sheets.* Tokyo: D. Reidel Publishing Company, Terra Scientific Publishing Company.

Johannesson, T. (1992) Landscape of temperate ice caps. Ph.D. thesis, University of Washington.

Merry, C.J. and I.M. Whillans (1993) Ice-flow features on Ice Stream B. Antarctica, revealed by SPOT HRV imagery. *Journal of Glaciology,* **39**(133): 515–552.

Reeh, N. (1987) Steady-state three-dimensional ice flow over an undulating base: First-order theory with linear ice rheology. *Journal of Glaciology,* **33**(114): 177–185.

Ice–Volcano Interaction at the Subglacial Grímsvötn Volcano, Iceland

MAGNÚS T. GUDMUNDSSON
Science Institute, University of Iceland, Dunhaga 3, 107 Reykjavík, Iceland

ABSTRACT

For at least two centuries, volcanic activity in Grímsvötn has been characterized by frequent small eruptions within the composite Grímsvötn caldera and larger, less frequent, fissure eruptions outside the caldera. The caldera eruptions take place within a subglacial lake and rapidly melt the ice above the vents, forming openings in the ice shelf covering the lake. Mounds of hyaloclastites are piled up at the vents, attaining elevations similar to the lake level. The volume of ice melted during these eruptions is less than 0.1 km^3. In contrast, the fissure eruption in 1938, which occurred to the north of the Grímsvötn caldera, melted 2 km^3 of ice over several days as a subglacial hyaloclastite ridge with a volume of 0.3–0.5 km^3 was formed. Simultaneously, meltwater was drained away in a jökulhlaup. In eruptions that break through the ice cover, it appears that the water level at the eruption sites controls the elevation of ridges and mounds formed. For eruptions that penetrate the ice cover outside the caldera, this water level seems to lie several hundred meters below the ice surface prior to eruption. Locally enhanced melting of ice at eruption sites suggest that thermal effects of individual eruptions last 5–20 years.

INTRODUCTION

Over the last several hundred years, many eruptions have occurred within ice caps covering parts of the volcanic zones in Iceland (e.g., Thorarinsson 1974, Björnsson and Einarsson 1990). Outside the areas currently covered with ice, hyaloclastite ridges and table mountains formed under ice during the Pleistocene glaciation are common landforms. Ice–volcano interaction is therefore an integral part of volcanism in Iceland, and jökulhlaups and fallouts of tephra from eruptions within ice caps pose hazards to some areas. In this paper the focus will be on eruptions at the subglacial Grímsvötn volcano. Various data are used to define the characteristics of eruptions. These data include the bedrock topography at eruption sites, data on temporal changes in ice cover and observations of the most recent eruptions. Parts of the work reported have appeared earlier in Gudmundsson and Björnsson (1991).

THE GRÍMSVÖTN VOLCANO

The Vatnajökull ice cap (8300 km^2) covers the central part of the Eastern Volcanic Zone, including several active volcanoes. The most active of these is Grímsvötn in the central part of Vatnajökull. Geothermal and volcanic activity at Grímsvötn has greatly modified the ice surface topography, creating a 10- to 12-km-wide and 200- to 300-m-deep depression. The Grímsvötn depression is a separate ice drainage basin with an area of 160 km^2 (Björnsson 1988). Within the depression a subglacial caldera lake is located, covered by an ice shelf that is 250 m thick. Ice flows into the Grímsvötn lake where it is melted at the base of the ice shelf. This results in a rising lake level, eventually leading to a jökulhlaup that partly drains the lake (Thorarinsson 1953, Björnsson 1974). Jökulhlaups occur on average once every 5 years and the volume drained in each event has varied from 0.6 to 4.7 km^3 (Gudmundsson et al. 1995). The whole of the Grímsvötn basin is at an elevation well above that of the present equilibrium lines on Vatnajökull. Therefore, basal melting by geothermal heat controls its mass balance; surface ablation plays only a minor role (Björnsson 1974, Björnsson and Gudmundsson 1993).

Calorimetric estimates based on water accumulation in Grímsvötn yield a geothermal power of several thousand megawatts (Björnsson et al. 1982, Björnsson 1983, Björnsson and Gudmundsson

1993). Fluctuations in geothermal power are closely related to fluctuations in volcanic activity. These fluctuations control the mass balance of the Grímsvötn basin, and a reduction in volcanic activity in the latter half of the 20th century has resulted in the buildup of ice in the area and a reduction in the volume of jökulhlaups (Gudmundsson et al. 1995).

The ice cover in the Grímsvötn area is 300–700 m thick but rocks outcrop at the southern rim of the composite Grímsvötn caldera. Exposed rocks in the caldera fault are basaltic tuffs with dikes and sills in places. The subglacial topographic expression of the Grímsvötn volcano is a complex of ridges and mounds, covering an area 10–15 km in diameter and rising 300–800 m above the surrounding bedrock (Björnsson 1988). The subglacial lake is located within the caldera, which has in recent times been the center of geothermal and volcanic activity.

ERUPTIONS

Over the last 400 years, activity has fluctuated, but eruptions have, on average, occurred once every 10–20 years (Thorarinsson 1974, Björnsson and Einarsson 1990). Since 1938, only one minor eruption has been observed, making the latter part of the 20th century the most quiet period since 1600 A.D. Despite the frequent eruptions, direct observations of eruption sites only exist for the eruptions of 1934, 1938 and 1983 (Áskelsson 1936, Nielsen 1937, Thorarinsson 1974, Grönvold and Jóhannesson 1984). Two of these were small eruptions within the caldera (1934 and 1983), while the eruption in 1938 was a large, almost entirely subglacial, fissure eruption to the north of the caldera.

Caldera eruptions

The craters of the eruptions in 1934 and 1983 were located underneath the southern rim of the caldera (Fig. 1 and 2). In 1934 three craters were active, but two of these were small, with minor activity compared to the main crater.

The beginning of the eruption in 1934 was marked with an earthquake swarm. The bedrock at the eruption site at its start was at least 100 m below the lake level, but the thickness of the ice shelf was 50–80 m. Apparently, the eruption melted its way through the ice shelf in less than half an hour, the time between the first recorded

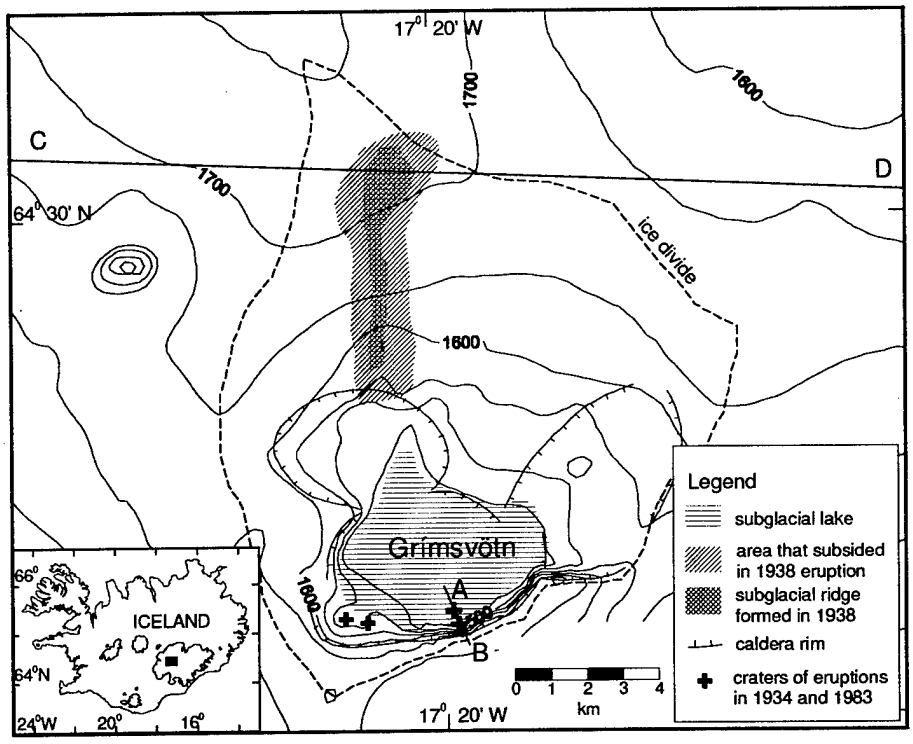

Figure 1. Ice surface topography in the Grímsvötn area (after Björnsson et al. 1992) showing the location of the subglacial lake and the eruption sites in 1934, 1938 and 1983. The cross-sections shown on Figures 2 (A–B) and 3 (C–D) are indicated.

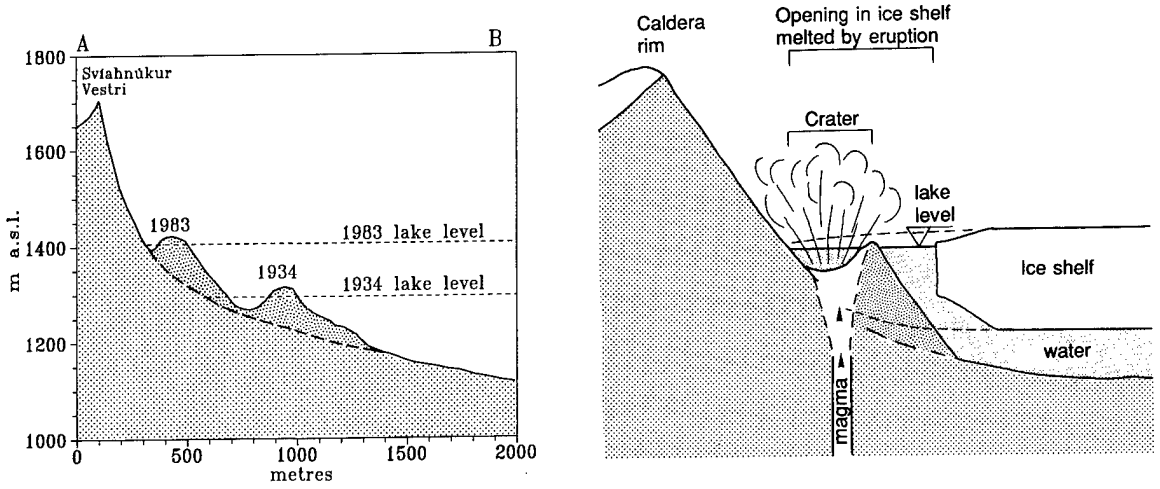

Figure 2. Mounds formed in caldera eruptions. Right: The mounds formed in the eruptions in 1934 and 1983. Left: A schematic cross-section showing the relationship between the ice shelf, lake level and the erupting crater (from Gudmundsson and Björnsson 1991).

earthquake (of magnitude 4-$^1/_2$ on the Richter scale) and the first sighting of an eruption column (Tryggvason 1960). The eruption column was seen from various parts of Iceland for 8 days and fallout of tephra was detected 100–150 km to the north and the east of Grímsvötn (Thorarinsson 1974). Some activity was still taking place 15 days after the start of the eruption (Áskelsson 1936) but 2 weeks later the eruption had ceased (Nielsen 1937). At the main eruption site, the opening formed in the ice shelf was elongated along the caldera wall, being about 1000 m long and 500 m wide. Smaller openings were at other two craters. The total volume of ice melted during the eruption was 40–50 $\times$ 10^6 m^3. Within the large opening, a pile of hyaloclastites had formed (volume 15–20 $\times$ 10^6 m^3), considered to be the rim of the crater (Fig. 2). Data on the eruption are summarized in Table 1.

The eruption in 1983 was also preceded by an earthquake swarm and 8 hours elapsed from the seismically estimated start of the eruption until an eruption column was seen (Einarsson and Brandsdóttir 1984). A relatively long subglacial phase in 1983 compared to 1934 was probably attributable to the combined effects of lower effusion rate and thicker ice cover in 1983. The opening formed had a diameter of 500 m and the volume of ice melted was 20–30 $\times$ 10^6 m^3. A mound of hyaloclastites, with a volume of 6–8 $\times$ 10^6 m^3, was formed within the opening. The eruption lasted for 5–6 days and fallout of tephra was minute, covering only a few square kilometers close to the vent (Grönvold and Jóhannesson 1984).

A minor volcanic event, lasting for about an hour, may have taken place in 1984 according to seismic data (Björnsson and Einarsson 1990). Lo-

Table 1. Data on three Grímsvötn eruptions. Based on Thorarinsson (1974), Tryggvason (1960) and Einarsson and Brandsdóttir (1984).

	No. vents	*Volume erupted (10^6 m^3)*	*Duration of eruption (days)*	*Duration of sub-glacial phase (hours)*	*Ice melted during eruption (10^6 m^3)*
1934	3	30–40	15–30	≤0.5	40–50
1983	1	10	5–6	8	20–30
1938	8 km fissure	300–500	>7	>6 days	≥2000

cally enhanced melting was not observed in Grímsvötn in relation to this event.

Cooling of the material erupted in 1983 took some years. Heat derived from the mound and underlying dike sustained the opening in the ice shelf for about a year. In 1987, four years after the eruption, ice melting at the eruption site was still high compared to the values before 1983. By 1991, however, ice flow had closed the opening and signs of elevated heat flow had declined. Observations after the 1934 eruption suggest similar thermal effects.

Neither the 1934 nor the 1983 eruptions sparked off a jökulhlaup from Grímsvötn. The eruption sites were located within the lake, and melting of floating ice does not affect the lake level. Comparison of the volume of ice melted during these caldera eruptions (0.02–0.05 km^3) with that drained in typical jökulhlaups also suggests that their effect on the size and general behavior of the jökulhlaups is minor. However, for some eruptions the reverse may be true, i.e., the release of overburden pressure when the lake is drained may have triggered eruptions (Thorarinsson 1953). Most Grímsvötn eruptions of the 19th and early 20th century seem to have been sparked off in this way. The eruption in 1934 falls into this category since it started at the end of a jökulhlaup when the lake level had fallen about 100 m. This interaction of the caldera lake and the presumed shallow magma chamber in the crust is a feedback mechanism: The periodic variations in overburden pressure cause periodic tapping of the magma chamber. The magma brought to the surface and intruded into the shallow crust supplies heat to the hydrothermal system that sustains the caldera lake by melting of ice. This mechanism has not produced eruptions since 1934, but earthquakes near the ends of jökulhlaups in 1954 and 1960 (Tryggvason 1960) may have been caused by intrusive activity of this nature.

Fissure eruption in 1938

In 1938 a large and unusually sudden jökulhlaup started on 23 May, reached a peak on 26 May and then receded slowly in about 10 days. Aerial inspection took place on 28 May, revealing the cause of the jökulhlaup: A depression with a volume of 2 km^3 (8 km long, 2 km wide and 100–150 m deep) had formed in the ice surface to the north of the Grímsvötn caldera (Fig. 1). A several-hundred-meters-deep hole was located in the northern end of the depression. Meltwater had drained from underneath the depression, into the Grímsvötn lake that was 30–40 m below its critical jökulhlaup level (Gudmundsson et al. 1995). The subsequent steep rise in lake level, possibly coupled with elevated temperature of the meltwater (Björnsson 1992), sparked off the jökulhlaup.

The depression is thought to have been formed by a subglacial fissure eruption. It only broke the surface of the ice at one location, near the termination of activity, forming a small tephra layer that stained a part of the depression. The ice thickness in the area is 400 to 700 m and radio-echo soundings have revealed a 70- to 200-m high bedrock ridge (volume 0.3 to 0.5 km^3) that coincides with the depression (Fig. 1 and 3; Table 1). A common landform in the now ice-free areas of the volcanic zones in Iceland are hyaloclastite ridges formed in fissure eruptions during the Pleistocene glaciation. From analogy, Gudmundsson and Björnsson (1991) concluded that the observed subglacial ridge was formed in the 1938 fissure eruption.

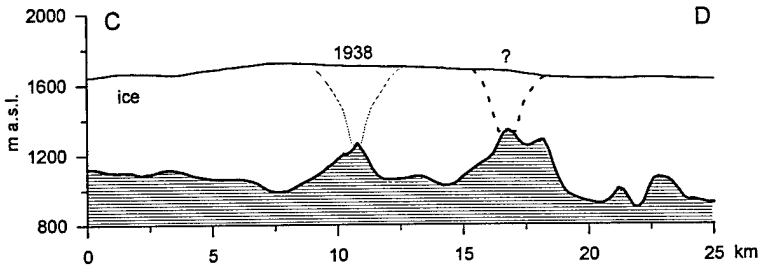

Figure 3. Subglacial ridges to the north of Grímsvötn, formed in fissure eruptions. The approximate form of 1938 ice depression is shown and a broken line shows the likely form of a depression created in the eruption that piled up the ridge at 17 km. Ice surface and bedrock topography from Björnsson et al. (1992).

If earthquakes occurred during this eruption, their magnitude was less than $3\text{-}^1/_2$, the detection limit for the area at the time (Brandsdóttir 1984). Thus, the beginning of the eruption cannot be timed, except that it must have started before 23 May, the time of the onset of the jökulhlaup. Ice surface and bedrock topography to the north of Grímsvötn is such that accumulation of large volumes of water at the eruption site is unlikely. Meltwater was probably drained quite fast southwards into the Grímsvötn lake. Since basaltic eruptions usually have the highest effusion rate soon after the start (Wadge 1981), it is to be expected that melting was most vigorous in the first days of the eruption. It is, therefore, probable that a delay attributable to the buffering effect of the Grímsvötn lake was probably no greater than a few days.

The total heat content of the basaltic magma required to form a 0.4-km^3 ridge is more than sufficient to melt 2 km^3 of ice (Gudmundsson and Björnsson 1991). By assuming that the magma was quenched as glass, the total specific heat of the magma can melt 2.5–3 km^3 of ice. The latent heat would then be released gradually during alteration of the glass to palagonite. If all the magma was crystallized as pillow lavas, the latent heat of the magma would have been released as well as the specific heat. If so, the total heat available would have been sufficient to melt about 4 km^3.

The depth of the depression in the ice surface decreased rapidly after 1938. In 1946, the northernmost part still had some crevasses and a clear depression is evident on air photos from 1954. Apparently, some subglacial melting was still taking place at the eruption site 16 years after the event. Irregularities in jökulhlaup frequency and volume in the decade following the 1938 eruption may be explained by frequent draining of meltwater from small subglacial vaults above a cooling hyaloclastite ridge (Gudmundsson and Björnsson 1991).

A few earlier eruptions are known to have occurred to the north of Grímsvötn. The eruptions in 1684–1685 (Thorarinsson 1974) and 1867 (Björnsson 1988) may fall into this category. The bedrock in this area has many subglacial ridges, some of which may have been formed in these eruptions (Fig. 3). Common to all the ridges is that the ice thickness above the highest points is at least 300–400 m, which is similar to the ice thickness above the ridge considered formed in 1938. The ash-producing eruptions must melt holes through the ice cover and the water level in these holes probably controls the elevation of the ridges formed. Thus, the elevation of the ridges suggests that the vents dispersing tephra over the area were located in deep depressions (Fig. 4). This further suggests that during eruptions of this type, melt-

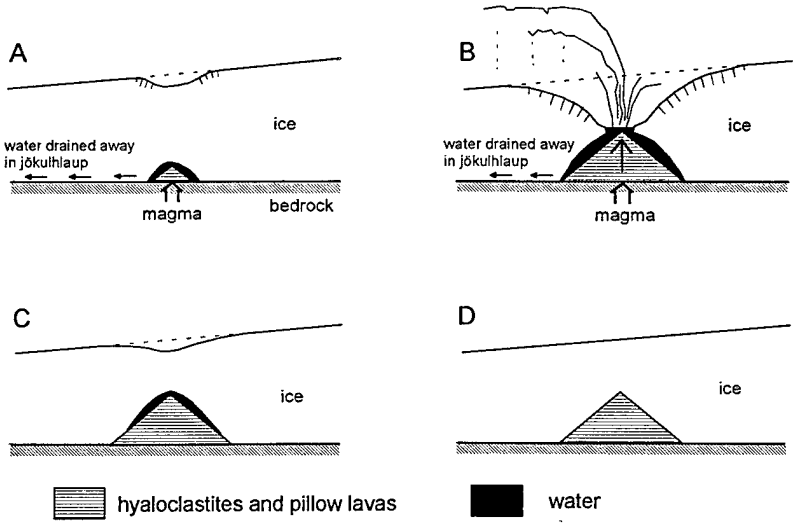

Figure 4. Schematic cross-sections illustrating the different stages in the formation and cooling of a hypothetical subglacial ridge. Eruptions may be entirely subglacial and terminate before reaching stage B. In stage C some localized melting still takes place while in D the ridge has lost all its heat. Stages A and B apparently take several days or weeks while stage C may last decades.

water is quickly drained away from the vents and collapse of the overlying ice creates the deep depressions. Were eruptions of this type to continue after breaking through the ice cover, subaerially erupted lavaflows might eventually cap the hyaloclastites. The table mountains of the volcanic zones in Iceland are thought to have formed in this way during the Pleistocene. No table mountains have been found in studies of the bedrock topography of the Grímsvötn area (Björnsson 1988), suggesting that eruptions usually terminate before subaerially erupted lavas form.

CONCLUSIONS

1. Individual eruptions, lasting several days or weeks, may quickly melt large volumes of ice, demonstrating the highly efficient heat transfer from magma to ice. These eruptions create local depressions in the ice. The depressions disappear gradually, suggesting that the thermal effects of individual eruptions last for 5–20 years.

2. A feedback mechanism involving eruptions and jökulhlaups may have existed in Grímsvötn. Apparently, a decrease in load by a rapidly lowering lake level during jökulhlaups sparked off eruptions within the caldera. In turn the heat from the erupted material and associated shallow intrusions increased the geothermal power, sustaining the high level of ice melting.

3. The products of the observed subaqueous and subglacial eruptions in Grímsvötn are ridges and mounds of hyaloclastites. The maximum elevation of these formations is controlled by the ambient water level at the eruption site. Within the caldera this level is that of the lake. Elsewhere, it is the water level within deep depressions in the ice formed by rapid ice melting and efficient draining of meltwater. A large fraction of the material erupted after the pile of hyaloclastites has reached the water level is carried away as airborne tephra.

ACKNOWLEDGMENTS

Helgi Björnsson introduced me to the study of subglacial volcanoes and his advice and support is greatly appreciated. A review by Gudrún Larsen improved the manuscript.

LITERATURE CITED

Áskelsson, J. (1936) On the last eruptions in Vatnajökull. Reykjavík: Soc. Sci. Isl., 18, 68 p.

Björnsson, H. (1974) Explanation of jökulhlaups from Grímsvötn, Vatnajökull, Iceland. *Jökull,* **24:** 1–26.

Björnsson, H. (1983) A natural calorimeter at Grímsvötn: indicator of geothermal and volcanic activity. *Jökull,* **33:** 13–18.

Björnsson, H. (1988) Hydrology of ice caps in volcanic regions. Reykjavík: Soc. Sci. Isl., 45, 139 p.

Björnsson, H. (1992) Jökulhlaups in Iceland: prediction, characteristics and simulation. *Annals of Glaciology,* **16:** 95–106.

Björnsson, H. and P. Einarsson (1990) Volcanoes beneath Vatnajökull, Iceland: Evidence from radio-echo sounding, earthquakes and jökulhlaups. *Jökull,* **40:** 147–168.

Björnsson, H., and M.T. Gudmundsson (1993) Variations in the thermal output of the subglacial Grímsvötn caldera, Iceland. *Geophys. Res. Lett.,* **20:** 2127–2130.

Björnsson, H., S. Björnsson and T. Sigurgeirsson (1982) Penetration of water into hot rock boundaries of magma at Grímsvötn. *Nature,* **295:** 580–581.

Björnsson, H., F. Pálsson and M.T. Gudmundsson (1992) Vatnajökull, northwestern part, 1:100,000. Glacier surface and bedrock topography. Reykjavík: University of Iceland and the National Power Company.

Brandsdóttir, B. (1984) Seismic activity in Vatnajökull 1900–1982 with special reference to Skeiåarárhlaups, Skaftárhlaups and Vatnajökull eruptions. *Jökull,* **34:** 141–150.

Einarsson, P. and B. Brandsdóttir (1984) Seismic activity preceding and during the 1983 volcanic eruption in Grímsvötn, Iceland. *Jökull,* **34:** 13–23.

Grönvold, K. and H. Jóhannesson (1984) Eruption in Grímsvötn: Course of events and chemical studies of the tephra. *Jökull,* **34:** 1–11.

Gudmundsson, M.T. and H. Björnsson (1991) Eruptions in Grímsvötn, Vatnajökull, Iceland, 1934–1991. *Jökull,* **41:** 21–45.

Gudmundsson, M.T., H. Björnsson and F. Pálsson (1995) Changes in jökulhlaup sizes in Grímsvötn, Vatnajökull, Iceland, 1934–91, deduced from in-situ measurements of subglacial lake volume. *Journal of Glaciology,* **41:** 263–272.

Nielsen, N. (1937) Vatnajökull. Kampen mellem

ild og is [Vatnajökull. The fight between ice and fire]. Kõbenhavn: H. Hagerup, 123 p.
Tryggvason, E. (1960) Earthquakes, jökulhlaups and subglacial eruptions. *Jökull,* **10:** 18–22.
Thorarinsson, S. (1953) Some new aspects of the Grímsvötn problem. *Journal of Glaciology,* **4:** 267–274.
Thorarinsson, S. (1974) Vötnin Stríå. Saga Skeiåarárhlaupa og Grímsvatnagosa [The swift flowing rivers. The history of Grímsvötn jökulhlaups and eruptions]. Reykjavík: Menningarsjóur, 254 p.
Wadge, G. (1981) The variation of magma discharge during basaltic eruptions. *J. Volc. Geoth. Res.,* **11:** 139–168.

Short Wavelength Variations in the Horizontal Velocity Field of a Valley Glacier

J.T. HARPER, N.F. HUMPHREY
Department of Geology and Geophysics, University of Wyoming, Laramie, WY 82071

W.T. PFEFFER, B.C. WELCH
INSTAAR, University of Colorado, Boulder, Campus Box 450, Boulder, CO 80309

ABSTRACT

Repeated surveys of a dense grid of 64 stakes placed in a 0.13-km^2 reach of Worthington Glacier, Alaska, are used to characterize the short length scale (~10–15 m) variations in the surface flow field. The data collected cover four velocity intervals in a 67-day period, spanning the summer velocity peak (June) and subsequent slowdown of the glacier. During the velocity peak, the average down-glacier component of velocity is 20% greater than in late summer. The velocity field of the glacier shows spatial variability at two levels: 1) a regional flow field with structure related to far-field flow dynamics, and 2) a localized flow field with features that are confined in both time and space. Characteristics of the regional flow field include velocity contours that run parallel to a valley wall and perpendicular to an ice-fall. The spacing of these contours is such that important changes occur at the 10-m length scale. Localized variability in the flow field consists of events lasting less than a few weeks and affecting the 10- to 50-m length scale. Local variations are interpreted to be the result of surface crevassing. These variations are greatest during the velocity peak and diminish in proportion to velocity after the peak. Since both the regional and localized flow fields overlap in length scale, the finer details of the regional flow field are masked by localized transient events. This makes the task of measuring short term variations in the regional strain field difficult, and suggests that considerable care should be taken in interpreting short time variations in surface velocity measurements.

INTRODUCTION

The velocity at the surface of a temperate glacier results from the sum of the ice deformation rate and the speed of sliding of the ice mass along its basal boundary. Deconvolving a measured surface velocity into the two components of motion is a difficult task owing to an inadequate understanding of glacier flow processes. Moreover, accurately calculating the velocity at a point on a glacier's surface from geometrical considerations, such as slope and ice depth, is rarely possible. An important method for gaining a better understanding of glacier flow is to study the temporal and spatial variations in surface velocity. Observations of flow variations give insight into deformation and sliding processes, thus providing information needed to improve theory and models of glacier flow.

The existence of temporal and spatial variations in the flow field of valley glaciers is well established. Work, such as that by Meier (1960) and Raymond (1971), has documented large scale spatial variations along the length and across the width of valley glaciers. Temporal variations have been documented for a range of time scales—from decades to centuries, as with periodic surging (see Paterson 1994), to seasonal variations lasting

weeks to months (e.g., Hodge 1974, Brzozowski and Hooke 1981, Hooke et al. 1983, Hooke et al. 1989), to transient events occurring over hours or days (e.g., Iken and Bindschadler 1986, Kamb et al. 1994, Meier et al. 1994). These studies have all shown that surface velocities can be highly variable in time and space because of changes in both the stress field and the basal boundary conditions.

While a great deal of work has been directed at measuring high-resolution temporal variations in the surface flow field, velocity variations occurring over small distances have not been as well documented. This gap in knowledge provides the motivation for this paper. Here we investigate short wavelength variations in the down-glacier component of the velocity of a temperate valley glacier. Summer motion of a 0.13-km^2 reach of the glacier is characterized by repeated surveys of a grid of 64 surface stakes placed 20–30 m apart. Interpolation of velocity values between measurement stakes allows the velocity field to be examined at the length scale of ~10–15 m. The data collected allow investigation of both localized transient events and short length scale changes in the regional flow pattern.

STUDY REACH

Research was conducted on Worthington Glacier, an 8-km^2 temperate valley glacier located in the Chugach Mountains, Alaska (Fig. 1). Surface velocities were measured as part of a larger investigation of the glacier's three-dimensional velocity field, which includes internal deformation studies using a dense network of boreholes (Pfeffer et al. 1994). Details of the fully three-dimensional flow field will be published elsewhere. Other recent work on Worthington Glacier includes mapping of the bed with radio-echo sounding techniques (Welch et al., this volume), studies of the glacier's englacial and subglacial hydrology (Stone et al. 1994), and analysis of the dissolved and suspended sediment loads in the outlet streams (Anderson et al., in press).

The study reach covers a flat bench of the glacier located just below the its equilibrium line. The bench is bounded in both the up-glacier and down-glacier directions by large ice-falls, where the overall slope is in excess of 20° and the surface is severely broken. Ice radar and borehole drilling show that the glacier is 175–220 m thick along this bench (Welch et al., this volume). Video observations made in boreholes show that the bed of the study region has a variable character: ice is in contact with clean bedrock in some areas, while other areas have at least 20 cm of till between ice and bedrock (Harper and Humphrey 1995). The observations suggest that the bed varies between clean bedrock and till at a length scale of a few tens of meters.

METHODS

Stakes

In May of 1994, 64 stakes were placed in the study reach. The stakes, which were 6.1-m lengths

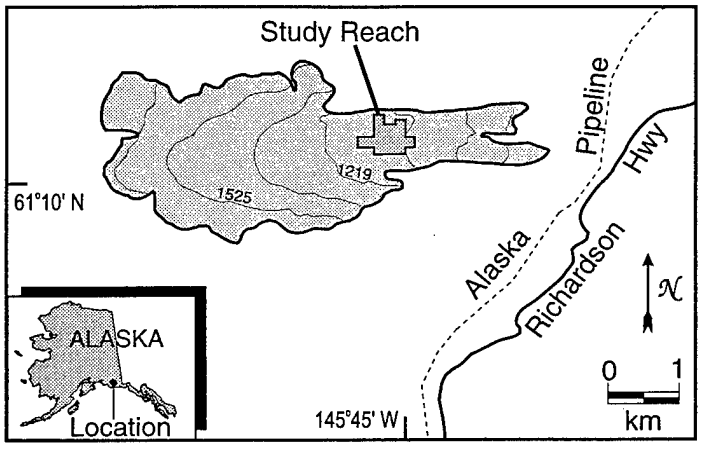

Figure 1. Worthington Glacier, Chugach Mountains, Alaska. Patterned area is glacier; contour interval is 152 m.

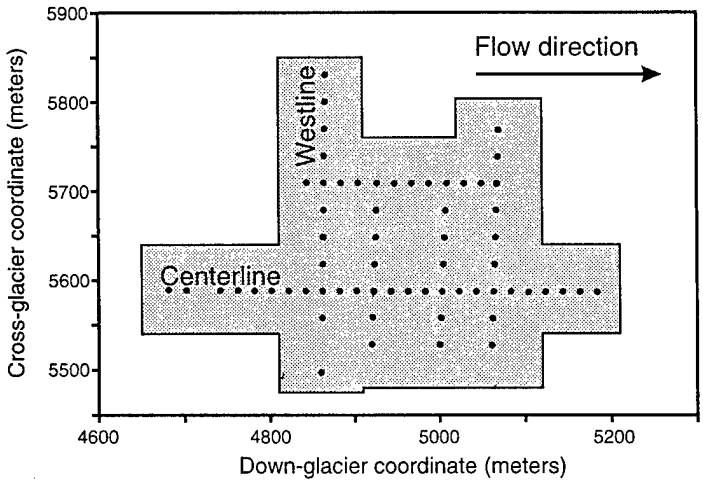

Figure 2. Study reach. Dots are locations of surface velocity stakes; Centerline and Westline are rows of stakes. Patterned area is region for which values are interpolated to a 10- × 10-m grid. Coordinates are in a local system.

of PVC pipe, were drilled into the glacier surface with a hot water drill. The ice surface was covered by 4–5 m of snow and the stakes were set so that their tops were initially flush with the snow surface. Thus, the lower 1–2 m of the stakes were anchored in glacier ice. Over time, snow melt and compaction exposed greater lengths of the stakes, making the flexible PVC pipe prone to tilting. To minimize this effect, the stakes were periodically cut to maintain their tops within 10–20 cm of the snow surface. The shortening of stakes was recorded and accounted for in the data reduction process.

Stakes were arranged in a grid of intersecting cross-glacier and along-glacier profiles (Fig. 2). The line of stakes labeled "Centerline" runs approximately along the glacier's kinematic centerline. The glacier's surface slope is nearly flat along the central and eastern portions of Centerline, but increases to over 10° as the western seven stakes extend up to the base of the upper ice-fall. The "Westline" traverses over half of the width of the glacier, from about 20 m from the north valley wall to south of Centerline.

Surveying

Surveys were made from one of two sites on the valley wall south of the glacier. The instrument used is a total-station theodolite, with a horizontal and vertical angular precision of 2 sec and an EDM precision of ± (2 mm + 2 ppm). Stake coordinates were determined by turning an angle from a fixed reference located on the north valley wall and measuring the distance to the stake. Since the instrument was calibrated to the reference between each measurement, errors do not propagate. Atmospheric corrections for the EDM were made internally by the instrument and will be in error if sampling of the air mass at the instrument does not adequately represent the average properties of air along the beam's travel path. A thermal gradient is likely to exist in the air near the glacier surface. However, the travel time through this zone is minimized by a steep vertical angle from the instrument to the reflector, and the survey sites' location on a ridge promontory gives a fair sampling of the air higher above the glacier.

Therefore, atmospheric effects give an error that we feel is less than ± 2 ppm. Two operational errors influence the measurement: 1) an error associated with centering of the top of the stake in the instrument cross hairs is estimated at ± 1 sec in the angular measurement, and 2) an error in properly locating the EDM reflecting prism at the stake gives an uncertainty of ± 3 cm to the distance measurement. Accumulating instrument and procedural errors gives an uncertainty of ± (3.2 cm + 4 ppm) to distance measurements and ± 3 sec to angular measurements.

The greatest distance from either of the survey sites to any particular stake is 840 m. At this distance, the above errors give an ellipse of uncer-

tainty in the coordinate of the stake that has foci of length 1.2 and 3.6 cm. The geometry is such that the long axis of the ellipse is oriented roughly across-glacier and the short axis runs along-glacier. Since velocity is calculated as the displacement between two surveys, the total uncertainty in any measurement of the down-glacier component of velocity is about ± 2.5 cm. With the displacement of stakes between surveys ranging from about 2–4.5 m over 11–28 d, the instrument error in calculated velocities is about 10% or less. This represents an upper limit for the error as the average distance to the stakes is 25% less than used here.

Data reduction

Five surveys of the stake grid were made over 67 days between late May and early August. This produces measurements of velocity over four separate stages as well as one long-term average. Data are reduced to three orthogonal components of velocity: x-direction (approximately down-glacier), y-direction (approximately across-glacier) and z-direction (vertical). Two-dimensional interpolation of velocity values is done by computer. A 10- × 10-m grid of values is calculated for the region defined in Figure 2 using an iterative interpolation scheme. First, every fourth grid node is estimated from the initial data by several averaging techniques, then the remaining grid nodes are filled in using a two-dimensional spline function. Biharmonic iterations with feedback from the initial data are used to distribute the curvature of the spline function so that the sum of the squares of the second derivative is minimized (Briggs 1974). This technique avoids the problems associated with data that are not located on grid nodes, honors the initial data points, and avoids introducing information that is not present in the data.

VELOCITIES

Regional velocity field

The flow field related to large scale flow dynamics, the regional flow field, is best revealed by long-time averaging of measurements. When the down-glacier component of velocity is averaged over the entire study period (late May to early August), the study reach shows several features important to the regional flow field (Fig. 3). Ice velocities are greatest below the ice-fall in the west-

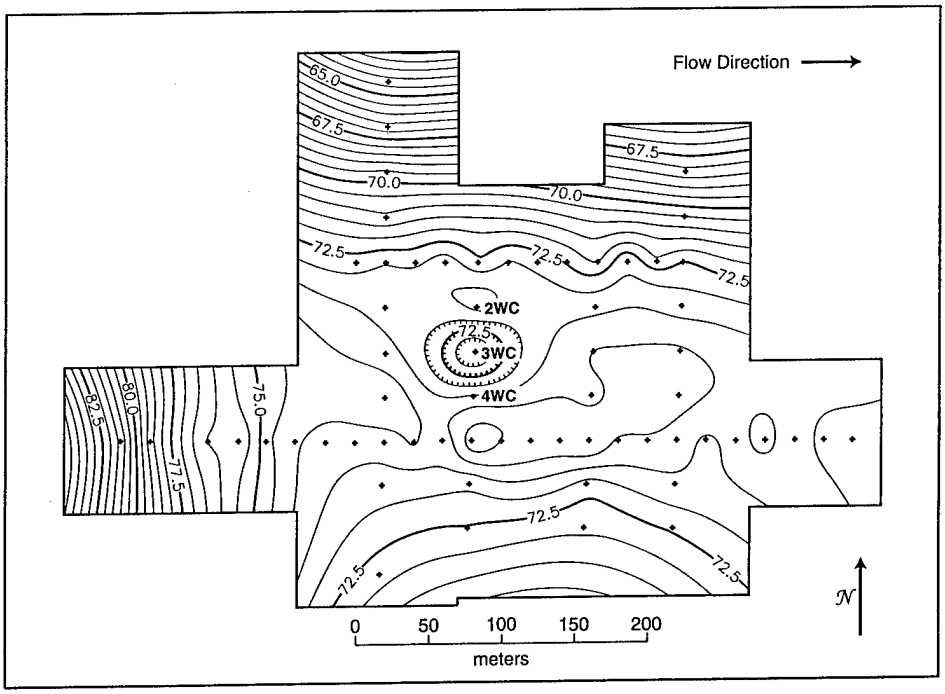

Figure 3. Map showing down-glacier component of the velocity field averaged over the entire study period. Crosses denote locations of survey stakes; 2WC, 3WC and 4WC are specific stakes. Stake velocities are interpolated to a 10- × 10-m grid; the grid is shown contoured at an interval of 0.5 m/yr. High gradients in velocity exist along the northern and western portions of the study reach.

Table 1. Displacement of 64 stakes.

Survey period	*Starting Julian day*	*Ending Julian day*	*Length (days)*	*Velocity† (m/yr)*	*Std. deviation*	*Std. error*
Stage I	149	162	13	79.8	2.46	0.31
Stage II	162	177	15	81.6	3.13	0.39
Stage III	177	188	11	71.8	2.64	0.33
Stage IV	188	216	28	66.3	2.3	0.29

*Day 150 = May 30.
†Average down-glacier component.

ern portion of Centerline, where they reach an excess of 80 m/yr. In this area, velocity contours are approximately perpendicular to Centerline and parallel to surface elevation contours. Velocity decreases from west to east along Centerline with a steep gradient of about –1.25 m/yr per 10 m. Slow velocities are found near the northern valley wall, where they are up to 25% less than near the center of the glacier. Velocity gradients in the northern portion of the study reach are roughly parallel with the valley wall and increase toward Centerline at a rate of approximately 0.80 m/yr per 10 m. Another gradient of decreasing velocity, although much weaker, extends from Centerline to the south at a rate of about 0.15 m/yr per 10 m. The central portion of the study reach has no regional gradients, but has several localized high value and low value areas. The most notable is an area of low velocity at stake 3WC. The velocity here is about 2 m/yr slower than the background of ~73.5 m/yr. The cause of this anomalously slow region is discussed in a later section.

Time variations

The four velocity stages, which range from 11–28 d in length (Table 1), show significant temporal variations. The average down-glacier velocity of the stakes is 80 m/yr at the start of the study period, reaches a peak of about 82 m/yr in early summer, and then slows to 66 m/yr by the end of summer (Fig. 4a). The average velocity of the study reach, thus, undergoes a change in magnitude of 20% during the summer months.

The standard deviation of the velocities of the 64 stakes is shown in Figure 4b. The standard deviation shows high variability in the velocity during the period of maximum average speed. As velocity decreases during the slowdown, the variability diminishes proportionally. However, the variability is anomalously low before the peak (Stage I) when compared to after the peak. The standard deviation suggests that there is higher variability in the velocity of stakes during the summer velocity peak and during the slowdown, and that variability is proportional to velocity both in magnitude and phase.

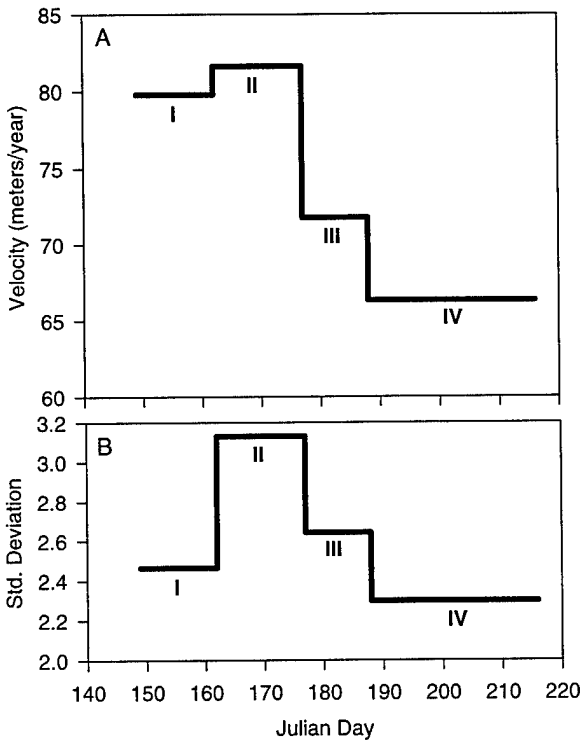

Figure 4. Down-glacier component of the velocity of 64 stakes. Roman numerals denote velocity stages. a. Average velocity during each of four stages. b. Standard deviation of velocity at each of the stages. Velocities and variability are greatest during Stage II; velocities and variability decrease proportionally during Stages III and IV.

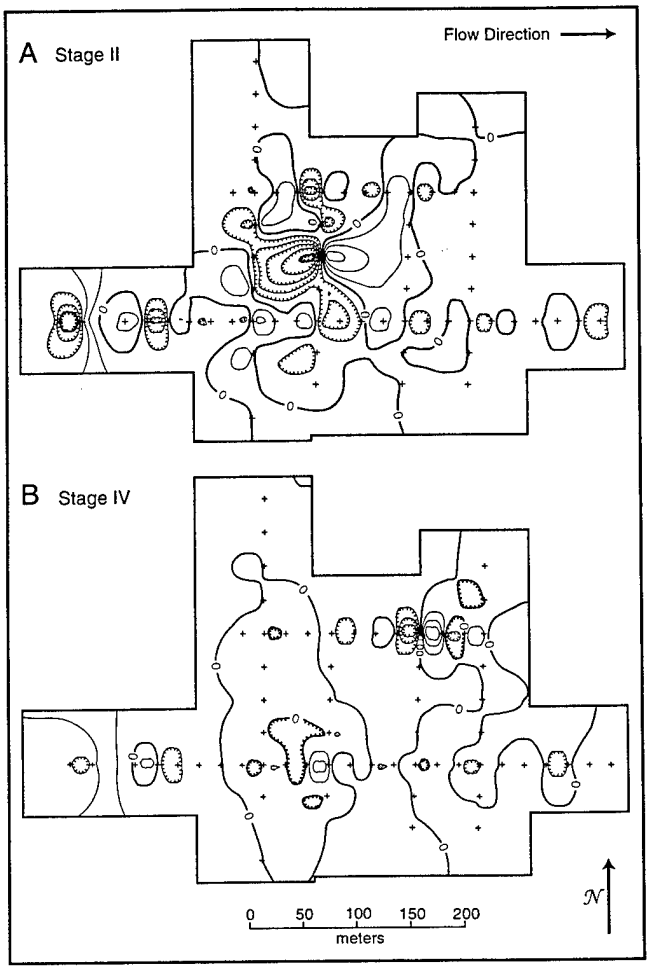

Figure 5. Maps showing longitudinal strain-rate during Stage II (a) and Stage IV (b). Crosses are locations of survey stakes. Strain-rates are calculated for a 10- ×10-m grid and are shown with a contour interval of 0.05 yr^{-1}; tick marks denote decreasing values. Locally high magnitude regions are more numerous during Stage II than during Stage IV.

Spatial variability in velocity can be examined in more detail by calculating the strain-rate field. In the case of the down-glacier component of velocity, u, the longitudinal strain rate is taken as u/x, where x is the down-glacier coordinate. Figure 5 shows the longitudinal strain-rate fields during Stage II and Stage IV. The strain-rate fields show multiple areas with closely spaced contours forming closed regions of ~10–40 m in diameter. The closed contours represent both locally positive (extensional) and negative (compressional) strain. These plots do not depict the true strain-rate field, but rather the strain-rate pattern measured by our particular spacing of measurement stakes. Details of the center and shape of positive and negative strain-rate regions may be an artifact of the contouring algorithm and are related to the location of initial data points. However, the plots clearly show that significant variability exists in the motion of stakes placed 20–30 m apart.

The longitudinal strain-rate is significantly more variable during the velocity maximum (Stage II) than during the slowest part of the study period (Stage IV). The strain-rate data show more numerous regions of closed contours during Stage II than Stage IV. The locations of the high and low value areas are not always constant between the two time periods. For example, the high strain-rate regions located along Westline during Stage II are totally absent in Stage IV. When the 25 stakes

spaced at 20 m along Centerline are considered, significant differences between the two stages are also observed. The magnitude of the strain-rate between these stakes averages 0.06 yr^{-1} during Stage II, while during Stage IV there is a reduction of 33%, giving an average of only 0.04 yr^{-1}.

DISCUSSION

Crevassing at the surface is the likely cause of the localized variability in velocity. The opening of a crevasse can cause a relative offset of stakes located on opposite sides of the crevasse, creating a velocity differential between the stakes. The magnitude of the offset depends on the proximity of the stakes to the crevasse, the total strain in ice near the crevasse, and width of the crevasse opening. During the study period, the glacier surface was covered by several meters of snow, making direct observations of crevasses difficult. However, an increasing number of crevasse traces were observed on the snow surface, beginning during Stage II and continuing through the remainder of the study period. The sound of crevasses opening was common during field work, with the intensity peaking toward the end of Stage II. Late summer observations of the bare-ice surface reveal that the glacier is heavily dissected by crevasses that are up to 150 cm in width. The crevasses are generally oriented across-glacier. Their opening would thus tend to cause variations in the down-glacier component of velocity.

The local velocity variability may be examined in more detail using stake 3WC. When averaged over the entire study period, stake 3WC has a velocity that is low relative to adjacent stakes (2WC and 4WC). However, the velocity of 3WC is only slightly lower during Stage I and Stage III, but is 10% slower during Stage II (Table 2). The velocity then reverts to the background average during Stage IV. This signal may be interpreted as the result of a crevasse opening just down-glacier of 3WC. The crevasse began opening during Stage I, experienced major failure and opening during Stage II, and stopped opening during Stage III. The opening of the crevasse caused the stake to move up-glacier relative to stakes 2WC and 4WC. The width of the crevasse can be calculated by comparing the absolute motion of Stake 3WC to the other stakes. During Stage II, the down-glacier displacement of stake 3WC was 3.02 m while 2WC and 4WC were displaced 3.37 and 3.35 m, respectively. A crevasse of ~35 cm width may have opened near 3WC. The crevasse opened at an average rate of 2 cm/day during the 15 day period—a reasonable rate. This is an upper limit for crevasse size as this is the only velocity anomaly present after averaging the measurements over the entire study period.

Table 2. 3WC velocities.

Survey period	*3WC velocity (m/yr)*	*% of 2WC*	*% of 4WC*
Stage I	79.19	98.9	98.0
Stage II	73.57	89.5	90.0
Stage III	69.19	98.5	97.8
Stage IV	67.72	100.5	101.1

Other work has shown the influence of crevassing on the surface flow field. By surveying stakes on Saskatchewan Glacier at 12-hour intervals, Meier (1960) found sudden large fluctuations in velocity, with stakes even appearing to move up-glacier. Most of these fluctuations were not synchronous among stakes, but instead seemed to affect blocks of not more than 100 m in horizontal dimension. Colbeck and Evans (1971) found extremely high local strain-rates associated with crevasses. When measured over the length scale of a few meters, they found that the strain field near opening crevasses has both compression and extension elements and reaches magnitudes as high as 0.08 yr^{-1}.

An alternative explanation for the local variability is survey errors. This explanation does not seem likely as the magnitude of the velocity variations are too great to be attributed to errors inherent in the measurement, and the surveying and data reduction methods caught or eliminated most common errors. Furthermore, errors arising from a one-time mislocation would lead to an anomalously low or high velocity during one stage to be followed by an anomalous velocity of the opposite sign during the next stage. This scenario is not observed.

CONCLUSIONS

Repeated measurements of surface velocity made with high spatial resolution give details about both the regional and local flow fields in a temperate valley glacier. The regional velocity field

shows gradients with velocity contours running parallel to a valley wall and perpendicular to an ice-fall. The steepness of these gradients is such that significant changes in velocity occur over the 10-m length scale. However, short term variations in velocity occur over this same length scale owing to surface crevassing. This localized variability is greatest during the summer velocity peak and scales with velocity following the peak. The similarity in length scales of variations in both the local and regional velocity fields leads to a problem: the regional velocity field can only be defined by smoothing in time or space, but smoothing removes important details about time-limited variations.

These findings suggest that considerable care should be taken in interpreting short time variations in the velocity of stake nets. Regional flow variations must be separable from localized transient events, such as surface crevassing, a difficult task over small time increments. The question of how the regional flow pattern in high-strain areas, such as near a large change in slope or an ice boundary, changes during short-term velocity variations thus remains open.

ACKNOWLEDGMENTS

This work was supported by grants from the National Science Foundation (OPP-9122966 to N. F. Humphrey; OPP-9122916 to W. T. Pfeffer). D. Bahr and B. Raup assisted with field work.

LITERATURE CITED

Anderson, S.P., J.I. Drever and N.F. Humphrey (in press) Glacial chemical weathering regimes in relation to the continental norm. In: *Proceedings of the Fourth International Symposium on the Geochemistry of the Earth's Surface, July 1996, Ilkley, England.*

Briggs, I.C. (1974) Machine contouring using minimum curvature. *Geophysics,* **39:** 39–48.

Brzozowski, J. and R.LeB. Hooke (1981) Seasonal variations in surface velocity of the lower part of StroglaciÑren, Kebnekaise, Sweden. *Geografiska Annaler,* **63A:** 233–240.

Colbeck, S.C. and R.J. Evans (1971) Small-scale strain measurements on a glacier surface. *Journal of Glaciology,* **10:** 237—243.

Harper, J.T. and N.F. Humphrey (1995) Borehole video analysis of a temperate glacier's englacial and subglacial structure: Implications for glacier flow models. *Geology,* **23:** 901–904.

Hodge, S.M. (1974) Variations in the sliding of a temperate glacier. *Journal of Glaciology,* **13:** 349–369.

Hooke, R.LeB., J. Brzozowski and C. Bronge (1983) Seasonal variations in surface velocity, StroglaciÑren, Sweden. *Geografiska Annaler,* **65A:** 263–277.

Hooke, R.LeB., P. Calla, P. Holmlund, M. Nilsson and A. Stroeven (1989) A 3 year record of seasonal variations in surface velocity, StorglaciÑren, Sweden. *Journal of Glaciology,* **35:** 235–247.

Iken, A. and R.A. Bindschadler (1986) Combined measurements of subglacial water pressure and surface velocity of Findelengletscher, Switzerland: Conclusions about drainage system and sliding mechanism. *Journal of Glaciology,* **32:** 101–119.

Kamb, B., H. Engelhardt, M. Fahnestock, N. Humphrey, M. Meier and D. Stone (1994) Mechanical and hydrologic basis for the rapid motion of a large tidewater glacier 2. Interpretation. *Journal of Geophysical Research,* **99:** 15,231–15,244.

Meier, M.F. (1960) Mode of flow of Saskatchewan Glacier, Alberta, Canada. U.S. Geological Survey Professional Paper 351, 70 p.

Meier, M., et al. (1994) Mechanical and hydrologic basis for the rapid motion of a large tidewater glacier 1. Observations: *Journal of Geophysical Research,* **99:** 15,219–15,229.

Paterson, W.S.B. (1994) *The Physics of Glaciers.* Oxford, United Kingdom: Pergamon Press, 480 p.

Pfeffer, W.T., N.F. Humphrey, D.B. Bahr, J.T. Harper, B. Raup and B. Welch (1994) Observed velocity structure at depth in Worthington Glacier, Alaska [abs.]. *Eos* (Transactions, American Geophysical Union), **75**: 222.

Raymond, C.F. (1971) Flow in a transverse section of Athabasca Glacier, Alberta, Canada. *Journal of Glaciology,* **10:** 55–84.

Stone, D.B., M.F. Meier, K.J. Lewis and J.T. Harper (1994) Drainage configuration and scales of variability in the subglacial water system [abs.]. *Eos* (Transactions, American Geophysical Union), **75**: 222.

Welch, B.C., W.T. Pfeffer, J.T. Harper and N.F. Humphrey (1996) A maximum resolution glacier bed surface obtained by radio-echo sounding. In Glaciers, Ice Sheets and Volcanoes: A Symposium Honoring Mark Meier. USA Cold Regions Research and Engineering Laboratory, Special Report 96-27.

On Energy Balance and Ablation of a Small Valley Glacier in Sweden

REGINE HOCK
Dept. of Geography, Swiss Federal Inst. of Technology,
Winterthurerstr. 190, CH-8057 Zurich, Switzerland
ph: +41-1-2575224
email: hock@geo.unmw.ethz.ch

BJÖRN HOLMGREN
Abisko Research Station, S-98107 Abisko, Sweden
ph: +46-980-40179

ABSTRACT

On Storglaciären, a small valley glacier in northern Sweden of 3 km^2, a comprehensive glaciometeorological experiment was conducted in both the second half of the 1970s and in the 1990s. A case study of heat-budget calculations for a 40-day period in summer 1994 is presented and discussed in detail in Hock and Holmgren (in press). The surface energy balance was calculated from hourly averaged measurements of air temperature, relative humidity, wind speed, net radiation and ice temperatures, which were obtained by a micrometeorological station close to the equilibrium line on the glacier ice. While net radiation was measured directly, the turbulent fluxes were estimated using the bulk aerodynamic method. Melt rates obtained as residuals in the heat balance equation were compiled to daily means and compared to measurements with ablatographs and ablation stakes in the vicinity of the meteorological station. On average, net radiation and the turbulent fluxes accounted for roughly two-thirds and one-third of the calculated energy balance, respectively. The heat flux in the ice was a minor heat sink owing to the existence of a cold surface layer on the glacier. The calculated melt energy was of similar magnitude to the measured melt energy on most of the days (Fig. 1). On average, 10% of measured melt was not accounted for by the model. On days characterized by dense fog or precipitation, though, the calculated melt energy considerably underestimated the actual values measured. These errors are mainly attributed to condensation under calm conditions, a process that may not be accounted for properly by the bulk aerodynamic approach. The energy balance proved to be very sensitive to the choices of aerodynamic surface roughness, and also to the relationship among the roughness lengths of wind, temperature and water vapor. Calculated melt energy changed considerably when using the widespread concept of similarity of roughness length, instead of a roughness length of wind that exceeds the one for temperature and vapor pressure by the order of two magnitudes. The latter relationship was derived from the profile measurements in the 1970s and used for the calculations. A stability correction for stable atmospheric conditions in terms of the Monin-Obukhov relations was considered inadequate, as the basic requirements for the theory are lacking in the glacier environment and which, in addition, deviated significantly from the wind profile structure found on the glacier.

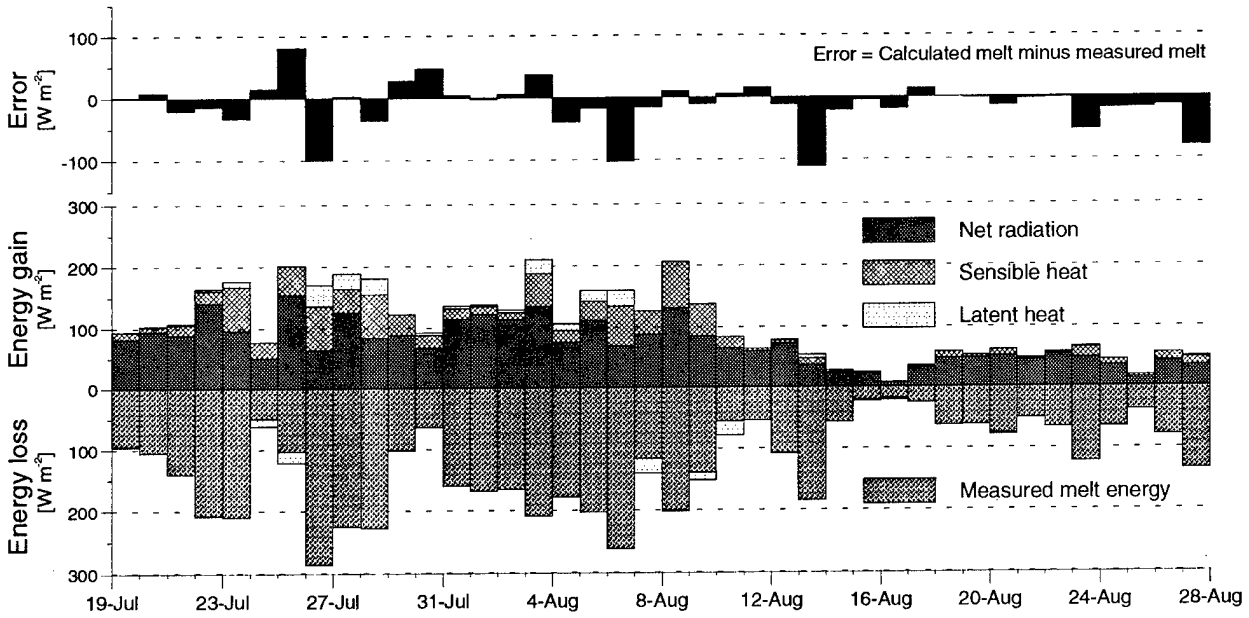

Figure 1. Energy balance terms given as flux densities close to the equilibrium line on Storglaciären from 19 to 27 July 1994. The error is defined as calculated minus measured melt flux densities. The ice heat flux is neglected.

LITERATURE CITED

Hock and Holmgren (in press) Some aspects of energy balance and ablation of Storglaciaren, northern Sweden. *Geografiska Annaler.*

Changes in the Configuration of Ice Stream Flow from the West Antarctic Ice Sheet

R.W. JACOBEL
Physics Department, St. Olaf College, Northfield, MN 55057

T.A. SCAMBOS
NSIDC, University of Colorado, Boulder, CO 80309

C.R. RAYMOND, A.M. GADES
Geophysics Program, University of Washington, Seattle, WA 98195

ABSTRACT

Ground-based radar studies have been carried out on Siple Dome, Antarctica, as a part of a collaboration among the University of Washington, St. Olaf College and the University of Colorado. The goals of this project are to use remote sensing imagery, ground surveys, and ice-penetrating radar (Fig. 1) to study the ice dynamics and history of the region as a part of the overall WAIS program. Radar profiles on the northeast flank of the dome show that a curvilinear scar, first seen in AVHRR imagery, is a dynamic boundary that defines the southwestern margin of a relict ice stream flowing from Ice Stream C to Ice Stream D, close to where it enters the Ross Ice Shelf. The scar is coincident with a trough and upward step in surface topography underlain by highly disturbed internal stratigraphy. Internal layers on the dome side of the boundary are undeformend, and can be traced to the summit where they have been dated, based on the 160-m core that has been drilled there. Northwest of the boundary, the internal layers are strongly folded and resemble more closely those seen in the active ice streams. Burial depth of the disturbed layers enables us to set a minimum shut-down time of this ice steam as having occurred prior to approximately 1.7 Ky BP. The configuration of the ice streams draining the West Antarctic Ice Sheet into the Ross Ice Shelf evidently changes with time, and attempts to predict the evolution of the WAIS must incorporate this observation.

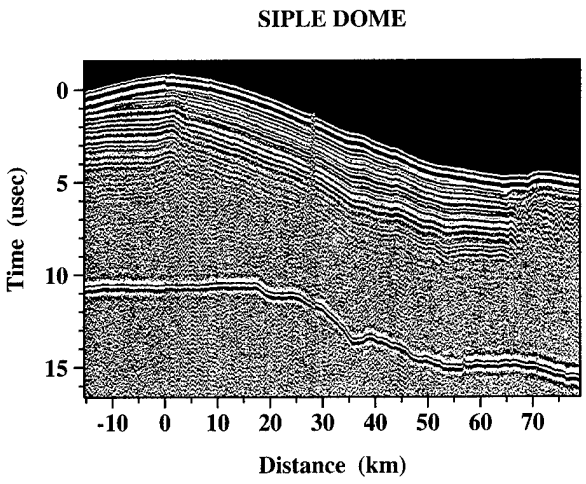

Figure 1. Radar profile from the summit of Siple Dome (~km 0) towards the northeast. The relict ice stream margin is crossed at approximately km 67, where continuous internal stratigraphy from the summit becomes disturbed, except for the uppermost layers.

On the Mass Balance of West Antarctica's Pine Island Glacier

S.S. JACOBS, A. JENKINS, H.H. HELLMER
Lamont-Doherty Earth Observatory
Palisades, NY 10964

INTRODUCTION

Perceptions of the total mass of the Antarctic Ice Sheet have changed much faster over recent decades than any conceivable climate-related changes, as Mark Meier has puckishly illustrated (Fig. 1). Adding a Drewry et al. (1982) value to that diagram continues the trend line, which admittedly, would be less steep if data prior to 1950 were ignored. It might also be inferred from the figure that credible advances have sought to stay within a few standard deviations of trends divined from the literature. In any event, a search for other evidence that might fit the Meier steady-growth principle led us to review the mass balance problem for Pine Island Glacier, a key element of the West Antarctic Ice Sheet (WAIS).

DISCUSSION

Pine Island Glacier (PIG) drains into the southeast corner of Pine Island Bay, a 30 × 40 km feature in the southeast Amundsen Sea. It was defined from 1946-47 aerial photographs and named for the *USS Pine Island*, a seaplane tender and flagship of the U.S. Navy Operation Highjump (Alberts 1995). The Bay lies at longitudes where early explorers in search of the southern continent were repulsed by the perennial sea ice. USGS surveyors worked on islands in the Bay in 1968, apparently supported by helicopter and LC-130 out of McMurdo Station (A. Lindsey, personal communication, 1996). The first ship in the Bay may have been the *USCGC Burton Island*, tasked in 1975 with evaluating this region's potential as a logistics support site for the U.S. Antarctic program (Seelig 1975). Pine Island Bay was bounded for years on its western side by the larger Thwaites Iceberg Tongue, since broken away but still prominent on some Antarctic maps.

In 1981, Hughes identified Pine Island Bay as the site of potential weakness in the WAIS, since it lacked a substantial ice shelf to retard retreat of its glacier grounding lines. The Bay may have been covered by an ice shelf until recent times, but by

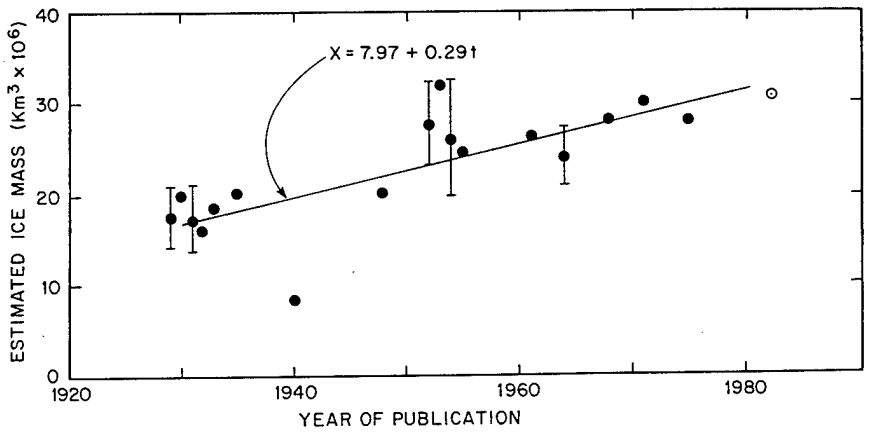

Figure 1. Temporal change in estimates of the total mass of the Antarctic Ice Sheet, modified from an unpublished diagram by M. Meier. The added open circle at the upper right is from Drewry et al. (1982).

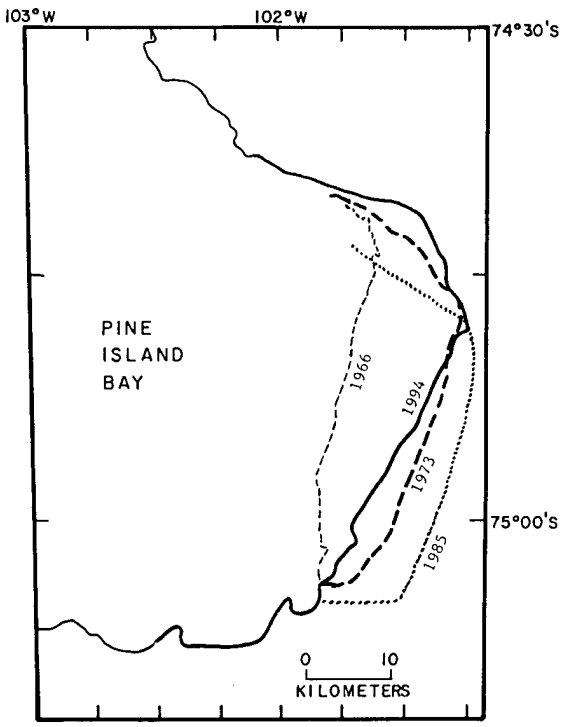

Figure 2. Temporal change in the position of the calving front of Pine Island Glacier, modified from Jenkins et al. (1994). The "1966" position is taken from a 1966 Antarctic Sketch Map, 1:500,000 scale, that also suggests prior calving of an ice front extending another 10 km seaward. The 1985 position is from Kellogg and Kellogg (1986). A calculated ice front velocity of 2.6 km/yr was based upon 1992 satellite imagery shown in Jenkins et al. (in press).

1985 the PIG calving front (Fig. 2) had been retreating at ~0.8 km/yr for at least the two prior decades (Kellogg and Kellogg 1988). Estimates of accumulation on its catchment basin and ice transport across its grounding line, however, led to the conclusion that the PIG had one of the more positive mass balances on the Antarctic Ice Sheet (Crabtree and Doake 1982, Lindstrom and Hughes 1984, Bentley and Giovinetto 1991).

More recently, ERS-1 SAR imagery has been used to determine the glacier's surface velocities, which increase rapidly across the grounding line to values of ~2.6 km/yr midway on the floating portion (Lucchitta et al. 1995). Their grounding line velocity of 1.9 km/yr, some three times higher than earlier estimates, implied that the catchment basin was much closer to equilibrium than previously believed. Similarly, measured changes in the calving front position over 10–15 month periods between successive SAR images indicated an advance rate of ~2.6 km/yr (Jenkins et al., in press). The forward movement since 1985 suggested an overall stability in the floating portion (Fig. 2), but radio echo soundings and freeboard height measurements revealed an ice flux across the grounding line roughly twice that across the calving front. If balanced by basal melting over an area corresponding to the 1994 PIG length, this implied a rate of 12 ± 3 m/yr (Jenkins et al., in press), much higher than the reported average for any other floating appendage of the WAIS.

The first ocean stations to the sea floor across the PIG calving front provided data consistent with a high melt rate. CTD (Conductivity-Temperature-Depth) profiles at three stations near the irregularly shaped PIG terminus (Fig. 3) revealed a 1080-m-deep trough, the bottom of which is filled with Circumpolar Deep Water (CDW). Slightly cooler and fresher than its source north of the continental shelf, CDW presumably extends into the sub-ice cavity at temperatures >3°C above the in-situ melting point. There, its buoyancy would increase as it melted basal ice, forming a plume of colder, lower-salinity water that would emerge at the ice front (Robin 1979, Kellogg and Kellogg 1988). At depths from about 100–800 m, thermohaline data from station 92 are consistent with the expected properties of a CDW/meltwater mixture (Nost and Foldvik 1994), and the Coriolis-deflected outflow is concentrated on the southern side of the cavity. Contrary to our initial perceptions (Jenkins et al. 1994), the cold and warm inversions on adjacent stations 93 and 94 appear to derive from the ambient shelf water and sub-ice outflows, respectively. Assuming geostrophic equilibrium and a salt balance between inflow and outflow on station 92 gave an average basal melt rate of 10–11 m/yr (Jacobs et al., in press).

A two-dimensional numerical model of the ocean thermohaline circulation beneath the PIG uses the CTD data to tune model parameters and cavity shape until outflow properties match those measured on station 92. For an 85-km-long PIG, this gives average melting of 9–12 m/yr, consistent with the ice and salt balance models. With local rates exceeding 20 m/yr, there is no evidence of basal freezing, and the average is more than 50 times that of the eastern Ross Ice Shelf (Hellmer and Jacobs 1995). Such high melt rates are caused by a combination of the "warm" CDW inflow and the great draft of PIG, which exceeds 1200 m near the grounding line (Crabtree and Doake 1982).

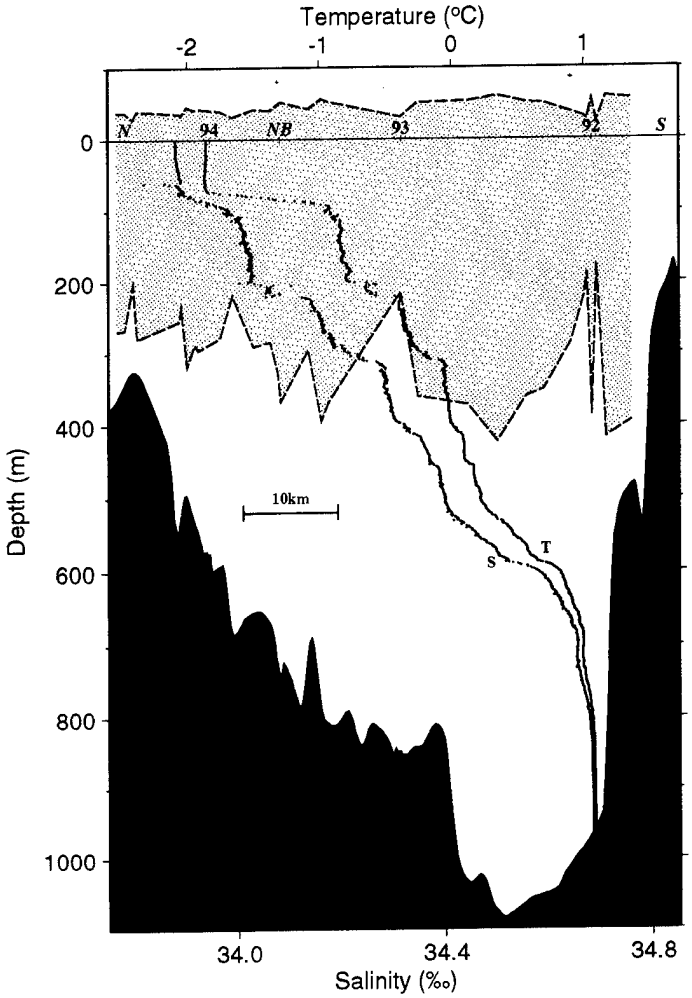

Figure 3. A north–south section occupied from the NB Palmer in March 1994 near the calving front of Pine Island Glacier in the southeast Amundsen Sea. The glacier thickness, calculated from freeboard heights (except +), averaged 410 m between station 92 and its northern boundary (NB). The superimposed station 92 salinity and temperature profiles and other related observations are discussed in more detail in Jacobs et al. (in press), and Jenkins et al. (in press).

These results confirm the Lucchitta et al. inference that the present-day PIG mass balance is close to zero. That balance is achieved by the ocean-driven melting, which, in combination with the calculated calving rate, requires high ice velocities to preserve the present glacier size. The findings extend observations near George VI Ice Shelf, which showed melting of approximately 2 m/yr and the shallow outflow of seawater well above the freezing point (Potter and Paren 1985). This melt-driven upwelling appears to be an important factor in the regional "ventilation" of CDW. In addition, Febuary–March 1994 ocean stations along the Amundsen and Bellingshausen continental shelf revealed that CDW floods most deep portions of this region. Higher basal melt rates than previously assumed must, therefore, be common throughout this sector. Applying this result to an earlier budget estimate increases the liklihood that the present-day mass balance of the Antarctic Ice Sheet is negative (Jacobs et al. 1992, in press).

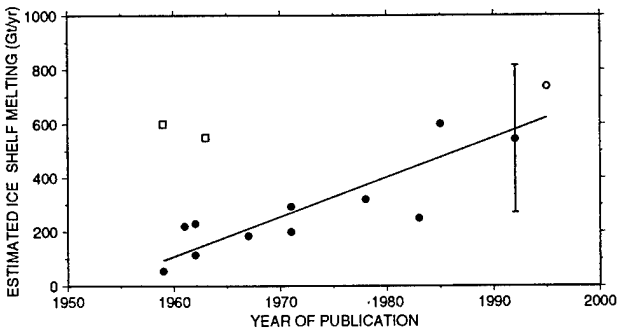

Figure 4. Temporal change in estimates of ice shelf melting, from data in Jacobs et al. (1992) and other sources. The open squares and some zero estimates were ignored in fitting the regression line; the open circle is from Jacobs et al. (in press) (1 Gt = 10^{12} kg).

SUMMARY

Meier (1993) pointed out that much more work is needed to understand the distribution of melting and freezing beneath the Antarctic ice shelves. He cited Oerter et al. (1992), who describe a thick layer of marine ice at the base of the Ronne Ice Shelf, as an example suggesting that basal freezing may be underestimated. The PIG provides an alternative example, illustrating that basal melting may be underestimated. Moreover, the history of estimates of the net mass balance at the base of Antarctic ice shelves shows a trend (Fig. 4) analogous to that of the total mass of the ice sheet in Figure 1. These are not data from which one can infer actual changes with time, much less predict the future evolution of these features. Nevertheless, it now appears that the ocean currently melts away a mass equivalent to approximately one-third of the recently increased annual accumulation (Giovinetto and Zwally, in press) on the Antarctic Ice Sheet.

LITERATURE CITED

Alberts, F.G. (1995) *Geographic Names of the Antarctic*, 2nd Ed. Washington, DC: National Science Foundation, 95-157, 834 p.

Bentley, C.R. and M.B. Giovinetto (1991) Mass balance of Antarctica and sea level change. In *International Conference on the Polar Regions in Global Change, Proceedings, 11–15 June 1990* (G. Weller et al., Eds.). University of Alaska, Fairbanks, p. 481–488.

Crabtree, R.D. and C.S.M. Doake (1982) Pine Island Glacier and its drainage basin: Results from radio echo-sounding. *Annals of Glaciology*, **3:** 65–70.

Drewry, D.J., S.R. Jordan and E. Jankowski (1982) Measured properties of the Antarctic ice sheet: Surface configuration, ice thickness, volume and bedrock characteristics. *Annals of Glaciology*, **3:** 83–91.

Giovinetto, M. and H.J. Zwally (in press) An assessment of the mass budgets of Antarctica and Greenland using accumulation derived from remotely sensed data in areas of dry snow. *Zeitschrift fur Gletscherkunde und Glazialgeologie*, **32.**

Hellmer, H.H. and S.S. Jacobs (1995) Seasonal circulation under the eastern Ross Ice Shelf, Antarctica. *Journal of Geophysical Research*, **100**(C6): 10,873–10,885.

Hughes, T.J. (1981) The weak underbelly of the West Antarctic Ice Sheet. *Journal of Glaciology*, **27**(97): 518–525.

Jacobs, S.S., H.H. Hellmer, C.S.M. Doake, A. Jenkins and R.M. Frolich (1992) Melting of ice shelves and the mass balance of Antarctica. *Journal of Glaciology*, **38**(130): 375–387.

Jacobs, S.S., A. Jenkins and H.H. Hellmer (in press) Antarctic Ice Sheet melting in the SE Pacific. *Geophys. Res. Lttrs.*

Jenkins, A., S.S. Jacobs and H.(J.R.) Keys (1994) Is this little PIG in hot water? *Ant. J. of the U.S.*, **29**(5): 121–122.

Jenkins, A., D.G. Vaughan, S.S. Jacobs, H.H. Hellmer and H.(J.R.) Keys (in press) Glaciological and oceanographic evidence for rapid melting

beneath Pine Island Glacier. Submitted to *Journal of Glaciology.*

Kellogg, T.B. and D.E. Kellogg (1986) Biotic provinces in modern Amundsen Sea sediments: Implications for glacial history. *Ant. J. of the U.S.*, **21**(5): 154–156.

Kellogg, T.B. and D.E. Kellogg (1988) Antarctic cryogenic sediments: Biotic and inorganic facies of ice shelf and marine-based ice sheet environments. *Paleo. Paleo. Paleo.*, **67:** 51–74.

Lindstrom, D. and T.J. Hughes (1984) Downdraw of the Pine Island Bay drainage basins of the West Antarctic Ice Sheet. *Ant. J. of the U.S.*, **19**(5): 56–58.

Lucchitta, B.K., C.E. Rosanova and K.F. Mullins (1995) Velocities of Pine Island Glacier, West Antarctica, from ERS-1 SAR images. *Annals of Glaciology*, **21:** 277–283.

Meier, M. (1993) Ice, climate and sea level: Do we know what is happening? In *Ice in the Climate System* (R. Peltier, Ed.). NATO ASI Ser., Vol. I 12. Berlin: Springer-Verlag, p. 141–160.

Nost, O.A. and A. Foldvik (1994) A model of ice-shelf-ocean interaction with application to the Filchner-Ronne and Ross Ice Shelves. *Journal of Geophysical Research*, **99**(C7): 14,243–14,254.

Oerter, H., J. Kipfstuhl, J. Determann, H. Miller, D. Wagenbach, A. Minikin and W. Graf (1992) Evidence for basal marine ice in the Filchner-Ronne Ice Shelf. *Nature*, **358:** 399–401.

Potter, J.R. and J.G Paren (1985) Interaction between ice shelf and ocean in George VI Sound, Antarctica. In *Oceanology of the Antarctic Continental Shelf*, Ant. Res. Ser., 43. Washington, DC: American Geophysical Union, p. 35–58.

Robin, G. (1979) Formation, flow and disintegration of ice shelves. *Journal of Glaciology*, **24**(90): 259–271.

Seelig, W.R. (1975) Pine Island Bay survey. *Ant. J. of the U.S.*, **10**(4): 193–194.

Shortwave Radiation Geometry and Glacier Distribution in the Cordillera Real, Bolivia

ANDREW G. KLEIN, JEFF G. MASEK, BRYAN L. ISACKS
Institute for the Study of the Continents, Department of Geological Sciences, Cornell University, Ithaca NY, 14853

ABSTRACT

Solar radiation is a primary energy source for ablation of the glaciers in the Cordillera Real of Bolivia (Francou et al. 1995). However, to date no studies have quantitatively examined the spatial variation of shortwave radiation in the region and its relationship to glacier locations. The direct and diffuse shortwave radiation fields were computed using a clear-sky radiation model for a small area in the Huayna Potosí region (16°17′S, 68°12′W) of the Cordillera Real, Bolivia. Hourly simulations of the shortwave components for the 21st day of each month show that glacierized areas receive significantly less shortwave radiation than non-glacierized areas at equivalent elevations during most months of the year. Annual average differences in total shortwave radiation incident upon glacierized and non-glacierized areas range between 2–4 MJ m^{-2} day^{-1}.

INTRODUCTION

Solar radiation provides a large percentage of the energy available for ablation on the high-elevation glaciers of the subtropical central Andes. Increased incident shortwave radiation attributable to decreased cloud cover during ENSO events contributes to the marked glacier retreat occurring in the region (Francou et al. 1995). The strong influence of radiation on glacial mass balance suggests that spatial variations in the net radiation field should influence where glaciers are located within the region and, potentially, glacier response to climatic forcings. However, the effect of orientation (aspect) on glacier Equilibrium Line Altitudes or ELAs in Bolivia has previously been examined only qualitatively (e.g., Jordan 1985). Glaciers with northeasterly aspects have been found to have the highest ELAs. This configuration was attributed to two effects: 1) at these low southern hemisphere latitudes, slopes with northern aspects receive more insolation than slopes with southern aspect, and 2) an afternoon buildup of clouds causes shading of slopes with a westerly aspects during the afternoon hours (Jordan 1985, Hastenrath 1991).

This study presents a quantitative analysis of the spatial distribution of shortwave radiation, testing the hypothesis that glacierized areas receive less solar insolation than non-glacierized areas. A Digital Elevation Model (DEM) was used to compute the direct and diffuse shortwave radiance incident on sloping surfaces under clear-sky conditions. Hourly simulations for the 21st day of each month were used to calculate seasonal and annual averages of incident shortwave radiation.

A small (15 × 17.5 km) region of the Cordillera Real was selected for this preliminary study (Fig. 1a). The site, centered at (16°17′S, 68°12′W), contains Cerro Huayna Potosí (6088 m), one of the higher massifs within the range, as well as numerous smaller peaks. Eighty-nine glaciers and perennial snow patches have been recognized within the study area. Glacierized areas were distin-

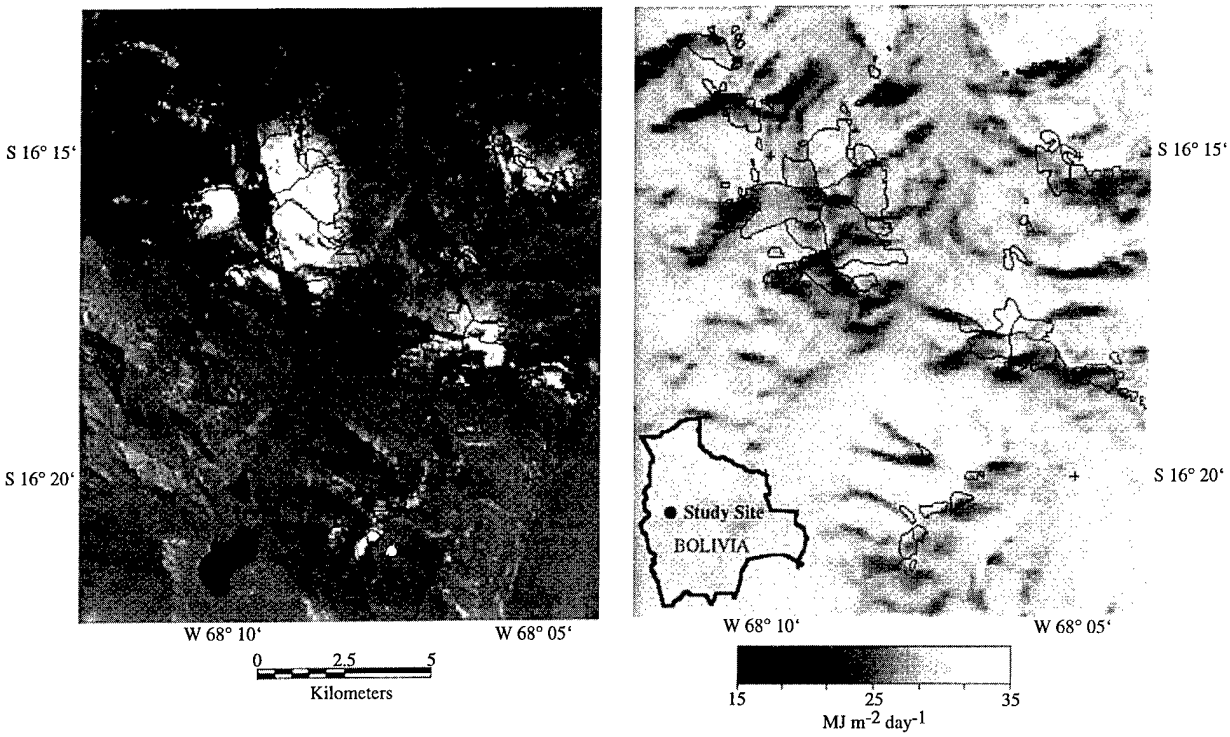

a. Landsat Thematic Mapper image (Band 4) of the numerous small glaciers in the area appear white in the image. Areas considered in the study are enclosed in black outlines and were taken from Jordan's (1991) glacial survey.

b. Greyscale image of average annual total (direct + diffuse) radiation received on each 100- × 100-m pixel in MJ m^{-2} day^{-1}.

Figure 1. Study area.

guished through digitization of 1:20,000 glacier maps produced by Jordan (1991).

SHORTWAVE TERRAIN MODELING AND METHODOLOGY

Mountainous terrain creates significant spatial variability in the incident shortwave radiation field. The total shortwave radiation incident upon a sloping surface is the sum of three components: direct, diffuse, and terrain reflectance. Direct radiation is a function of the elevation, slope, and aspect of each terrain facet, and whether the sun is obstructed from an individual terrain facet by surrounding topography. Diffuse radiation depends on the amount of the overlying sky visible to an individual slope facet. Terrain reflectance is neglected because of its relatively small magnitude and computational limitations to its calculation.

Topographically induced variations in shortwave radiation can be quantitatively modeled (e.g., Williams et al. 1972) using DEMs. The DEM for the study area was created from contours digitized from the 1:50,000 topographic maps produced by the Instituto Geografia Militar (IGM) in La Paz, Bolivia. The DEM, with 100-m resolution, was produced using a gridding algorithm developed by Hutchinson (1989) as implemented in the ARC/INFO Geographic Information System. The slope and aspect of each cell were calculated from the DEM by a planar least-squares fit to the nine adjacent elevation values within a 3 × 3 moving window.

Under clear-sky conditions the direct shortwave radiation (S_0) received on each terrain facet can be calculated as

$$S_0 = I \eta \Phi T_r T_w \quad (1)$$

(Munro and Young 1982) where I is the solar constant (1353 W m^{-2}), η is a binary shade factor (0 if the pixel is shadowed, 1 if not), Φ is the local illumination factor that corrects for topographic ori-

entation, and T_r and T_w are atmospheric transmissivities accounting for Rayleigh scattering and water vapor absorption, respectively. The local illumination factor is calculated by

$$\Phi = \cos(Z)\cos(\beta) + \sin(Z)\sin(\beta)\cos(\gamma_s - \gamma) \quad (2)$$

where Z is the solar zenith angle, β is the local topographic slope, γ is the local topographic aspect, and γ_s is the solar azimuth. The binary shade factor (η) utilizes the Dozier and Frew (1990) algorithm for rapid determination of local horizons.

The diffuse radiation (D_0) is calculated as

$$D_0 = I\cos(Z)\,T_d\,V\,. \quad (3)$$

The sky-view factor (V) is the fraction of the hemispheric sky dome visible from the given pixel (Dozier and Frew 1990). It is calculated from the DEM by calculating the horizon angle from each point on the topography in eight directions (45° increments) and averaging.

The atmospheric transmissivities (T_r and T_w) are functions of atmospheric path length and hence decrease with increasing zenith angle and decreasing elevation. Expressions for T_r and T_w are taken from Coulson (1975) and Gruell and Oelermans (1986). T_d is the diffuse atmospheric transmissivity given by (Munro and Young 1982) as

$$T_d = \{0.5\,(1 - T_r)\} + \{0.8\,(1.0 - T_z)\,(T_r * T_w)\} \quad (4)$$

where T_z represents atmospheric dust transmissivity, fixed in this study at 0.95. The values of 0.5 and 0.8 represent forward scattering ratios for Rayleigh and Mie scattering, respectively (Munro and Young 1982).

RESULTS AND CONCLUSIONS

Shortwave radiation geometry is found to be an important factor controlling the location of glaciers in the eastern Andes of Bolivia. Under clear-sky conditions, glaciers in the Huayna Potosí region are found preferentially in topographic positions receiving less incident solar radiation than non-glacierized areas. On an annual basis, mean differences in total (direct + diffuse) radiation received on glacierized and non-glacierized areas at the same elevation range between 2–4 MJ m^{-2} day^{-1}. These differences represent between 5 and 25% of the total radiation incident on glacierized slopes.

Despite the low latitude of the study site, the magnitude and the spatial patterns of incident shortwave radiation vary considerably from month to month. Incident net radiation averaged by elevation (Fig. 2) varies from 12 MJ m^{-2} day^{-1} during the austral winter months to over 35 MJ m^{-2} day^{-1} during austral summer months. Monthly mean differences in incident shortwave radiation between glacierized and non-glacierized areas also vary considerably throughout the year (Fig. 3). Maximum differences, up to 9 MJ m^{-2} day^{-1}, occur during the austral winter when absolute incident shortwave radiation is also low. Minimum differences are found during austral summer, when incident shortwave radiation is high in all landscape positions. From March to

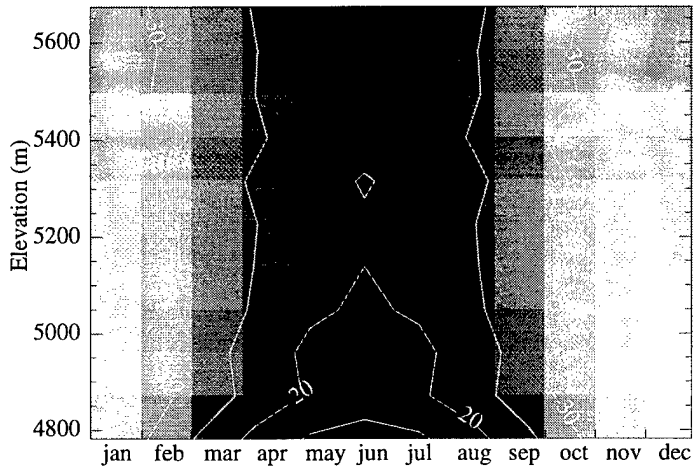

Figure 2. Average shortwave (direct + diffuse) insolation received on glacierized areas as a function of elevation for each month of the year. Each cell in the graph represents the mean monthly shortwave radiation for a 90-m vertical interval. The contours indicate values of the incident radiation in MJ m^{-2} day^{-1}.

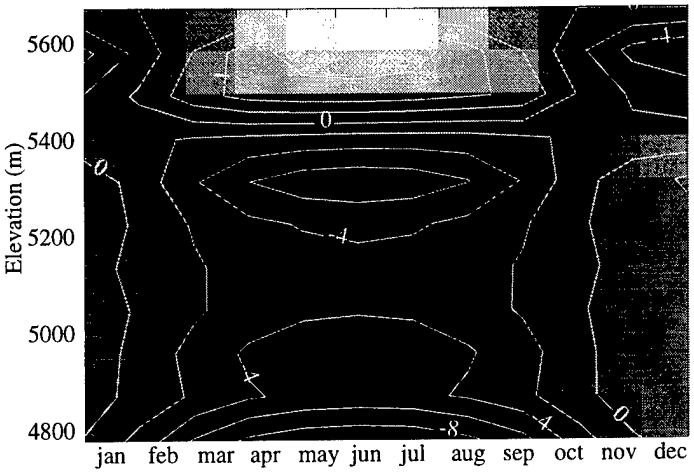

Figure 3. Mean monthly differences in total shortwave radiation between glacierized and non-glacierized areas as a function of elevation. Each cell represents the shortwave radiation difference for each month for the same 90-m vertical interval shown in Figure 2. Differences are negative where glacierized areas receive less incident radiation. Contours indicate values of the incident radiation in MJ m^{-2} day^{-1}.

September, glacierized areas receive 10 to 50% less shortwave radiation than non-glacierized areas at equivalent elevation.

The occurrence of only negligible differences between incident solar radiation received on glacierized and non-glacierized slopes during the height of austral summer would seem to weaken the contention that spatial variations in the net shortwave field control glacier distribution. However, during austral summer little overall variation occurs in the shortwave field, so it is not surprising that model results show only negligible differences in shortwave radiation received on glacierized and non-glacierized slopes. Increased cloudiness during this period also makes the clear-sky model less representative of actual conditions than during the rest of the year. Most importantly, the early and late periods of the wet season (October–December and March–May) are the critical times for determining the annual mass balance of region's glaciers, especially during ENSO years (Francou et al. 1995). Significant differences in incident shortwave radiation exist between glacierized and non-glacierized regions during most of these months, especially during March-May (Fig. 3).

In addition to differences in the direct component, significant differences in incident diffuse radiation occur between glacierized and non-glacierized areas. Under the assumption that diffuse radiation geometry is an adequate proxy for overcast skies, then, under these conditions, glacierized areas also receive less solar radiation than non-glacierized areas. This arises because glaciers tend to be located in topographic locations that "see" a smaller portion of the overlying hemisphere.

The dominant southerly aspect of the majority of region's glaciers is the major reason glacierized areas receive less solar radiation than adjacent non-glacierized areas. On average, south facing slopes receive less annual shortwave radiation than northern slopes. Southerly slopes also exhibit higher variability in the magnitude of incident shortwave radiation for a given aspect. This is ascribable to greater slope dependence of the direct component for locations facing away from the sun.

Considerable variation exists in the amount of average annual shortwave radiation incident upon individual glaciers. Differences in the average incident radiation received on the studied glaciers can be as large as 14 MJ m^{-2} day^{-1}. Such differences could conceivably lead to varying glacier response to a climatic forcing. While this clear-sky modeling indicates that radiation geometry influences the position of glaciers and creates large differences in the incident shortwave energy received on individual glaciers, inclusion of cloud cover in

the model remains paramount to fully understanding the relationship between incident shortwave radiation and glaciers in the region.

ACKNOWLEDGMENTS

This work is supported by NASA Mission to Planet Earth/Earth Observing System grant NAGW-2638. The first author is also supported by a DOE Graduate Fellowship for Global Change. The authors wish to thank Pierre Ribstein and Bernard Francou of ORSTOM/La Paz and Sophie Moreau of ABTEMA for their kind support. Thanks also to Christopher Duncan, Cornell University, for his indispensable software libraries. INSTOC contribution 224.

LITERATURE CITED

Coulson, K.L. (1975) *Solar and Terrestrial Radiation.* New York: Academic Press, 322 p.

Dozier, J. and J. Frew (1990) Rapid calculation of terrain parameters for radiation modeling from digital elevation data. *IEEE Transactions on Geoscience and Remote Sensing,* **28**(5): 963–969.

Francou, B., P. Ribstein, R. Saravia and E. Tiriau (1995) Monthly balance and water discharge of an inter-tropical glacier: Zongo Glacier, Cordillera Real, Bolivia 16° S. *Journal of Glaciology,* **41**(137): 61–67.

Gruell, W. and J. Oerlemans (1986) Sensitivity studies with a mass balance model including temperature profile calculations inside the glacier. *Zeitschrift für Gletscherkunde und Glazialgeologie,* **22**(2): 101–124.

Hastenrath, S. (1991) *Climate Dynamics of the Tropics.* Dordrecht: Kluwer Academic Publishers, 488 p.

Hutchinson, M.F. (1989) A new procedure for gridding elevation and stream line data with automatic removal of spurious pits. *Journal of Hydrology,* **106:** 211–232.

Jordan, E. (1985) Recent glacier distribution and present climate in the central Andes of South America. *Zeitschrift für Gletscherkunde und Glazialgeologie,* **21:** 213–224.

Jordan, E. (1991) *Die Gletschcer der Bolivianischen Andean.* Stutgart: Franz Steiner Verlag, 365 p.

Munro, G.J. and D.S. Young (1982) An operational net shortwave radiation model for glacier basins. *Water Resources Research,* **18**(2): 220–230.

Williams, L.D., R.G. Barry and J.T. Andrews (1972) Application of computed global radiation for areas of high relief. *Journal of Applied Meteorology,* **11:** 526–533.

Glacier Mass Balance Using the Grid-Index Method

ROBERT M. KRIMMEL
U. S. Geological Survey, Ice and Climate Project, Tacoma, WA

ABSTRACT

Mass balance is often measured at specific points on glaciers. Many methods have been devised to convert balance measured at points to a glacier-averaged value. Ideally, a sufficient number of balance points is measured so that isopleths of balance can be drawn over the entire glacier, and balance volumes are determined from the isopleths. In practice, the low density of measurements often does not allow accurate isopleth maps to be drawn.

The Grid-Index (GI) method requires a Digital Elevation Model (DEM) of the glacier and an Elevation-Balance Function (EBF). Numerous points along a hand-drawn curve of point measurements become the EBF. Linear interpolation is then used to determine the balance at the elevation of all grid locations of the DEM, an average of which is the average glacier balance. The GI method has been used to calculate winter and net balances at South Cascade Glacier, for the years 1986–91, and results deviate as much as 0.6 m from the single point index method of balance averaging previously used.

INTRODUCTION

Long-term glacier mass balance data sets typically consist of a differing number of measurements from year to year because of changes in funding levels, personnel, technology, logistics, and weather. For example, at South Cascade Glacier in Washington State, the density of net balance measurements varies from 0.3 to 10 points per square kilometer for the 1958–94 measurement period. Detailed balance maps can be drawn with confidence with a measurement density of 10/km^2, but not with a density of less than about 3/km^2. Thus, not only does the density of measurements change, depending on external forces, but the methods by which the balance is calculated also change. The purpose of this paper is two-fold. First, a method that uses all available balance data regardless of measurement density is proposed. Second, that method is applied to South Cascade Glacier data for 1986–91, years for which balance values had previously only been estimated by using a single-point index method (Krimmel 1989).

All evaluations of total glacier balance require some method of using balance results obtained at specific locations on a glacier to represent the surrounding area. When sufficient data density exists, a map of equal balance contours may be created from the collection of represented areas, from which total glacier balance is determined (Ostrem and Brugman 1991). When the density of measurements is too low to make a balance map, a different method of balance evaluation must be devised.

Balance maps were created at South Cascade Glacier for years 1965–82, examples of which can be found in Meier et al. (1971). A balance measurement was always made near the lateral center of the glacier at about 1840 m elevation (P1 on Fig. 1). The 1965–82 record of net balance at P1 is plotted against the glacier net balance (as determined from the balance maps) in Figure 2. Glacier net balance may subsequently be determined using the relation between the P1 balance and map-determined balance from subsequent P1 measurements alone. Values of winter and net balance for South Cascade Glacier have been published for every year during 1958–91 using either the mapping method or the single point (P1) indexing method (Krimmel 1995). The single point indexing method does not compensate for changes in glacier geometry, nor does it incorporate data points at locations other than P1. The grid-index

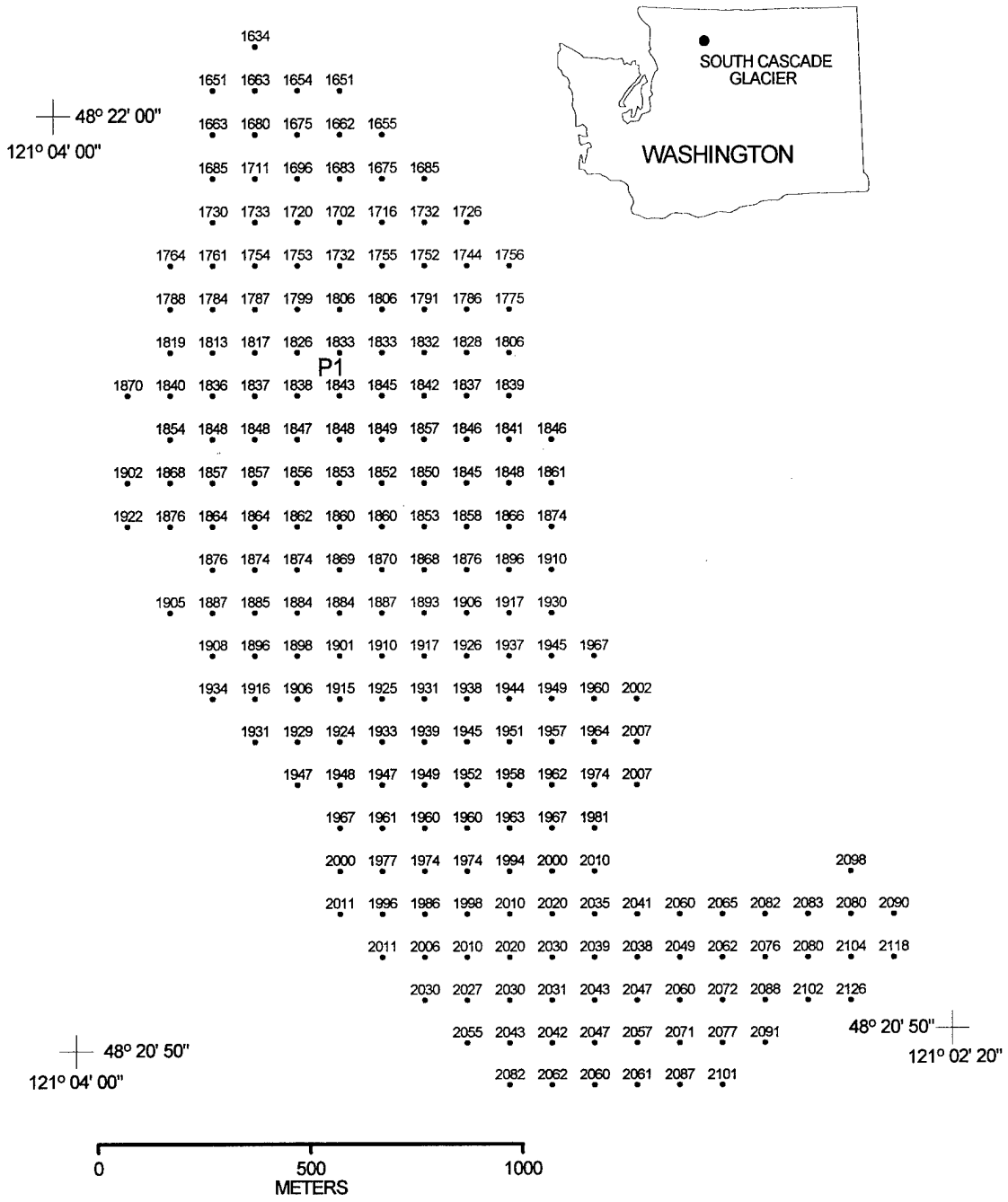

Figure 1. South Cascade Glacier, Washington. The numbers are elevations, in meters, of the digital elevation model for 1991.

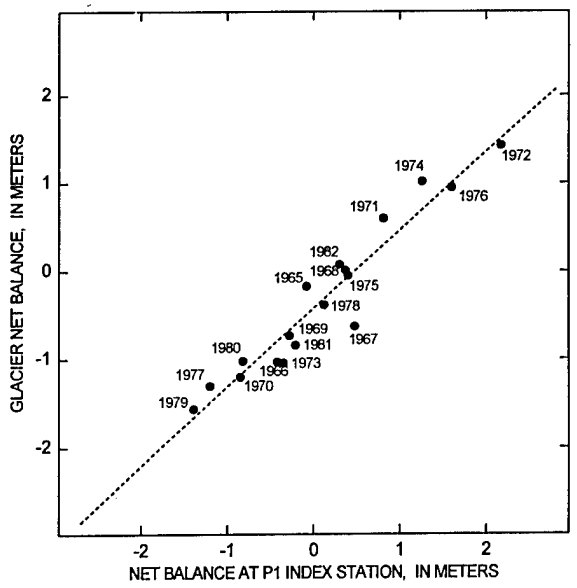

Figure 2. Relation between South Cascade Glacier net balance and P1 net balance.

(GI) method was devised so that all measurements could be used, rather than relying on the single measurement at P1, yet would not require that a balance map be drawn when the measurement density was too low for a valid map.

GRID-INDEX METHOD

A Digital Elevation Model (DEM) and an Elevation Balance Function (EBF) are essential to the grid-index method. The DEM is a regularly spaced grid of surface elevations. At South Cascade Glacier, a grid resolution of 100 m is used, resulting in about 200 grid points (Fig. 1). The elevation values of the DEM can be extracted from a topographic map or directly taken from a stereo model of aerial photographs or high resolution satellite images. The DEM should represent the glacier surface approximately concurrently with the balance year. For South Cascade Glacier, a DEM is created every year because of the rapidly changing terminus position and surface elevation.

The EBF is a function that describes the change in mass balance with change in surface elevation of the glacier that can be made at any time, but is normally produced for measurements near the accumulation maximum (winter balance) and the glacier minimum mass (net balance). An elevation function of other variables can be formed, and might be useful in forming the EBF. For instance, snow depth is easily measured with a probe rod, and is routinely measured at South Cascade Glacier near the time of maximum accumulation. Each probe location is recorded on a field map and an elevation for the probe is determined from the DEM. A pocket altimeter can also be used to determine the elevation, and satellite global positioning can be used to locate the probe. An elevation function of snow depth can be converted to an EBF by applying a snow density factor, which might also be an elevation function. Figure 3 shows elevation functions of snow depths for the years 1986–91, which subsequently are converted to EBFs. Figure 4 shows the EBFs of net balances for the years 1986–91.

The distribution of data points on the EBF plot rarely indicates a simple relation between balance and elevation because of naturally occurring variations of balance at any elevation. On most glaciers, local topography influences accumulation and ablation resulting in these lateral variations. A hand-drawn line approximating an average curve through all the data points, and extrapolated to elevations above and below the data points to include the entire elevation span of the DEM, becomes the EBF (Fig. 4). The final requirement of the EBF is that it be numerically calculable at all DEM elevations. A table of specific balance–elevation values can be extracted from the EBF, and linear interpolation on the segmented hand-drawn curve determines the balance at all elevations.

Calculation of the total balance requires summation of the calculated balance volumes at each element of the DEM. The average of all DEM balance values is the average balance.

RESULTS

The GI method was applied to measurements made at South Cascade Glacier for the balance years 1986–91. An elevation function was developed for the maximum snow accumulation and net balance for each year. Each maximum accumulation function is based on all the available measurements, which are usually numerous snow depth probes, and one or two measurements of snow density. For the years 1989–91, the elevation span of the DEM is fairly well covered with numerous snow depth measurements. In 1987, the elevation span is good, but because there are only eight data points there is little information about possible lateral variations of balance. In 1986 and 1988, the accumulation function was determined

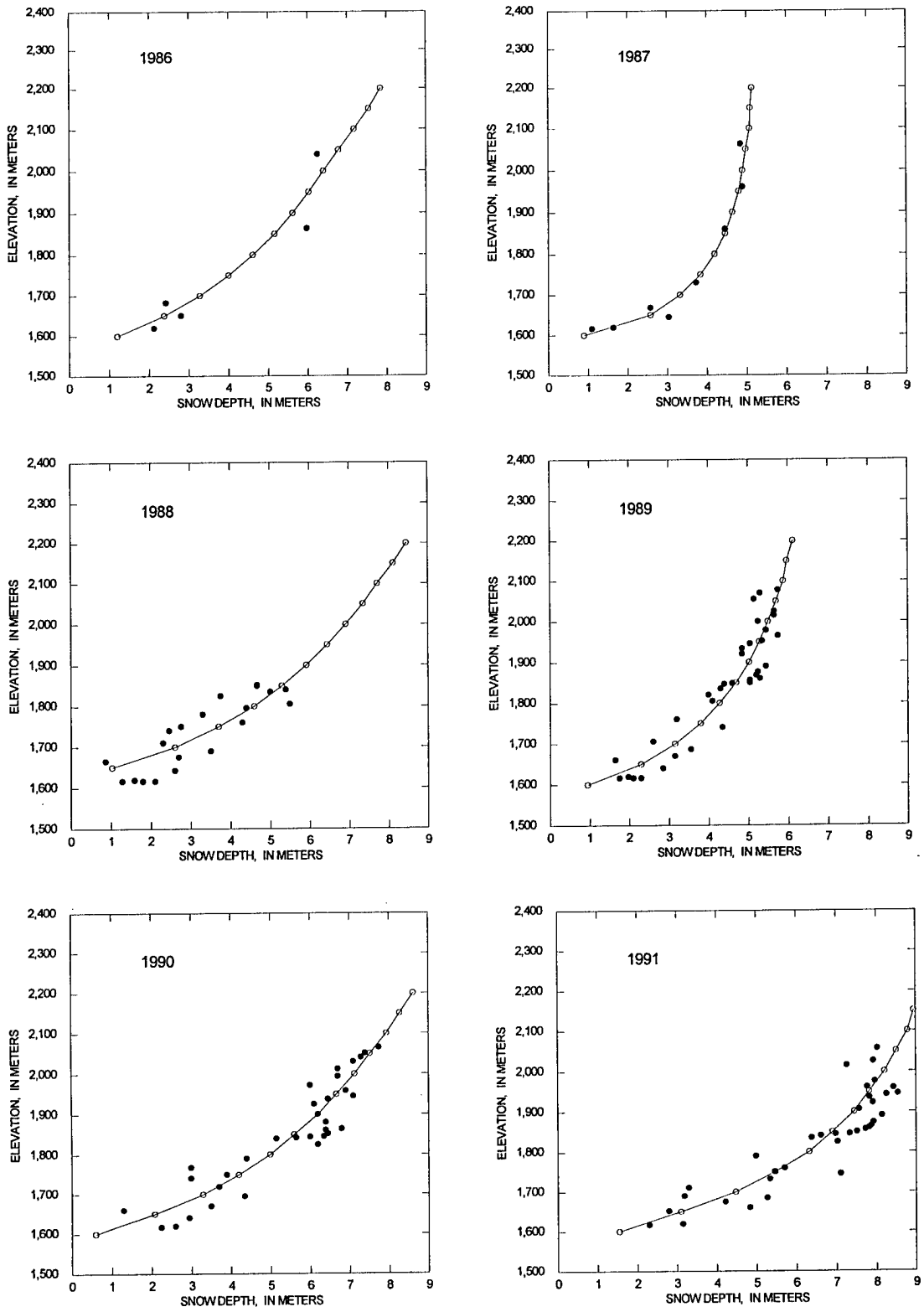

Figure 3. Elevation snow-depth function at South Cascade Glacier for 1986–91. Solid dots are measured snow depths, the line is a hand drawn estimate of the trend of the measured depths, and circles are points along the hand drawn line used for interpolation.

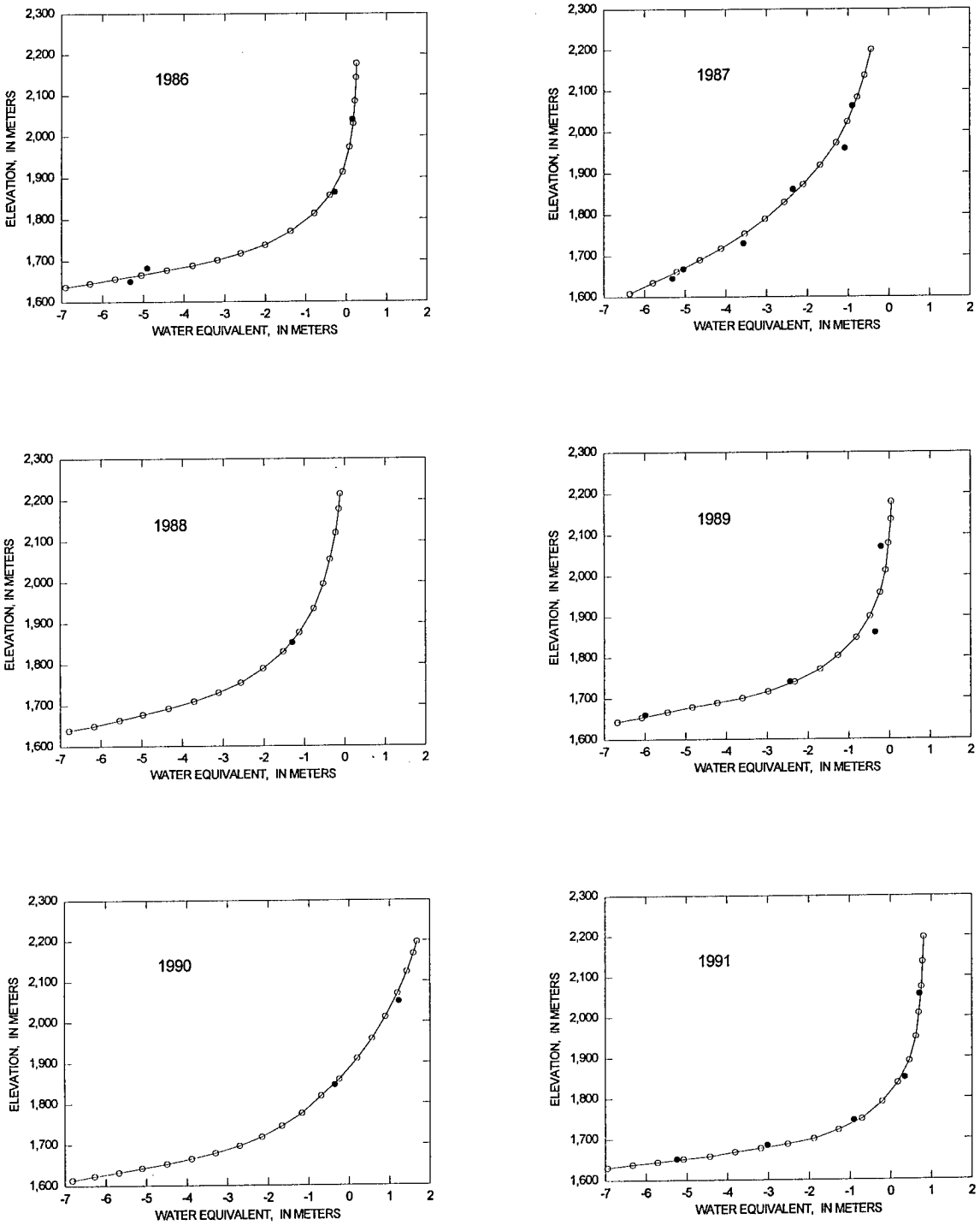

Figure 4. Elevation net-balance function at South Cascade Glacier for 1986–91. Solid dots are measured net balance, the line is a hand drawn estimate of the trend of the measured net balance, and circles are points along the hand drawn line used for interpolation.

Table 1. Net and winter balance values calculated by the Grid-Index method and the P1 single point method.

Year	Number of cells	GI Net (m)	P1 Net (m)	GI Winter (m)	P1 Winter (m)
1986	231	–0.61	–0.71	2.45	2.43
1987	224	–2.06	–2.56	2.04	1.88
1988	219	–1.34	–1.64	2.44	1.89
1989	219	–0.91	–0.71	2.43	2.35
1990	218	–0.11	–0.73	2.60	2.80
1991	218	0.07	–0.20	3.54	3.35

Definitions:
Year = The calendar year in which the net and winter balance occurred.
Number of cells = Each cell is 100 × 100 m.
GI Net = Net balance calculated using the GI method.
P1 Net = Net balance calculated using the P1 index method.
GI Winter = Winter balance calculated using the GI method.
P1 Winter = Winter balance calculated using the P1 index method.

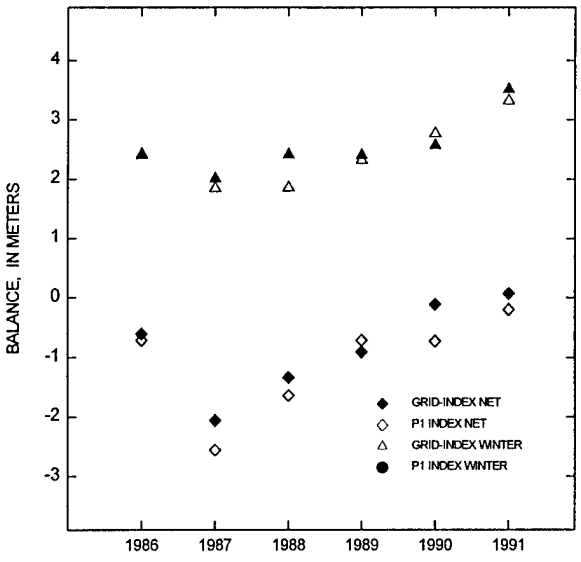

Figure 5. Comparison of grid-index method results and P1 index station results for mass balance evaluations.

from a dearth of data and by assuming that the shape of the function was similar to other years.

Fewer measurements are available for the EBFs of net balance than for winter accumulation because it is more difficult to measure the material that has disappeared during the ablation season than it is to measure the snow of the accumulation season. At South Cascade Glacier, stakes are set into the firn or ice prior the onset of ablation, and the total seasonal firn or ice loss is measured at each of the stakes. If stakes are not placed deeply enough into the ice, and if they are not reset during the ablation season, direct measure of the total seasonal ablation is irrecoverably lost. For the years 1986, 1987, 1989, and 1991, measurements spanned the elevation of the DEM well. For years 1988 and 1990, the shape of the EBF is assumed to be similar to that of the years for which there are more data. For each year, it is assumed that the measurements are located so that no strong bias is created because of lateral balance variation.

Results using the GI method are compared with results from the P1 indexing method in Table 1 and Figure 5. Results deviate as much as 0.6 m from the single point index method of balance averaging previously used.

Errors are difficult to assign to mass balance measurements. In Meier et al. (1971), errors in the balance values determined from balance maps were estimated at 0.1 m for net balance and 0.2 m for winter balance. Error in the P1 indexing method, which relies on a single measurement point, is much larger, and estimated at 0.5 m for both the net and winter balance values. Error using the GI method would logically fall between those of the mapping and P1 indexing methods, or 0.2 or 0.3 m for both the net and winter balance. The error will also depend on the degree to which the EBF elevation span was covered with actual measurements; for instance, the 1988 net balance results rely heavily on the assumption of a curve shape.

The GI method uses all balance measurements, and after the shapes of the required EBFs are determined, is independent of the density of measurements. Furthermore, lateral variations of balance are included to the extent that measurements record these variations, and changes in glacier size and elevation distribution are accounted for as the DEM is adjusted to the true glacier configuration.

LITERATURE CITED

Krimmel, R.M. (1989) Mass balance and volume of South Cascade Glacier, Washington 1958–1985. *Glacier Fluctuations and Climatic Change.* Kluver Academic Publishers, Dordrecht etc., p. 193–206.

Krimmel, R.M. (1995) Water, ice, and meteorological measurements at South Cascade Glacier, Washington, 1994 balance year. U.S. Geological Survey

Water-Resources Investigations Report 95-4162.
Meier, M.F., W.V. Tangborn, L.R. Mayo and A. Post (1971) Combined ice and water balances of Gulkana and Wolverine Glaciers, Alaska, and South Cascade Glacier, Washington, 1965 and 1966 hydrologic years. U.S. Geological Survey Professional Paper 715-A.
Ostrem, G. and M. Brugman (1991) Glacier mass-balance measurements. Saskatoon: NHRI Science Report No. 4, p. 71–74.

Changing Mode of Ice Flow During Advances of Hintereisferner

M. H. KUHN, N. SPAN
Institute of Meteorology and Geophysics, Innrain 52, A-6020 Innsbruck, Austria, +43-512-507-5450, meteorologie@uibk.ac.at

H. SCHNEIDER
Institute of Mathematics, Technikerstr. 24, A-6020 Innsbruck, Austria

ABSTRACT

Since the beginning of surveys of the ice flow velocity of Hintereisferner in 1894, this glacier has experienced three phases of anomalously high speed, peaking in an actual advance in 1919 and leading to slowdowns of the terminus retreat in 1939 and 1980. Velocity maxima were up to eight times those of the quiescent phase, and they built up and decayed in as little as 6 years.

The velocities of these events cannot be explained by increased thickness and basal stress alone, but also must be attributable to increased basal sliding. Unlike in kinematic waves, the ice was accelerating almost instantaneously in the lower accumulation area and in most of the ablation zone. Thickness profiles along the central flow line show thinning above the equilibrium line and bulging of the tongue.

The three accelerated phases were preceded by exceptional winter precipitation and cool summers. In general, peak flow velocities followed peak specific mass balances with 1 or 2 years delay.

INTRODUCTION

Hintereisferner is a temperate valley glacier in the Tyrolean Alps (46°48'N, 10°46'E) of about 10-km^2 area that currently extends between 2500- and 3700-m elevation over a length of 7.5 km (Fig. 1). It has been thoroughly investigated and mapped since the end of the 19th century (Blümcke and Hess 1899), velocity having been surveyed since 1894 and mass balance since 1952 (Schimpp 1960, Hoinkes 1970, Kuhn 1981, Span 1993). Central flow line models have been applied to Hintereisferner by Greuell (1992) and Schlosser (1996).

This 100 years of record comprises three periods of accelerated flow that led to an actual advance from 1918 to 1922 and to peak velocities in 1943 and 1978. Compared to the quiescent phase, velocity increased by up to eight times. In the following, we will present selected data to highlight these events, point out the climatic conditions preceding them and speculate about the changes in the flow regime that were associated with them.

VELOCITY DATA

Blümcke and Hess installed a stake network that covered the tongue and the lower accumulation area up to an altitude of about 3000 m (at 2.5 km in Fig. 1). During and immediately after World War I, only the lower part up to 2700 m (at 7.0 km) was surveyed annually. The average velocity of a group of stakes between 8.1 and 9 km is shown in Figure 2 for the period 1895 to 1932. During that time, the ice thickness decreased considerably (cf. Fig. 1) so that a general decrease of surface velocity is not surprising.

In 1914 and subsequent years, surface velocity started picking up at an increasing rate until it reached 125 m/a in 1919, decaying again to less than 20 m/a in 1923. The filled and open squares in Figure 2 are at 8.1 and 8.2 km and the open circle and crosses at 8.9 and 9.1 km, respectively. Ice thickness was about 180 m at 8.1 km and nearly zero at 9.1 km. From 1918 to 1922, the front of Hintereisferner advanced by an average of 60 m.

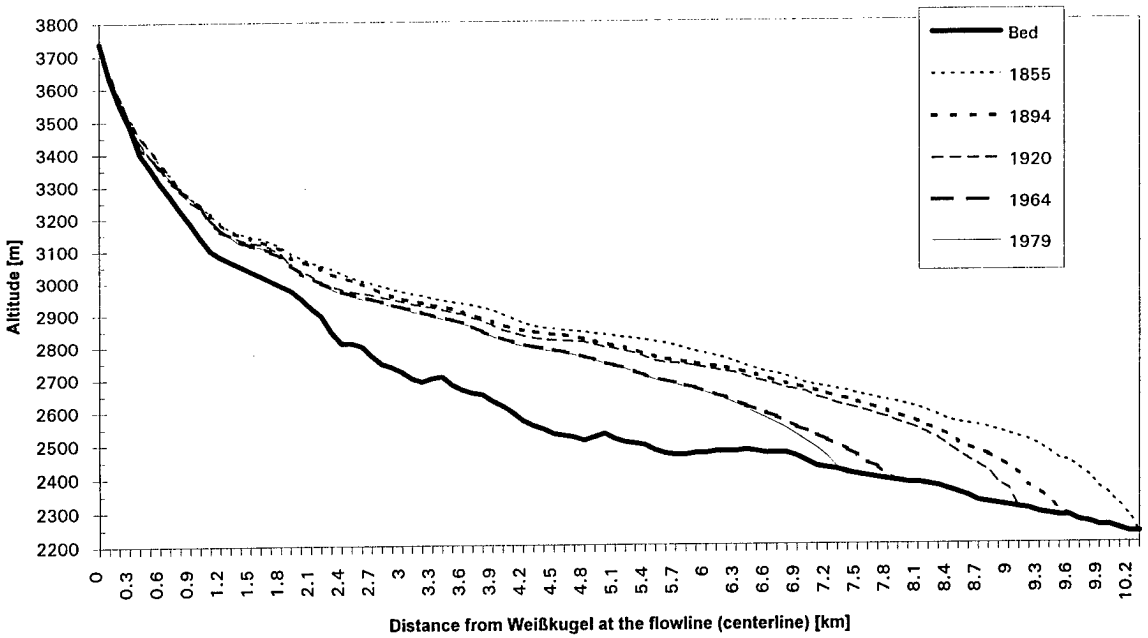

Figure 1. Longitudinal profiles along the central flow line of Hintereisferner. The 1855 profile is a reconstruction by Schlosser (1996); all other profiles are based on maps.

A comparable ice thickness was observed at cross profile 6 (180 m in 1979, at 6.0 km in Fig. 1). A continuous record of annual velocity measurements for this profile (*Linie 6*) is given in Figure 3. After a slow start from 17 m/a in 1933 to 24 m/a in 1940, velocity accelerates to more than 40 m/a in 1942. The subsequent decay is more gradual than in the early 1920's.

The acceleration from 14 m/a in 1965 to 32 m/a in 1978 was less dramatic than the previous two events, but the increase from 14 to 21 m/a after the strongly positive balance in 1965 is remarkable (Table 1).

A similar sequence of acceleration, advance and decay that had been observed on nearby Vernagtferner around 1900 is reproduced in Fig-

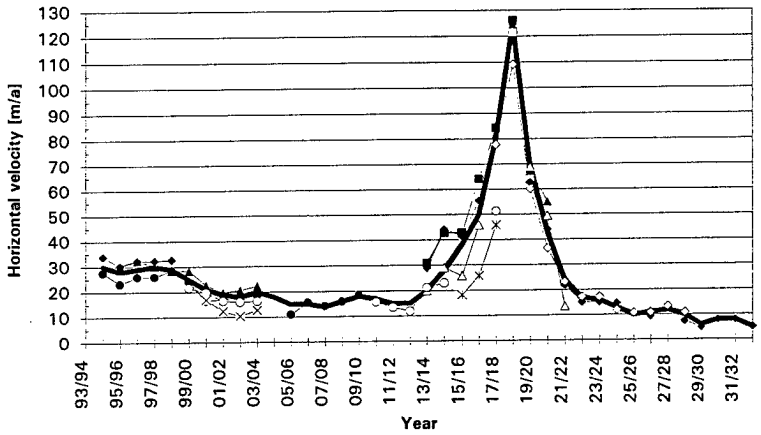

Figure 2. Horizontal velocities of the lower part of Hintereisferner, mean annual values from 1894–95 to 1932–33. The filled and open squares are situated at 8.1 and 8.2 km and the open circle and crosses at 8.9 and 9.1 km, respectively. Ice thickness was about 180 m at 8.1 km and nearly zero at 9.1 km. All stakes downward of 7.0 km reached their maximum velocity in 1919.

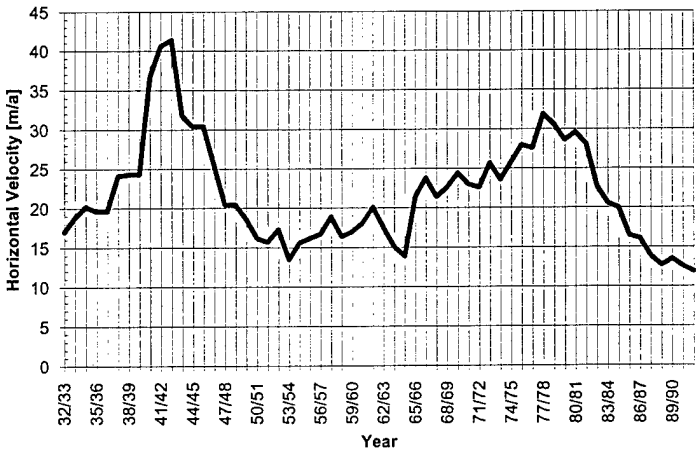

Figure 3. Horizontal velocities of Hintereisferner from 1932–33 to 1991–92, averages of 20 points on a cross profile at 6.0 km, ca. 2600 m elevation. Ten of twelve stakes between 1.0 and 6.8 km reached their maximum velocity in 1979, while the peak flow in 1943 is insufficiently documented longitudinally.

Table 1. Summary of accelerated flow events.

Period	*1914–19*	*1933–43*	*1965–78*
Initial velocity (m/a)	15	17	14
Peak velocity (m/a)	125	41	21
Ratio	8.3	2.4	1.5

ure 4 from Finsterwalder and Hess (1926). Although this one reaches peak velocitites twice as high as Hintereisferner in 1919, the acceleration over a period of 5 years and the subsequent return to quiescent flow is strikingly similar.

FLOW CONVERGENCE AND SURFACE ELEVATION

It is fortunate that of the five longitudinal cross sections given in Figure 1, three were taken in years of advance or acceleration: 1855, 1920 and 1979. They have distinctly steeper fronts than the two inactive cases of 1894 and 1964. Compared to a model steady-state calculation by Schlosser (1996), the real 1920 profile is several tens of meters thinner in the upper part (at down-glacier distances of 2 to 4 km in Fig. 1) and substantially thicker at the tongue.

This difference suggests that the acceleration was most pronounced in the central section of the glacier, with divergent flow in the upper basin and convergence near the terminus. From Figure 2 we observe a decrease of surface velocity from 80 m/a at 8.1 km to 45 m/a at 9.0 km in 1918, the terminus itself advancing at that time.

A further illustration of the mass flux convergence accompanying the 1919 acceleration is given in Figure 5, where the surface elevations at stakes on the lowermost 3 km of Hintereisferner are compared to the datum level of the summer of 1915. Two facts can be seen this graph: 1) the surface is raised most strongly at the end, as it should be with an advancing glacier, and 2) the acceleration proceeds as rather more block-like than wave-like. Within the resolution of once per year surveys, the upper three stakes have their highest elevation in 1919, the following in 1920 and only the last in 1921.

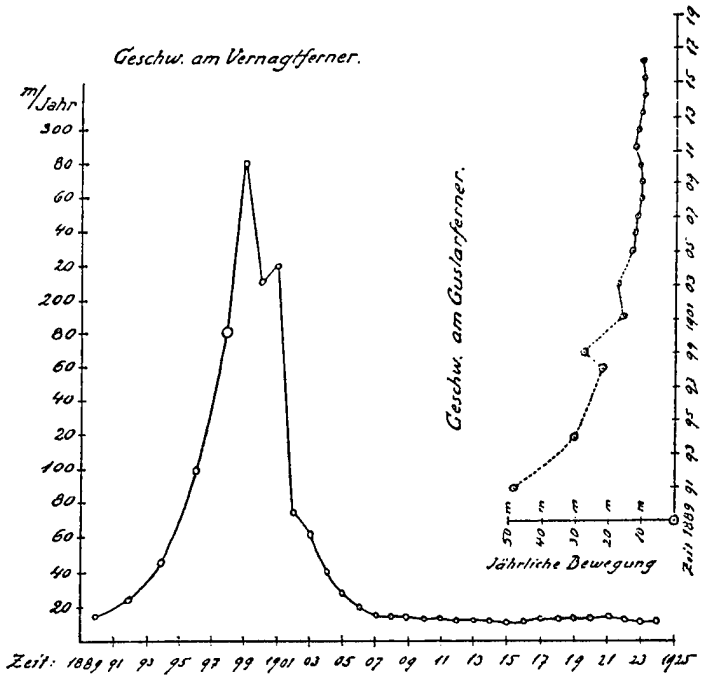

Figure 4. Velocities on the lower part of Vernagtferner, a close neighbor of Hintereisferner. Note that Vernagtferner exhausted its ice reserves in 1900 so that it was not able to take part in the 1919 advance of nearly all eastern alpine glaciers. Inset: Guslarferner, a former tributary of Vernagtferner, had only a minor acceleration in 1899.

CLIMATIC CONDITIONS, MASS BALANCE AND VELOCITY

From an inspection of Figure 6, it is obvious that a connection exists between the directly measured mean specific mass balance and ice velocity in the ablation area of Hintereisferner, the velocity reacting to changes in mass balance with a delay of 1 or sometimes 2 years. A particularly strong example is the acceleration from 13 to 21 m/a following the positive mass balance of 900 mm water equivalent.

To extend that series into the period without direct measurements of mass balance before 1952, we used data from two climate stations (Marienberg and Vent, either one less than 25 km away). We obtained best results with a combination of winter precipitation and the summer–winter temperature difference, both good indicators of maritime influence.

This parameter indicated conditions favorable for advances or accelerations in 1898, 1915, 1927, 1939 and 1965–75. Apparently, Hintereisferner had

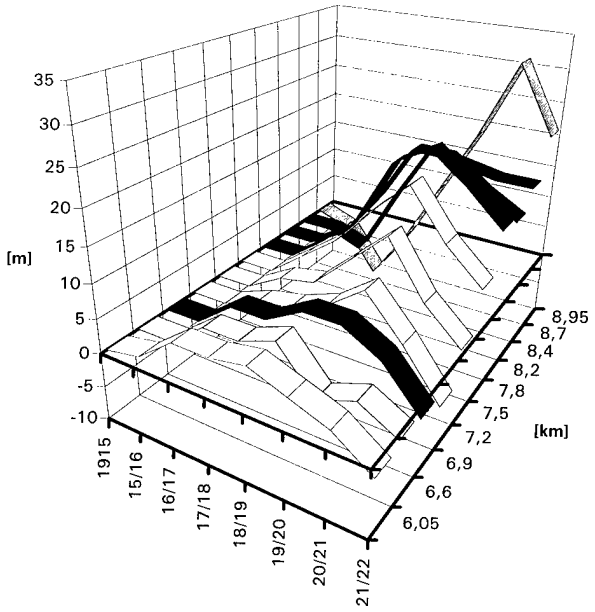

Figure 5. Surface elevations at stakes on the lowermost 3 km of Hintereisferner compared to the datum level of the summer of 1915. Note that the down-glacier distance is not exactly on a linear scale. The location of maximum change of surface elevation was progressing down-glacier by 3 km in 3 years.

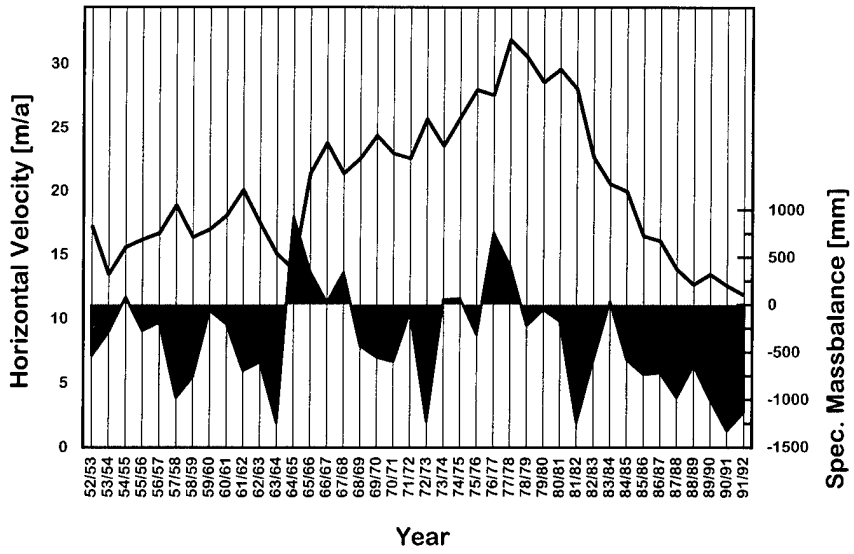

Figure 6. Time series of velocities at 6.0 km (as in Fig. 3) and mean specific mass balance of Hintereisferner. Most extremes of mass balance are followed by extremes of velocity with one or two years delay.

used so much of its ice reserves in the 1919 advance that it could not react to the positive conditions of 1927 (as other eastern alpine glaciers did); similarly, Vernagtferner had spent its mass in the 1900 surge so that it could not take part in the 1919 advance.

CHANGING MODE OF FLOW

From the climate and velocity records, it seems safe to say that the three phases of accelerated flow of Hintereisferner were initiated by several years of positive mass balance, the latter being a necessary but not always sufficient condition for extended acceleration.

The velocities of the three events cannot be explained by increased deformation alone, but require a strong contribution by basal or subglacial sliding. Particularly, the 1919 and 1943 maxima developed over several years, nearly independent of mass balance, once the initial conditions had been positive enough.

We propose that at least the 1919 and 1943 accelerations developed substantial crevassing of the lower and central part of the glacier, most likely also at the riegel in the rock bed at 2.0 km. Through these newly opened crevasses, meltwater penetrated to the bed and altered sliding conditions on the rock or subglacial till, filling cavities and building up basal water pressure. This would be in agreement with measurements at Findelengletscher (Iken and Bindschadler 1986) and Storglacären (Jansson 1995). These altered hydraulic conditions affected the major part of Hintereisferner in the same year and enabled a block-like movement with the surface sinking in the upper part and bulging and steepening on the tongue.

While in 1919 this motion extended down to the end of the glacier and caused an actual advance of 60 m, it did not reach the terminus in the 1943 and 1979 accelerations, but was evident in the slowdown of the general retreat in those years and in the longitudinal profile of 1979.

ACKNOWLEDGMENTS

This investigation has been sponsored by the National Committee for the IGBP at the Austrian Academy of Sciences.

LITERATURE CITED

Blümcke, A. and H. Hess (1899) Untersuchungen am Hintereisferner. *Wissenschaftliche Ergänzungshefte zur Zeitschrift des D. u. Ö. Alpenvereins*, 1. Band, 2. Heft. Bruckmann AG, München, 87 p.

Finsterwalder, S. and H. Hess (1926) Über den Vernagtferner. *Festschrift zum fünfzigjährigen Bestehen der Sektion Würzburg des Deutschen und Österreichischen Alpenvereins, Würzburg*, p. 30–41.

Greuell, W. (1992) Hintereisferner, Austria: Mass balance reconstruction and numerical modelling of the historical length variations. *Journal of Glaciology*, **38**(129): 233–244.

Hoinkes, H. (1970) Methoden und Möglichkeiten von Massenhaushaltsstudien auf Gletschern. *Zeitschrift für Gletscherkunde und Glazialgeologie*, **6**: 37–90.

Iken, A. and R.A. Bindschadler (1986) Combined measurements of subglacial water pressure and surface velocity of Findelengletscher. *Journal of Glaciology*, **32**(110): 101–119.

Jansson, P. (1995) Water pressure and basal sliding on Storglaciären, northern Sweden. *Journal of Glaciology*, **41**(138): 232–240.

Kuhn, M. (1981) Begleitworte zur Karte des Hintereisferners 1979, 1:10.000. *Zeitschrift für Gletscherkunde und Glazialgeologie*, **16**(1): 117–124.

Schimpp, O. (1960) *Der Haushalt des Hintereisferners; Akkumulation, Ablation und Gletscherbewegung in den Jahren 1952/53 und 53/54.* Veröffentlichungen des Museums Ferdinandeum in Innsbruck, Bd. 39. Universitätsverlag Wagner, Innsbruck.

Schlosser, E. (1996) Modellierung der neuzeitlichen Schwankungen des Hintereisferners. Thesis, Institute of Meteorology and Geophysics, University of Innsbruck, 150 p.

Span, N. (1993) Untersuchung der Dynamik des Hintereisferners zwischen 1894 und 1992. Thesis, Institute of Meteorology and Geophysics, University of Innsbruck, 110 p.

Tephrastratigraphy of Ablation Areas of Vatnajîkull Ice Cap, Iceland

GUDRÚN LARSEN, MAGNÚS T. GUÓMUNDSSON, HELGI BJÖRNSSON
Science Institute, University of Iceland, Sudurgötu, 101 Reykjavík, Iceland

ABSTRACT

Tephra horizons form isochrones in glaciers that may be useful to many studies of glacier dynamics and mass balance, in addition to being a record of the eruption history of glaciated regions. The tephrastratigraphy of Tungnaárjökull, an outlet glacier in the western part of the Vatnajökull ice cap, has been mapped in detail. A sequence of 38 horizons was found cropping out in the ablation area, whereof 34 consisted mostly of tephra. The chemical composition of the tephra has been determined by microprobe analysis, establishing the origin of 29 layers. Twenty-one layers originate in the Grímsvötn volcanic system, the majority from previously unknown eruptions. The remaining eight layers come from the volcanic systems of Veidivötn/Bárdarbunga (four), Katla (three) and Öræfajökull (one). Six tephra horizons have been accurately dated, including the acid tephra from the 1362 AD eruption in Öræfajökull and the tephra from the Laki/Grímsvötn eruption in 1783–84 AD, the youngest tephra layer in the sequence. The oldest layer is considered to be from the 12th century. Thus, the sequence of 34 horizons represents a continuous record of more than 600 years of volcanism and ice accumulation and is a valuable addition to the eruption history of subglacial volcanoes within Vatnajökull.

INTRODUCTION

Volcanoes can provide visible internal time markers or isochrones in glaciers by showering them with tephra, while the glaciers keep record of the eruption history of the volcanoes by preserving the tephra layers. Tephra layers that are deposited onto the accumulation areas of glaciers are buried by continued build-up of snow and descending flow of the ice. The tephra layers are preserved as distinct horizons in the ice and are seen as internal reflections by radar (Björnsson 1987), both in surging and non-surging glaciers. They crop out in ablation areas as dark, sinuous bands, consisting of ash- to lapilli-size tephra particles, and are prominent on glaciers within the active volcanic zones in Iceland.

The Vatnajökull Ice Cap covers the central part of the Eastern Volcanic Zone in Iceland (Fig. 1). The postglacial volcanism is confined to well-defined volcanic systems within the volcanic zone, and many have distinct geochemical characteristics that make it possible to recognize their products (Saemundsson 1979, Jakobsson 1979). This allows tephra layers to be correlated to their source with great confidence (Larsen 1981). Further, the eruption history of these volcanic systems during the last millennium is well known, as is the regional tephrochronology (Thorarinsson 1958, 1967, 1974, 1975; Larsen 1982, 1984; Björnsson and

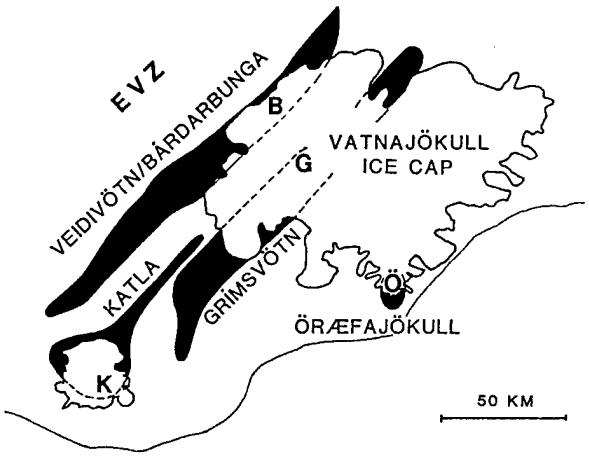

Figure 1. Vatnajökull ice cap relative to relevant volcanic systems of the Eastern Volcanic Zone. Their subglacial parts are indicated by broken lines.

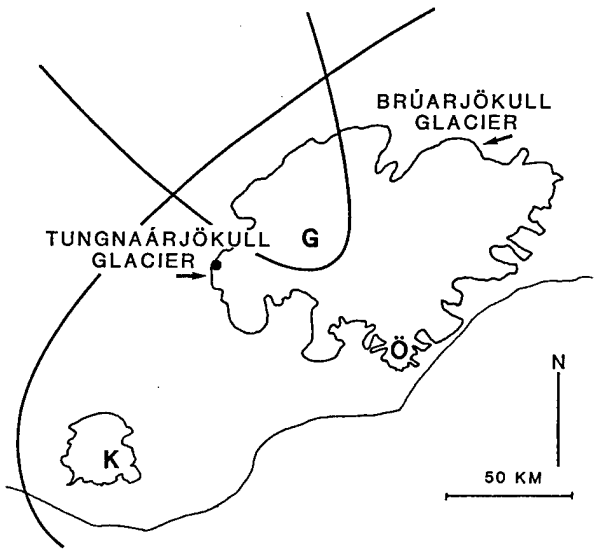

Figure 2. Outlines of two hypothetical fans of tephra deposited on Vatnajökull, one from Grímsvötn and the other from Katla volcano. The whole ice cap lies within the tephra fan from Katla, and that tephra layer should, as a result, be found on all the outlet glaciers, while the tephra from Grímsvötn will only appear on outlet glaciers in its western half. Dot at the edge of Tungnaárjökul indicates location of Figure 3.

Einarsson 1990; Gudmundsson and Björnsson 1991). Thus, tephra layers can be correlated to eruptions of known origin and age through investigation of the chemical composition of the glass and by comparison to historical records on eruptions and tephra falls.

The Vatnajökull Ice Cap partly overlies four volcanic systems, including the Grímsvötn, Öræfajökull and Veidivötn/Bárdarbunga systems. A great deal of the basaltic magma erupted on their ice-covered parts is therefore extruded as tephra, and altogether there is evidence of some 80 eruptions during the last 11 centuries (Björnsson and Einarsson 1990). These and other relevant volcanic systems are shown on Figure 1. Tephra layers from volcanoes both within and outside Vatnajökull have been deposited onto its accumulation area (Fig. 2).

The goal of our study is to map the tephrastratigraphy of the major outlet glaciers of Vatnajökull, obtaining information on the age of the ice and correlating the dated tephra horizons in the ablation areas to internal reflections seen by ice radars, thereby providing a tool for studies of glacier mass balance and dynamics. Further, this work is expected to add to the eruption history of the subglacial volcanoes within Vatnajökull during the last millennium, part of which may only be revealed from tephra layers in its ice.

PREVIOUS WORK ON GLACIER TEPHRASTRATIGRAPHY

In 1972, a 415-m deep hole was drilled into the ice near Bárdarbunga in the northwestern part of the ice cap for various glaciological and climatological purposes. Tephra layers were used to date the ice at various levels and to obtain knowledge of the eruption history of the subglacial volcanoes. The chemical composition of the volcanic glass was obtained by electron microprobe analysis of individual tephra grains. About 30 tephra layers were found in the Bárdarbunga core, which covered about 300 years back to the middle of the 17th century, but did not reach the bottom of the ice (Steinthórsson 1978).

TEPHRASTRATIGRAPHY OF TUNGNAÁRJÖKULL

Tungnaárjökull is a broad, lobelike outlet glacier of the Vatnajökull ice cap. The glacier, with its ice drainage area, is about 340 km^2 in size. The central flow line is 40 km long and the ice thickness is commonly 300–600 m. Tungnaárjökull has surged at least twice this century. The first recorded surge was in 1945–46, when the terminus advanced 1–2 km (Freysteinsson 1968). A second surge of similar magnitude took place in 1994–95. These surges have affected the entire length of the glacier. Sampling of the tephra layers reported here took place in 1994, just before the onset of the surge.

In the ablation area of Tungnaárjökull, some 38 dark bands of different width and continuity crop out, broadly parallel to the glacier terminus. The intervals between individual bands also differ and as a result a distinct pattern is formed that is easily recognizable everywhere on this particular glacier. Figure 3 shows part of the ablation area as it appeared on aerial photographs in the fall of 1986. Subglacial topography causes irregularities in the tephra bands and clean white snowdrifts of early winter make them appear more discontinuous than they really are. Comparison with aerial photographs taken in 1960 confirms that this pattern,

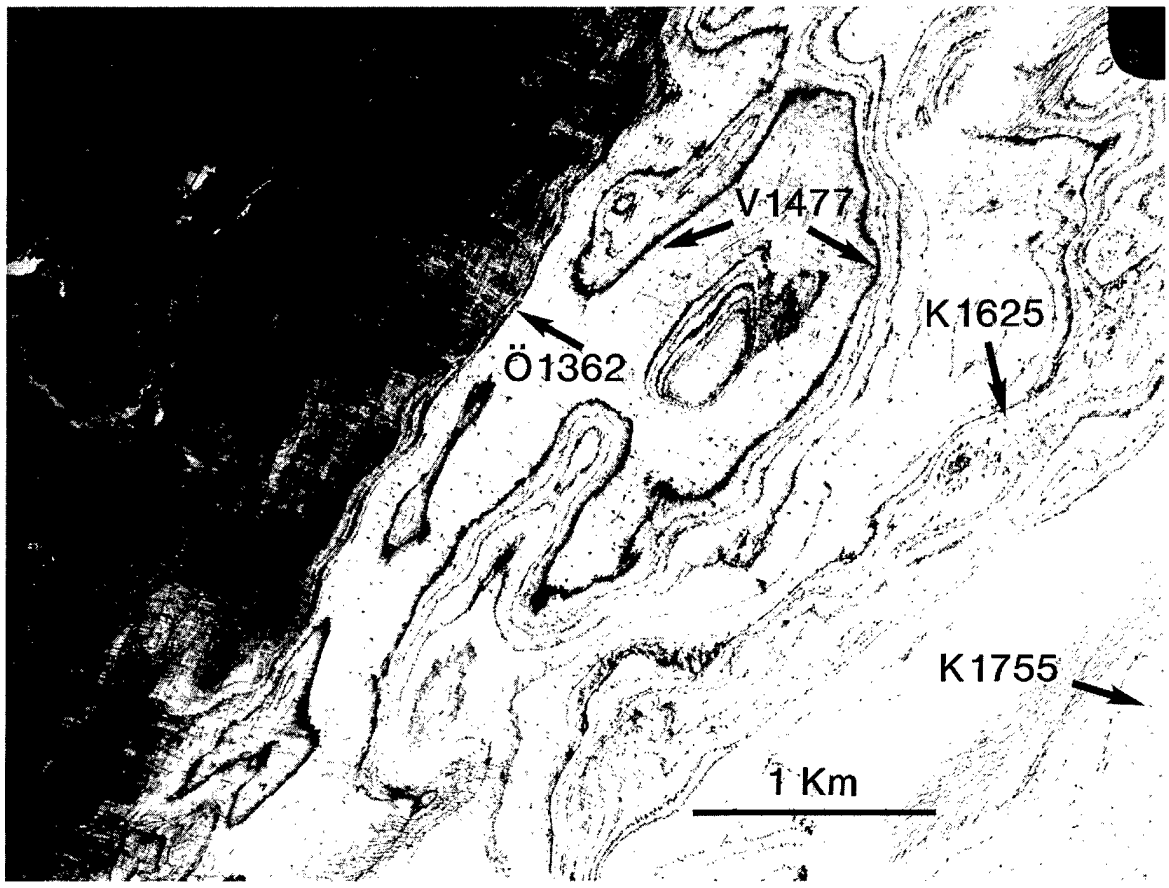

Figure 3. Part of the ablation area of Tungnaárjökull outlet glacier in 1986. Four tephra layers of known age are labeled with their respective eruption years. The acid Ö 1362 tephra is light-grey and does not show up on the photograph but lies immediately below the black horizon indicated by the arrow (Iceland Geodetic Survey).

i.e., the relative thicknesses or widths of the bands and intervals, has persisted over decades while the glacier has retreated and thinned. Most of the bands consist of ash- to lapilli-sized tephra particles and they are the surface expression of thin (millimeter to centimeter) but distinct horizons in the ice.

In crevasses, the tephra horizons can be observed in three dimensions in the ice. They cut the glacier surface at an angle, forming a notch at the intersection with the surface. Above the notch the ice is clean, in front of it the tephra is left to form a "dirt" band when the ice melts and the notch retreats during the melting season. Most of the tephra horizons form continuous or near-continuous layers in the ice, but in between are thinner and less continuous layers. The dips of the layers are 15–25° in the lower part of the ablation area, decreasing to 5–10° higher up.

Sampling of the tephra and measurements of dips and distances were done along several short, overlapping profiles perpendicular to the tephra bands. Oblique aerial photographs taken from low-flying aircraft were used for orientation on the glacier. The layers were sampled by taking short (0.5–1.5 m) cores, 7.5 cm in diameter, a few metres up-glacier from the notch. To obtain enough material for chemical analyses and studies of grain properties, mass loading, etc., one to three cores were extracted. The mass loading varied from a few grams to a few milligrams per square centimeter and the thickness from about 10 cm (an exception) to less than a millimeter.

A schematic section of the lower part of an outlet glacier, such as Tungnaárjökull, is shown on Figure 4. Tephra horizons or layers of different thickness are shown parallel to the bedrock topography. Also shown is how a subglacial hill causes irregularities on the glacier surface by bending ice and tephra layers upwards. Deformation by shearing is only observed at the snout, where horizons of debris, with much steeper dip than the tephra

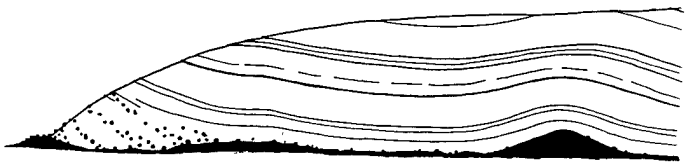

Figure 4. Sketch of an outlet glacier with tephra horizons, seen in a longitudinal section.

layers, also appear on the surface.

Of the 38 bands or horizons that cropped out in the ablation area, 34 consisted mostly of tephra. The remaining four, which cropped out between the lowermost tephra layer and the glacier terminus, consisted mostly of debris. Glass from all 34 horizons has been chemically analyzed by electron microprobe and the origin of 29 tephra layers has been established. The origin of the remaining five layers is less certain. Of the 29 layers, one originates in the Öræfajökull system, three in the Katla system, four in the Veidivötn/Bárdarbunga system and 21 in the Grîmsvötn system (Table 1). Two of the remaining five layers have intermediate composition which resembles that of older intermediate rocks reported from the Hágöngur area (Noe-Nygaard 1950) within the Grímsvötn system, one also containing a minor component with Grímsvötn composition. They are, therefore, believed to originate in that system. The other three consist of two or more glass types and may represent more than one tephra layer each. In addition, a tephra band with the chemical characteristics of the Katla system was found on the surface just below the equilibrium line.

Six tephra layers have been related to definite eruptions with known eruption years by combinations of chemical characteristics, tephrochronology of adjacent areas and historical records on eruptions and tephra falls. The oldest of these key layers is the silicic tephra layer from the 1362 eruption of the Öræfajökull volcano (Ö 1362). The youngest key layers are those of the Katla 1755 (K 1755) and Laki/Grímsvötn in 1783/84 (L/G 1783/84). The former provides a link between the Tungnaárjökull tephrastratigraphy and the 1972 Bárdarbunga ice core stratigraphy. The latter is the uppermost, well-discernible layer and is hidden in places by perennial snow. The key layers are listed in Table 2.

The tephra band emerging at the equilibrium line was probably deposited in the Katla eruption of 1918. No bands of tephra have been found in Tungnaárjökull between this layer and the L/G 1783/84 tephra. The eruption history of Vatnajökull in this period is well documented (Thorarinsson 1974) and moderate Grímsvötn eruptions are dominant. Tephra was mainly transported in easterly directions and what was transported westwards may have been deposited only in the upper part of the accumulation area of Tungnaárjökull. If so, ice flow has not transported these layers far enough down-glacier for them to be exposed in the ablation area. Four of the key layers are labeled on the aerial photograph of Tungnaárjökull in Figure 3. By interpolating between the key layers, the age of the other layers can be estimated. The oldest preserved layer dates back to the early 12th century; hence, the sequence represents roughly 600 years of volcanism and ice accumulation.

Of the 21+2 tephra layers from the Grímsvötn system, 11 layers can be fitted to previously known eruptions. The other 12 come from unreported eruptions and are an important addition to the volcanic history of Grímsvötn, both in terms of number of eruptions and frequency of eruptions in certain periods. The K 1625 tephra layer is a part of a series of 11 horizons; the other 10 layers represent as many eruptions in the Grímsvötn system, all

Table 1. Sources of the tephra horizons from volcanic systems. Two horizon of intermediate composition are preliminarily assigned to Grímsvötn volcanic system.

	No. of tephra layers		
Source of tephra	*Acid*	*Interm.*	*Basic*
Öræfajökull	1		
Katla			3
Veidivötn/Bárdarbunga			4
Grímsvötn		2	21

Table 2. Key tephra layers for dating on Tungnaárjökull.

Öræfajökull	1362	AD
Veidivötn	~1477	AD
Grímsvötn	1619	AD
Katla	1625	AD
Katla	1755	AD
Laki/Grímsvötn	1783/84	AD

taking place in the 17th century—or within less than 100 years—according to interpolation between key layers. In the 300 years before 1600 AD (using the same method), only eight tephra layers with the chemical signature of Grímsvötn system are found. A marked increase in eruption frequency on the Grímsvötn system around 1600 AD is implied, assuming that the tephra record in Tungnaárjökull is consistent throughout the 600-year period. This is supported by historic records that first mention Grímsvötn eruption around 1600 AD (Thorarinsson 1974).

The continuity of the tephra layers, both laterally and vertically, shows that the bulk of the ice has not been subjected to any significant shearing displacement along fault planes, either vertically or along the direction of flow. This is remarkable since Tungnaárjökull is a surging glacier. Surges may have occurred once or twice every century. However, within a few hundred meters from the terminus, where the ice thickness is less than 50 m, the occurrence of relatively steeply dipping horizons (more than 30°) containing clay and debris indicate shearing and sediment transport from the base along fault planes.

Preliminary results from Brúarjökull glacier in northern Vatnajökull indicate that several of the tephra layers found in Tungnaárjökull, including the one from the Öræfajökull eruption in 1362 AD, are also present there, providing firm links between outlet glaciers some 100 km apart.

SUMMARY AND CONCLUSIONS

The sequence of 34 tephra horizons in the ablation area of Tungnaárjökull represents about 600 years of volcanism and ice accumulation from the middle 12th century to the late 18th century.

Of these 34 layers, 29 have been pinpointed to definite volcanic systems, and six of those layers, from the period 1362–1783/84, have related to definite eruptions and serve as key layers for dating.

The number of eruptions known to originate from the Grímsvötn volcanic system during the 600-year period has almost been doubled by the tephra record in Tungnaárjökull glacier.

A significant increase in eruption frequency of that system occurred in the 17th century, the activity increasing by a factor of three in comparison to the previous centuries, while a definite low in the eruption frequency occurred in the 15th century.

The lateral and vertical continuity of the tephra layers in the surging glacier show that the bulk of the ice has not been subjected to any significant shearing displacement along fault planes, neither vertically nor along the direction of flow.

A link between the Tungnaárjökull tephrastratigraphy and the Bárdarbunga ice core is provided by the K 1755 AD tephra. The first results from Brúarjökull outlet glacier in the northern part of the ice cap indicate the presence of the Ö 1362 AD tephra, providing a chronological link 100 km across the ice cap.

ACKNOWLEDGMENTS

This study was supported by the Iceland Science Foundation (RANNÍS). Óskar Knudsen, and Elsa Vilmundardóttir are thanked for assistance in the field and Bjarni Richter for preparing the samples. Karl Gronvold helped us with the EMPA analyses, which were done at the Nordic Volcanological Institute.

LITERATURE CITED

Björnsson, H. (1987) Könnun jökla med rafsegulbylgjum (Radio echo-sounding of temperate glaciers). In *Í hlutarins e li* (Th.I. Sigfússon, Ed.). Menningarsjódur, Reykjavík, p. 279–292.

Björnsson, H. and P. Einarsson (1990) Volcanoes beneath Vatnajökull, Iceland: Evidence from radio echo-sounding, earthquakes and jökulhlaups. *Jökull,* **40:** 147–168.

Freysteinsson, S. (1968) Tungnaárjökull. *Jökull,* **18:** 371–388

Gudmundsson, M.T. and H. Björnsson (1991) Eruptions in Grímsvötn, Vatnajökull, Iceland, 1934–1991. *Jökull,* **41:** 21–45.

Jakobsson, S.P. (1979) Petrology of recent basalts of the Eastern Volcanic Zone, Iceland. *Acta Naturalia Islandica,* **26:** 1–103.

Larsen, G. (1981) Tephrochronology by micro-

probe glass analysis. In *Tephra Studies* (S. Self and R.S.J. Sparks, Eds.), p. 95–102.

Larsen, G. (1982) Gjóskutímatal Jökuldals og nágrennis (Tephrochronology of the Jökuldalur area). In *Eldur er í nordri* (H. Thórarinsdóttir, Ó.H. Óskarsson, S. Steinthórsson and Th. Einarsson, Eds.). Sögufélag, Reykjavík, p. 51–65.

Larsen, G. (1984) Recent volcanic history of the Veidivötn Fissure Swarm, southern Iceland—an approach to volcanic risk assessment. *Journal of Volcanol. and Geotherm. Res.*, **22:** 33–58.

Noe-Nygaard, A. (1950) Hágöngur, a partially subglacial volcano in SW-Vatnajökull. *Meddelser fra Dansk Geologisk Forening*, **11:** 513–521.

Saemundsson, K. (1979) Outline of the geology of Iceland. *Jökull*, **29:** 7–28.

Steinthórsson, S. (1978) Tephra layers in a drill core from the Vatnajökull ice cap. *Jökull*, **27:** 2–27.

Thorarinsson, S. (1958) The Öræfajökull eruption of 1362. *Acta Naturalia Islandica*, **2:** 1–99.

Thorarinsson, S. (1967) The eruptions of Hekla in historical times—a tephrochronological study. *The Eruptions of Hekla 1947–1948, I*, p. 1–170.

Thorarinsson, S. (1974) Vötnin strío. *Saga Skeioarárhlaupa og Grímsvatnagosa* (The swift flowing rivers. *The history of Grímsvötn jökulhlaups and eruptions*). Menningarsjódur, Reykjavík, p. 254.

Thorarinsson, S. (1975) Katla og annáll Kötlugosa (Katla and annals of its eruptions). *Árbók Feroafélags Islands 1975*, p. 124–149.

Lava and Ice Interaction: Controls on Lava Flow Morphology and Texture

D.T. LESCINSKY, J.H. FINK
Department of Geology, Arizona State University,
Box 871404, Tempe, AZ 85287-1404; 602-965-0828; e-mail: lescinsky@asu.edu

ABSTRACT

Mount Rainier has been identified as a significant hazard to the population of central Washington, in large part because of its extensive glacial cover. To better understand the hazard that it and other glaciated volcanoes present, the process of lava and ice interaction, its variety and its frequency, were studied. Observations of historical activity demonstrate that lava does melt ice, but at a relatively slow rate. As a consequence, lava is easily constrained within voids eroded into the ice by steam or running water, both before and during the eruption. Morphological features characteristic of lava flow confinement have been identified in older lava deposits now exposed by glacial retreat. These features are common in the Cascades Range of North America, and can be expected at glaciated stratovolcanoes worldwide. Features characteristic of the flow of lava into trapped water, such as pillow lava and hyaloclastites, are common in Iceland, Antarctica and central British Columbia, but rare at stratovolcanoes. This is attributable to the greater ability of flat-lying ice sheets to trap water compared to the relatively thin, sloping valley glaciers found on stratovolcanoes. Smaller textural features confirm ice and lava interaction, as well as providing insight into stress fields within the lava flows during cooling. By identifying the deposit features attributed to lava and ice interaction, it is possible to determine past eruption frequencies and to reconstruct environmental conditions, such as paleoslopes and ice thicknesses, and thereby to aid in predictions of future eruption hazards. Additional work is being undertaken to enable more quantitative estimates of eruption parameters and amounts of meltwater produced during lava eruptions at glaciated volcanoes.

INTRODUCTION

The Cascades Mountain Range extends from northern California to southern British Columbia. The active nature of this volcanic arc was demonstrated by the 1980 eruption of Mount St. Helens, Washington, that resulted in the deaths of more than 50 people and hundreds of millions of dollars in damage. Since then, continued population growth in the Cascades region and the possibility of renewed volcanic activity have raised considerable concern among civil planners and disaster prevention agencies. Mount Rainier, Washington, identified as the most potentially dangerous of the Cascades volcanoes owing to its proximity to major population centers and its style of activity, was designated a Decade Volcano in the early 1990's and targeted for detailed volcanological study and hazards evaluation (National Research Council 1994).

The greatest potential hazards at Mount Rainier and most other glaciated volcanoes are related to melting of near-summit snow and ice. At Mount St. Helens, debris flows and floods traveled down the flanks, choking river channels and causing destruction, from 1980 through 1990 (Simkin and Siebert 1994). In 1985, debris flows triggered by the eruption of Nevado del Ruiz, Colombia, destroyed the town of Armero and killed 25,000 of its inhabitants (Simkin and Siebert 1994). While these events involved explosive interactions with snow and ice, Mount Rainier is most likely to erupt non-explosively, producing lava flows from its summit crater (National Research Council 1994).

Figure 1. Llaima, Chile, following its May 1994 eruption. The dark lava visible on the summit glacier is located in a trench about 50 m deep, 50 m wide, and 2 km long. During the eruption, the lava is believed to have traveled down an enlarged subglacial drainage tunnel. Melting of the tunnel roof over a period of several days following the eruption exposed the lava flow.

Effusive activity at glaciated volcanoes can also produce debris flows as shown by the 1964 and 1971 eruptions of Villarrica, Chile, that resulted in the deaths of 22 and 15 people, respectively (Simkin and Siebert 1994).

The interaction between lava and ice is poorly understood, largely because of the inaccessibility of glaciated volcanoes. Reports on eruptive activity are fragmentary and consist primarily of observations made during brief overflights. Post-eruption ground-based studies are of limited value owing to the dynamic nature of glaciers and the resultant rapid burial, removal, or modification of volcanic deposits and glacial features related to lava and ice interaction. To better understand the processes involved, we have combined eruption observations with studies of older, better exposed deposits believed related to the interplay between ice and lava.

ERUPTION OBSERVATIONS

Published descriptions of 10 recent effusive eruptions were examined (Kamchatka—Kliuchevskoi 1974, 1983–84 in Doubik [1974] and Vinogradov and Murav'ev [1988]; Alaska—Okmok 1945 in Byers et al. [1947], Westdahl 1991 in Smithsonian Institution [1991, 1992], Veniaminof 1983–84, 1993–94 in Yount et al. [1985] and Smithsonian Institution [1993, 1994]; Chile—Llaima 1994 in Moreno and Fuentealba [1994]; Villarrica 1971, 1984–85 in González-Ferran [1973], Smithsonian Institution/SEAN [1989]; and Hudson 1991 in Naranjo et al. [1993]). During these eruptions, lava traveled over glaciers almost always constrained within channels or crevasses in the ice, that occasionally became tunnels for short distances (Fig. 1). The one exception was the 1945 Okmok eruption, during which a lava flow trav-

eling down the volcanic cone was deflected by the steep margin of a small glacier (Byers et al. 1947). Although these eruptions only represent a small portion of the range of ways ice can affect moving lava, they do provide some critical information. Lava does melt ice and can form debris flows, either through the release of ponded melt water, or by mixed avalanches generated during collapse of a lava flow's margin. However, the rate of direct thermal erosion by lava is relatively slow and lava flows are easily constrained by ice. Observations indicate that the most of glacial erosion and modification (the production of channels and crevasses in ice) is caused instead by the kinetic and thermal effects of flowing melt water.

DEPOSITS

To investigate a wider variety of lava and ice interactions, field studies of older volcanic deposits in the Cascades Range of North America (Fig. 2) were combined with published deposit descriptions. Many of these deposits were produced by activity during the Pleistocene and earlier periods of widespread glaciation, and have now been exposed by the recession of ice sheets and valley glaciers. This work revealed a number of large- and small-scale deposit features characteristic of eruption observations. A list of these features is shown in Table 1. The different large-scale deposit types and flow morphologies can be attributed to flow into water and flow confinement, while the small-scale deposit features reflect flow into water, quenching of lava and complicated stress fields in cooling lava.

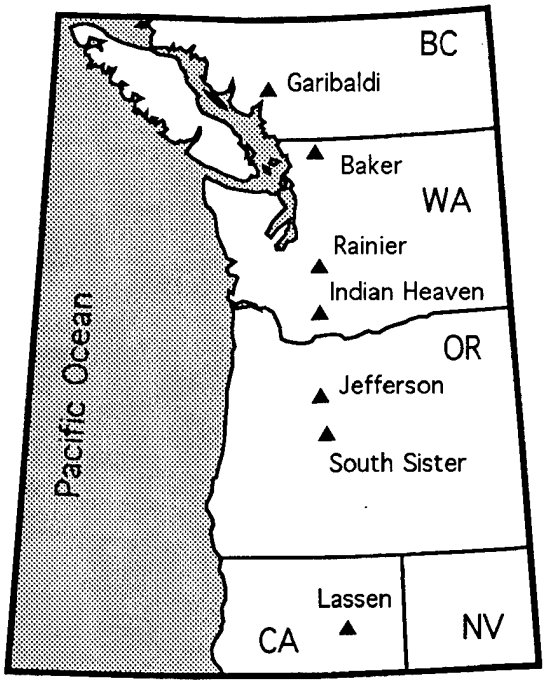

Figure 2. Volcanic sites in the Cascades Range of North America visited during this study.

Probably the best known example of lava and ice interaction is the extrusion of lava into sub- or peri-glacial lakes. This process is thought to produce the lava pillows, hyaloclastites, hyalotuffs and large-scale landforms such as tuyas (flat-topped mounds of subaerial lava overlying lava pillows and hyaloclastites—also called table mountains) and möberg formations (rolling hills of lava pillows and hyaloclastites) commonly found in central British Columbia, Iceland, and Antarctica. The meltwater forming the lakes can be produced over a period of years prior to eruption, because of increased heat flow and ponding of glacial runoff, or can be produced over a period of several days during an eruption (Noe-Nygaard 1940; Björnsson 1983, 1992). When sufficient water has accumulated, it lifts the glacier and escapes suddenly from under the ice as a jökulhlaup or outburst flood (Nye 1976). The thicker the layer of ice is, the greater the volume of water required to lift it. As a consequence, features indicative of lava extrusion into glacial lakes are rare in the Cascades Range where thinner ice sheets and steeper paleoslopes are not conducive to trapping large quantities of water.

As the amount of trapped meltwater is reduced, the importance of lava flow confinement by ice increases. Unusual lava deposit shapes and thicknesses indicate that lava traveled into and filled voids or trenches in ice. Many thick and steep-sided lava flows in the northern Cascades show evidence of paleovalley infilling–confinement by paleotopography that has subsequently been completely removed. This is consistent with confinement by layers of ice that have since retreated. More unusual lava deposit shapes include: pill-shaped (steep sided cylinders), V-shaped (attributed to syn-eruptive downslope ice movement [Conrey 1991]), laccolith-shaped, and esker-shaped. These deposits were produced by subglacial eruptions, with the first three shapes representing extrusion of domes and lava flows into voids above and surrounding the eruptive vents.

Cooling rates and stress fields within the lava are reflected in small-scale features and textures preserved in deposits. These features tend to be

Table 1. Features of volcanic deposits indicative of lava and ice (subaqueous) interaction found at: Mount Redoubt, Alaska; Mount Garibaldi, and the Tuya Region of British Columbia; Mount Rainier, Washington; Mount Jefferson and South Sister, Oregon; Nevado del Ruiz, Colombia; various locations in Iceland; and various locations in Antarctica (based on observations by the authors and Mathews 1947, 1951, 1952; Bemmelen and Rutten 1955; Walker and Blake, 1966; Jones 1969; Saemundsson 1970; Furnes et al. 1980; Conrey 1991; McIntosh and Gamble 1991; Smellie et al. 1993; LeMasurier et al. 1994; Skilling 1994; Smellie and Skilling 1994).

a. Large scale features and examples	
III. Evidence of large volumes of trapped water	
A. möberg (rolling hills of lava pillows and hyaloclastites)	Indian Heaven, Tuya, Iceland, Antarctica
B. tuya (flat-topped mounds of subaerial lava overlying lava pillows and hyaloclastites)	Tuya, Iceland, Antarctica
I. Evidence of confinement	
A. unusually thick deposit	Garibaldi, Baker, Rainier, Jefferson
B. perched lava flows	Garibaldi, Baker, Rainier, Jefferson
C. unusual shape	
1. steep margins	Garibaldi, Baker, Rainier, Jefferson
2. pill-shaped	Garibaldi
2. V-shaped	Jefferson
3. laccolith shaped	Garibaldi
4. esker shaped	Garibaldi, Iceland
b. Small scale features and examples	
I. Evidence of large volumes of trapped water	
A. lava pillows (basaltic composition)	Indian Heaven, Tuya, Iceland, Antarctica
B. cylindrical bodies (silicic composition)	Rainier, Jefferson, Iceland
C. hyaloclastites and hyalotuffs	Indian Heaven, Tuya, Iceland, Antarctica
II. Evidence of rapid quenching	
A. glassy texture	Cascades, Tuya, Iceland, Antarctica
B. small diameter polygonal joints	Cascades, Iceland
C. high entablature:colonnade thickness ratio	Garibaldi, Iceland
III. Evidence of complicated stress field	
A. "cordwood" (horizontal polygonal joints)	Baker, Rainier, Jefferson, South Sister, Redoubt, Nevado del Ruiz
B. "kubbaberg" (fan-like polygonal joints)	Garibaldi, Baker, Iceland
C. irregularly oriented polygonal joints	Cascades, Tuya, Iceland, Antarctica
D. sheet-like polygonal joints	Jefferson, South Sister, Caribou Wilderness
E. complicated structural stratigraphy	Baker, Rainier, Jefferson, South Sister, Caribou Wilderness

non-unique, forming also in subaqueous environments. However, when found on the steep slopes of a stratovolcano thought be to glaciated at the time of eruption, they provide strong evidence of lava and ice interaction. The presence of glass indicates rapid quenching and is frequently attributed to the presence of water surrounding the lava or traveling through cracks and fractures within solidified portions of the lava flow, or both, resulting in convective cooling. Convective cooling only requires relatively small amounts of water (i.e., rainfall [Hardee 1980]). Glass is ubiquitous at deposits attributed to lava and ice interaction, where it usually penetrates 2 to 5 m from the flow margin. Pervasive glass, tens of meters thick, has been reported from some localities (Conrey 1991).

Figure 3. Cross-sectional view of a subglacially erupted dacite lava dome at South Sister, Oregon. Polygonal joints bend from sub-horizontal at the left edge of the deposit to near vertical, indicating that cooling occurred towards a flow margin in contact with ice or water. The deposit is roughly 15 m thick and the left edge of the deposit is believed to coincide with the original flow margin.

Figure 4. Polygonal joints forming a chevron pattern in an andesite flow at Mount Baker, Washington. This pattern suggests a warping of isotherms related to heterogeneous permeability or continued flow movement during fracturing. Note the hat in the lower center of the photo for scale.

Polygonal joints or columns are another commonly observed deposit feature. They are produced by incremental fracturing, triggered by the accumulation of stress associated with thermal contraction of the lava (Ryan and Sammis 1978). While polygonal joints are found in lava deposits that were emplaced subaerially with no evidence of water or convective cooling, these columns have relatively large diameters (generally 80–200 cm) and are associated with conductive cooling processes. Smaller diameter columns (frequently 5–20 cm), such as those in glacial areas, are attributed to more rapid convective cooling (Long and Wood 1986, DeGraff and Aydin 1993, Grossenbacher and McDuffie 1995). Differential cooling rates can lead to the development in some lava flows of a thick upper zone of thin columns (entablature) and a relatively thin lower zone of wide columns (colonnade). This sequence is believed to represent upward convective cooling related to circulating water and downward conductive cooling (Saemundsson 1970, DeGraff et al. 1989).

Because polygonal joints are produced when fractures propagate away from a cooling surface (the flow margin) toward the direction of maximum stress, they can be used to locate original flow margins and as paleostress indicators. The wide range of observed joint orientations indicates that cooling is not always vertical. For example, horizontal columns indicate cooling toward steep flow margins (Fig. 3). More irregular joint patterns such as bends, chevrons (Fig. 4), and kubbaberg (fans) evade simple explanation, but are likely caused by warping of isotherms related to heterogeneous permeability or continued flow movement during fracturing.

Several types of "sheeted" columns have been observed at deposits attributed to lava and ice in-

teraction. These four-sided columns share a single bounding fracture with their neighbors. Typically, polygonal joints have five to seven sides, reflecting the isotropic stress field associated with thermal contraction. The tetragonal shape of the "sheeted" columns suggests more complex boundary conditions, such as flow confinement by an ice wall, coupled with thermal contraction. Some of these joints also show evidence of water circulation and a second phase of fracturing.

Polygonal joints seldom extend through an entire lava flow other than near the margins. The most common stratigraphy includes columns at the deposit base, overlain by a broadly jointed (several meters diameter, sometimes tetragonal) interior with platy texture, topped by more columns. The platy texture occasionally extends into a transition zone with columns and suggests shear associated with continued flow movement. This stratigraphy indicates that fracturing and polygonal joint formation can occur prior to the end of flow emplacement.

HAZARD IMPLICATIONS

Eruption observations and examinations of deposits provide important clues to interpreting past volcanic activity and predicting future hazards. Identifying characteristic large- and small-scale features can help determine the frequency of eruptions that have included lava and ice interaction and estimate the thickness and location of former ice sheets. The absence or lack of tuyas and möberg formations in the Cascades suggests that future eruptions of Mount Rainier will not involve the trapping of large quantities of meltwater nor the production of jökulhlaups. Evidence of lava flow confinement does, however, increase the likelihood of extensive melting of glaciers and the formation of large voids in ice. The slow rate at which lava can melt ice means that meltwater production will be near continuous and associated predominantly with kinetic and thermal erosion by flowing water. This process will result in high water flow rates and probably flooding. Debris flows, normally associated with the sudden production or release of water, would be less common and rather small, resulting from hot avalanches or pyroclastic flows caused by collapse of a lava flow front, or by the sudden release of meltwater ponded behind collapsed ice blocks. We are currently using laboratory simulations and analytical models in conjunction with field observations to better quantify estimates of cooling rates, meltwater production and eruption parameters such as effusion rate and paleoslope.

ACKNOWLEDGMENTS

This work is supported by National Aeronautics and Space Administration Grant NAGW-529 and National Science Foundation Grant OCE93-16831 to Fink and National Science Foundation Grant EAR94-21455 to S.N. Williams.

LITERATURE CITED

Bemmelen, R.W.v., and M.G. Rutten (1955) Tablemountains of Northern Iceland. Leiden, Netherlands: E.J. Brill, 217 p.

Björnsson, H. (1983) A natural calorimeter at Grímsvötn, an indicator of geothermal and volcanic activity. *Jökull,* **33:** 13–18.

Björnsson, H. (1992) Jokulhlaups in Iceland: prediction, characteristics and simulation. *Annals of Glaciology,* **16:** 95–106.

Byers, F.M., D.M. Hopkins, K.L. Wier and B. Fisher (1947) Volcano investigations on Umnak Island (1946). Progress of Investigations in 1946, Part 4. U.S. Geological Survey Alaskan Volcano Investigations Report 2, p. 19–53.

Conrey, R.M. (1991) Geology and petrology of the Mt. Jefferson area, High Cascade Range, Oregon. Ph.D. Dissertation, Washington State University.

DeGraff, J.M. and A. Aydin (1993) Effect of thermal regime on growth increment and spacing of contraction joints in basaltic lava. *J. Geophys. Res.,* **98:** 6411–6430.

DeGraff, J.M., P.E. Long and A. Aydin (1989) Use of joint-growth directions and rock textures to infer thermal regimes during solidification of basaltic lava flows. *J. Volcanol. Geotherm. Res.,* **38:** 309–324.

Doubik, Y.W. (1974) Klyuchevskoy volcanic activity. Center for Short-Lived Phenomena Annual Report 1974, p. 134–136.

Furnes, H., I.B. Fridleifsson and F.B. Atkins (1980) Subglacial volcanics—on the formation of acid hyaloclastites. *J. Volcanol. Geotherm. Res.,* **8**(1): 95–110.

González-Ferran, O. (1973) Description of volcanic eruptions—Villarrica. *Bull. Volcan. Erupt.,* **11:** 41–42.

Grossenbacher, K.A. and S.M. McDuffie (1995)

Conductive cooling of lava: columnar joint diameter and stria width as function of cooling rate and thermal gradient. *J. Volcanol. Geotherm. Res.*, **69:** 95–103.

Hardee, H.C. (1980) Solidification in Kilauea Iki lava lake. *J. Volcanol. Geotherm. Res.*, **7:** 211–223.

Jones, J.G. (1969) Intraglacial volcanoes of the Laugarvatn region, south-west Iceland—I. *Q. J. Geol. Soc. Lond.*, **124:** 197–211.

LeMasurier, W.E., D.M. Harwood and D.C. Rex (1994) Geology of Mount Murphy volcano: An 8-m.y. history of interaction between a rift volcano and the West Antarctic ice sheet. *Geol. Soc. Amer. Bull.*, **106:** 265–280.

Long, P.E. and B.J. Wood (1986) Structures, textures, and cooling histories of Columbia River basalt flows. *Geol. Soc. Amer. Bull.*, **97:** 114–155.

Mathews, W.H. (1947) "Tuyas," flat-topped volcanoes in northern British Columbia. *Amer. J. Sci.*, **245**(9): 560–570.

Mathews, W.H. (1951) The Table, a flat-topped volcano in southern British Columbia. *Amer. J. Sci.*, **249:** 830–841.

Mathews, W.H. (1952) Ice-dammed lavas from Clinker Mountain, southwestern British Columbia. *Amer. J. Sci.*, **250:** 553–565.

McIntosh, W.C. and J.A. Gamble (1991) A subaerial eruptive environment for the Hallett Coast volcanoes. In: *Geological Evolution of Antarctica* (M.R.A. Thomson, J.A. Crame and J.W. Thomson, Eds.). Cambridge, England: Cambridge University Press, p. 657–661.

Moreno, R.H. and C.G. Fuentealba (1994) The May 17–19 1994 Llaima volcano eruption, southern Andes (38°42'S-71°44'W). *Rev. Geol. de Chile*, **21:** 167–171.

Naranjo, S.J.A., R.H. Moreno and N.G. Banks (1993) La erupción del Volcán Hudson en 1991 (46°S), Región XI, Aisén, Chile. Serv. Nac. Geol. Min. Boletín 44, 50 p.

National Research Council (1994) Mount Rainier, Active Cascade Volcano. Washington, DC: National Academy Press, 114 p.

Noe-Nygaard, A. (1940) Subglacial volcanic activity in ancient and recent times. *Folia Geographica Danica*, **1**(2).

Nye, J.F. (1976) Water flow in glaciers: jökulhlaups, tunnels and veins. *J. Glaciol.*, **17**(76): 181–207.

Ryan, M.P. and C.G. Sammis (1978) Cyclic fracture mechanisms in cooling basalt. *Geol. Soc. Amer. Bull.*, **89:** 1295–1308.

Saemundsson, K. (1970) Interglacial lava flows in the lowlands of southern Iceland and the problem of two-tiered columnar jointing. *Jökull*, **20:** 62–77.

Simkin, T. and L. Siebert (1994) Volcanoes of the World, 2nd Ed. Tuscon, Arizona: Geoscience Press, 349 p.

Skilling, I.P. (1994) Evolution of an englacial volcano: Brown Bluff, Antarctica. *Bull. Volcanol.*, **56:** 573–591.

Smellie, J.L., M.J. Hole and P.A.R. Nell (1993) Late Miocene valley-confined subglacial volcanism in northern Alexander Island, Antarctic Peninsula. *Bull. Volcanol.*, **55:** 273–288.

Smellie, J.L. and I.P. Skilling (1994) Products of subglacial volcanic eruptions under different ice thicknesses: two examples from Antarctica. *Sed. Geol.*, **91:** 115–129.

Smithsonian Institution (1991) Descriptions of volcanic events—Westdahl. *Global Volcanism Network Bull.*, **16**(11): 2; (12): 3.

Smithsonian Institution (1992) Descriptions of volcanic events—Westdahl. *Global Volcanism Network Bull.*, **17**(1): 4.

Smithsonian Institution (1993) Descriptions of volcanic events—Veniaminof. *Global Volcanism Network Bull.*, **18**(7): 3–4; (10): 3–4.

Smithsonian Institution (1994) Descriptions of volcanic events—Veniaminof. *Global Volcanism Network Bull.*, **19**(2): 6–7; (4): 8–9; (9): 14.

Smithsonian Institution/SEAN (1989) Global Volcanism 1975–1985. American Geophysical Union, Washington, D.C. Englewood Cliffs, NJ: Prentice Hall, 657 p.

Vinogradov, V.N. and Y.D. Murav'ev (1988) Lava–ice interaction during the 1983 Klyuchevskoi eruption. *Volcanol. Seismol.*, **7**(1): 39–61.

Walker, G.P.L. and D.H. Blake (1966) The formation of a palagonite breccia mass beneath a valley glacier in Iceland. *Quat. J. Geol. Soc. Lond.*, **122:** 45–61.

Yount, M.E., T.P. Miller, R.P. Emanuel and F.H. Wilson (1985) Eruption in the ice-filled caldera of Mount Veniaminof. In: The United States Geological Survey in Alaska: Accomplishments during 1983 (S. Bartsch-Winkler and K.M. Redd Eds.). U.S. Geological Survey Circular 945, p. 58–60.

Counting Glaciers: Use of Scaling Methods to Estimate the Number and Size Distribution of the Glaciers of the World

M. F. MEIER
INSTAAR and Department of Geological Sciences,
University of Colorado, Boulder, CO

D. B. BAHR
CIRES, University of Colorado, Boulder, CO

ABSTRACT

Global and regional syntheses of glacier melt and runoff are needed for understanding present and future sea-level rise, as well as for hydrological and climatological analyses. Observational data on glacier areas are needed for modeling glacier–climate interactions and runoff, but are available for only a few regions. Data on the distributions of sizes and thicknesses are critical for modeling the glacier contribution to sea-level change, but are even fewer. The problem of insufficient data is addressed by two scaling applications: one relating numbers of glaciers to their size (area) distribution, and one relating volume to area. Glacier inventory data suggest distinctive relations between the numbers of glaciers larger than certain area to that area. The form of this relation appears to approximate the product of a power law times an exponential, with parameters differing regionally. Knowing the approximate total area of glacier ice in each region and the approximate sizes of the largest glaciers, the numbers and size distributions of glaciers in regions and the world can be determined. Bahr and others have shown that measured glacier volumes are proportional to surface area raised to a power, allowing volumes and mean thicknesses to be estimated based on the area distributions. These two relationships can then be combined to determine the volume of glacier ice on Earth, the number of glaciers, the distribution of ice thickness, and (with additional data) the distribution of glacier response times.

INTRODUCTION

Does the global set of glacier measurements contain regularities—such as fractal distributions—that can be used for the estimation of glacier numbers, areas, thicknesses, and volumes for the unmeasured ice masses? Better knowledge of the global distribution of land ice, including mountain glaciers and high-latitude ice caps, has become important with the developing interest in the global earth system and how it is changing.

1. Changes in land ice affect global sea level (e.g., Meier 1984, Warrick and Oerlemans 1990, Warrick et al., in press). Understanding present sea-level rise and projecting future rise attributable to global warming requires knowledge of ice areas (needed to compute ice wastage), ice thickness distributions (influences the response times to changes in climate [Jóhannesson et al. 1993]), as well as the thickness/area distribution (controls the loss of contributing ice area and volume from thinning).

2. Changes in ice volume affect the water balance of high-altitude and high-latitude areas. This affects river runoff and water supply (and thus water-resource planning) and climate feedbacks in some areas, as well as riparian ecology and other qualities of these environments.

3. There is a human desire to know the Earth; glaciers are distinctive features but generally oc-

cur in relatively inaccessible areas where mapping and other observations are meager. We have only rough guesses about the volume of glacier ice (exclusive of the ice sheets) on Earth; published values differ by at least a factor of two.

In this paper we note that several regular patterns appear in the empirical data, which can then be used to make a preliminary estimate of the global distributions. This involves three steps: 1) determining the numbers of glaciers of different areas in different regions, including estimating the distribution of areas in unmeasured regions and the distribution of smaller glaciers in measured areas; 2) given the above, determining the thickness and volume distributions; and 3) summing these regional results to get a first estimate of the global distribution of glacier areas, thicknesses, and volumes, including sea-level equivalents.

ESTIMATING NUMBERS OF GLACIERS AS A FUNCTION OF SIZE

Two problems must be overcome: too few measured data (inventories) exist, and, even in those areas with detailed inventory data, the small glaciers are often not included. The paucity of measured data is illustrated by the fact that the most recent publication of the World Glacier Inventory program (IAHS[ICSI]-UNEP-UNESCO 1989) lists about 35 detailed inventories (only four in the United States) totaling about 36,000 glaciers with total area of about 90,000 km^2. These are just $^1/_4$ and $^1/_8$ of the global totals by our estimate. (Note that these numbers may be increased somewhat by a detailed inventory of glaciers in the former Soviet Union, which is just now being made available in machine-readable format.)

The fact that small glaciers may be unnoticed even in relatively complete inventories is illustrated in Figure 1. Glaciers have been studied and mapped very carefully over many years in the European Alps, and the resulting area/number distribution shows many glaciers of small size, down to less than 2^{-5} (0.03) km^2. The Svalbard curve suggests a cutoff below about 1 km^2. Small glaciers exist on Svalbard, and in most other glacierized regions, but were not counted. Thus, the left-hand side of the Svalbard graph needs to be completed in some way.

Cumulative distributions of area vs. size are plotted as log-log graphs in Figure 2, for five typical, detailed inventories. Only the graph for Neuquen Sur suggests a straight-line (power law)

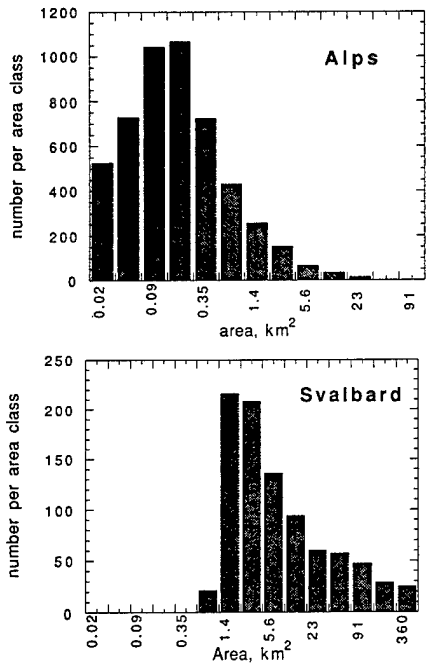

Figure 1. Number of glaciers as a function of area for the European Alps and Svalbard. Numbers are in bins by area increasing by powers of 2; the lowest bin includes glaciers ranging in area from 2^{-6} to 2^{-5} km^2. Data from IAHS[ICSI]-UNEP-UNESCO (1989).

relation; this is an area of very tiny glaciers. All of the others (and in fact almost all inventory data tested) show curves that depart from a power-law over part of the size range. In the case of the South Norway and North Scandinavia curves, the flattening of the curves at low areas is ascribable in part to the smaller glaciers were not being measured, but this does not apply to the Stikine and Alps data sets. Note that the two Scandinavian curves are similar, even though South Norway is in a warm, maritime environment, and Northern Scandinavia is an area with cold-temperate to subpolar glaciers.

These curves, and others not shown, show a rather distinctive shape, so the questions are:

1. Can these curves be described mathematically?

2. Is there a physical basis for the mathematical description?

3. Can this description be used to extend the results to unmeasured areas?

Much attention is now being given to the fractal

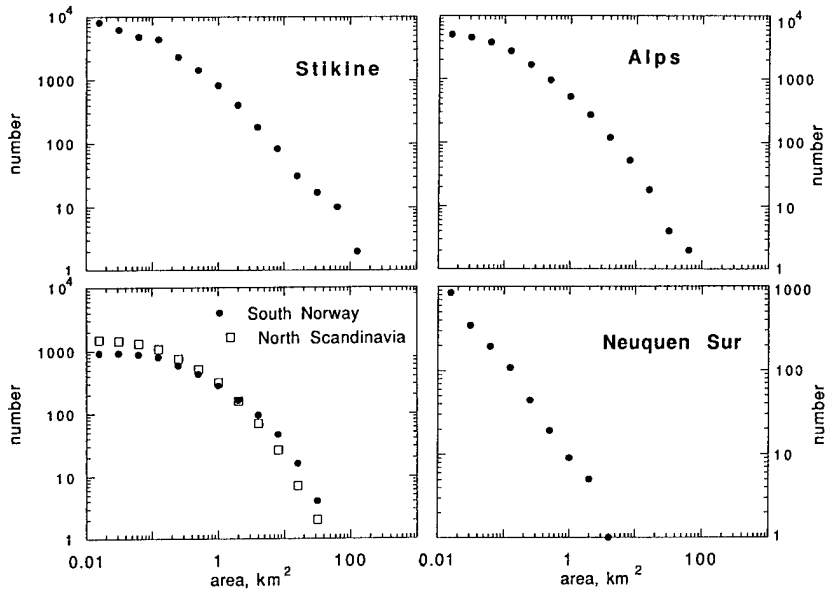

Figure 2. Cumulative plots of numbers of glaciers with areas greater than a given area, versus that area, for five typical areas: Stikine River, British Columbia, Canada; European Alps; South Norway and North Scandinavia; and Neuquen Sur, Argentina. Data from IAHS[ICSI]-UNEP-UNESCO (1989).

description of landscape elements. Perhaps the closest analog to glaciers is the distribution of snow patches, which has been studied by Shook and coworkers in the Canadian Prairies and in the Alps (Shook et al. 1993). They predict and find a power-law relation (Fig. 3). However, the curves shown in Figure 2 depart from a power-law relation in a distinctive way, suggesting that an appropriate description might involve a combination of a power-law and an exponential.

One of us (D. B. Bahr) has suggested that an explanation for the shape of these curves might be found using percolation theory. If one assumes that in a given region the mass balance at any particular grid cell is given by the sum of a mean balance (constant for the region) plus a random perturbation, then in some grid cells the balance may be positive, resulting in snow accumulation. Thus, clusters may occur, which can be identified as the accumulation areas of glaciers. Percolation theory then suggests, on the basis of certain further assumptions, that the area distributions may be described by a relation involving the area raised to a power times an exponential involving area (Stauffer and Aharony 1991). Which of these functions is dominant may depend on the cluster density. This might explain the difference between the

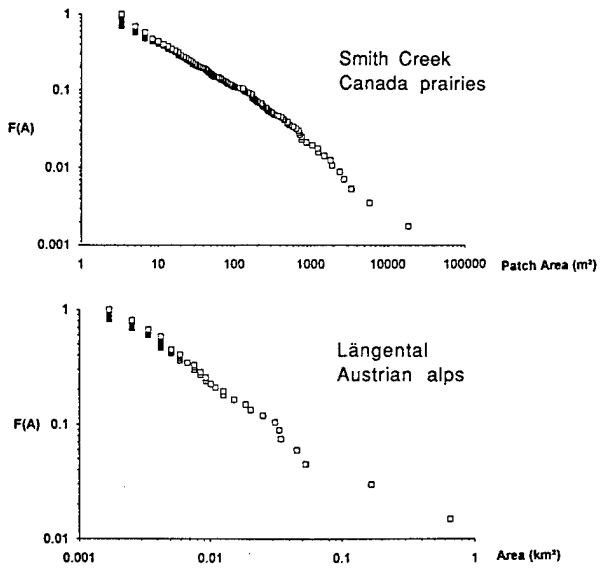

Figure 3. Cumulative plots for snow patch area distributions for Smith Creek drainage in the Canadian Prairies and Längental in the Austrian Alps. F(A) is the fraction of the number of snow patches having an area equal to or greater than the area A (from Shook et al. 1993).

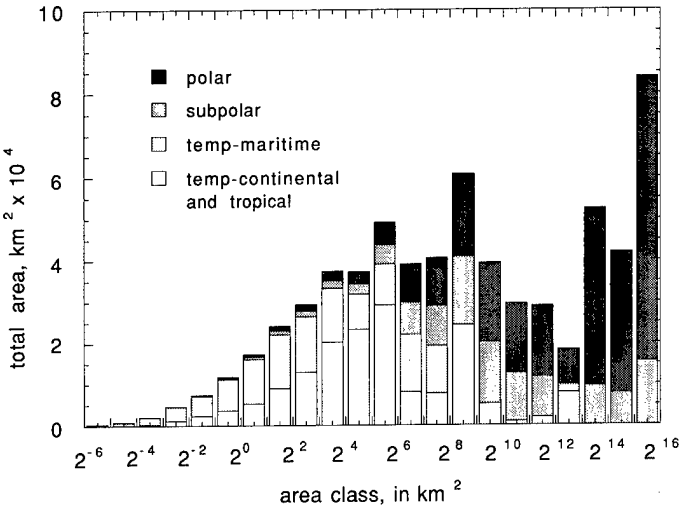

Figure 4. Histogram showing the total area of glaciers in the world as a function of glacier size. The histograms are also divided into four broad climatic regions.

glacier (Fig. 2) and snow-patch (Fig. 3) distributions. Although the physics is not yet developed, the curves shown in Figure 2 do suggest that a power-law times exponential description is appropriate for the observational data.

Lacking a physics-based model, we fitted empirical curves to each set of inventory data, and assumed that these curves had regional validity. Then these results could be used to calculate the shape of the area distribution functions for unmeasured areas. Two important constraints on this method strengthen the result: 1) the total area of glaciers in most areas has been estimated and the integrated area distributions must agree with these estimates, and 2) the area distribution depends on the size of the largest glaciers, which is known for most areas. These regional results were then summed to produce an estimate of the area distribution function for the glaciers of the world (Fig. 4).

ESTIMATING ICE THICKNESSES AND VOLUMES

Several authors (e.g., Zhurovlyev 1985, Macheret et al. 1988, Chen and Ohmura 1990, Meier 1993) have suggested that the volumes of mountain glaciers are proportional to their area raised to a power of about 1.36, and Bahr et al. (in press) have shown the physical basis for this power-law relationship. We have done a survey of the literature (a list of references is available from the authors) to locate glaciers with reliable, recent thickness measurements (mostly by radio-echo sounding) that could be used to test this relationship. This expanded study confirms the result obtained earlier, and shows little variation for glaciers in different regions. The results for 144 glaciers, exclusive of large ice caps, are shown in Figure 5. Only small differences between geographic regions (and, therefore, glacier type and climatic environment) are seen in these data. A composite of data from all four regions indicates an exponent of 1.36 with a squared correlation coefficient (r^2) of 0.99 (Fig. 6). Ice caps larger than 200 km^2 also show a power relationship (Fig. 7), but the exponent is significantly lower (about 1.22); this has been suggested before and is consistent with simple models of ice sheet dynamics (e.g., Paterson 1972) and with the Bahr et al. (in press) analysis for ice masses with equilibrium lines near the perimeter, both of which predict a value of about 1.25.

SUMMARY

These results can be assembled to produce a current estimate of the numbers, areas, mean thicknesses, and volumes of glaciers and ice caps on Earth. Detailed results of these compilations are

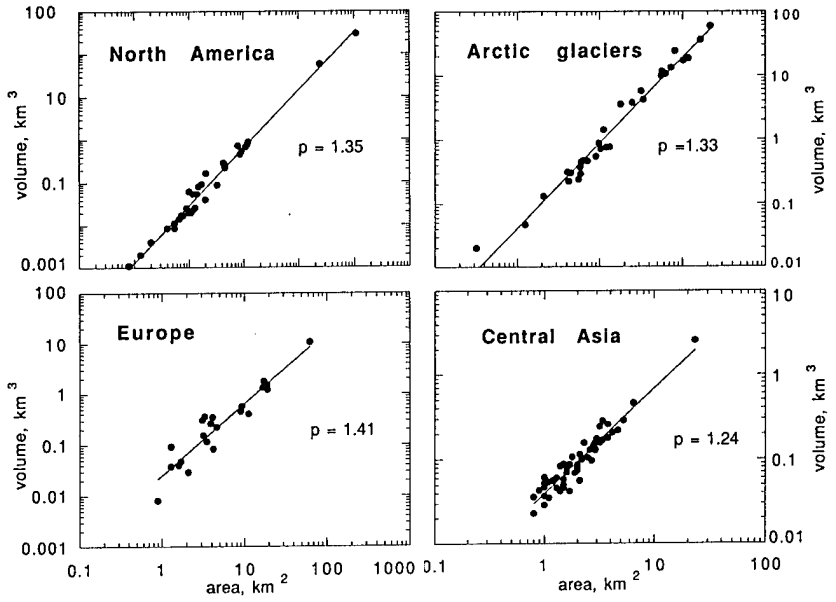

Figure 5. Plots of volume vs. area for measured mountain glaciers.

voluminous and are not presented here. However, some interesting results do appear:

1. Much of the mountain glacier area is contained in individual glaciers larger than 10 km^2, and especially in glaciers larger than 100 km^2 in area (Fig. 4). Yet, most of the glaciers currently being monitored for mass balance and glacier–climate interactions are less than 10 km^2 in area and many are even less than 1 km^2. Can these be considered representative of the world's glacier cover?

2. The response times of glaciers depend on thickness as well as the mass balance rates. Assuming reasonable balance rates, the calculated response times range from less than 10 to more than 1000 years, a difference of more than two orders of magnitude. Yet models to project sea-level rise for given climate scenarios typically assume (or calculate) a single response time for the world's glacier cover. Our results suggest that these models need to be revisited.

3. The estimated total volume of glacier ice on Earth, exclusive of the Greenland and Antarctic Ice Sheets, is slightly larger than most previous estimates, and is about equally divided between ice caps (larger than 200 km^2) and mountain glaciers (of all sizes up to about 5000 km^2), as shown in Table 1. One reason for the larger estimate of glacier volume, and especially glacier area, is the

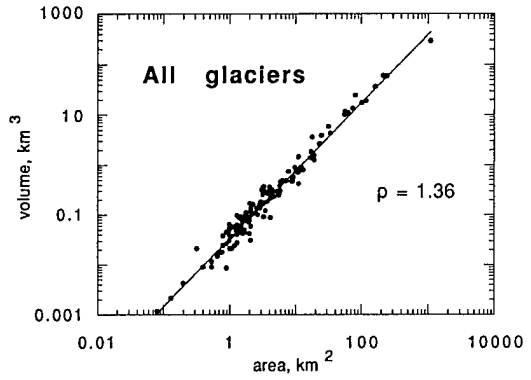

Figure 6. Composite plot of volume versus area for all 144 mountain glaciers shown in Figure 5.

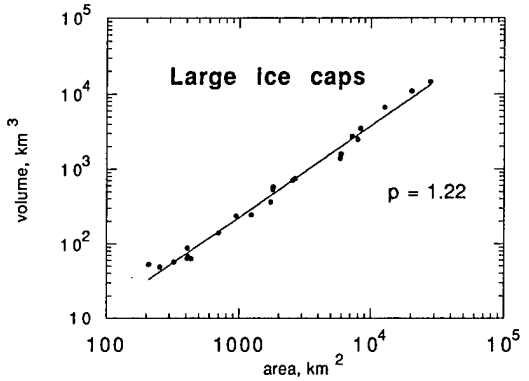

Figure 7. Plot of volume versus area for ice caps larger than 200 km^2.

Table 1. Numbers, areas, and volumes of glaciers and ice caps of the world.

	Ice caps	*Glaciers*	*Total*
Number ($\times 10^3$)	0.07	160	160
Area ($\times 10^3$ km^2)	240	430	680
Volume ($\times 10^3$ km^3)	100	80	180
Sea-level equivalent (m)	0.27	0.24	0.50

inclusion here of ice caps and glaciers bordering the Greenland and Antarctic ice sheets.

LITERATURE CITED

Bahr, D. B., M. F. Meier and S. Peckham (in press) The physical basis of glacier volume-area scaling, mass balance distributions and sea level predictions.

Chen, J. and A. Ohmura (1990) Estimation of alpine glacier water resources and their change since the 1970's. In *Hydrology in Mountainous Regions. I. Hydrological Measurements; the Water Cycle.* IAHS Publ. No. 193, p. 127–135.

IAHS[ICSI]-UNEP-UNESCO (1989) World Glacier Inventory, Status 1988. Paris: IAHS Press, UNEP, UNESCO, 290 p.

Jóhannesson, T., C. Raymond and E. Waddington (1989) Time scale for adjustment of glaciers to changes in mass balance. *Journal of Glaciology,* **35:** 355–369.

Macheret, Yu.Ya., P.A. Cherkasov and L.I. Bobrova (1988) Tolschina i ob'em lednikov Djungarskogo Alatau po danniy aeroradiozondirovaniya. *Materialy Glyatsiologicheskikh Issledovaniy. Khronika. Obsuzhdeniya,* **51:** 49–62.

Meier, M.F. (1984) Contribution of small glaciers to global sea level. *Science,* **226:** 1418–1421.

Meier, M.F. (1993) Ice, climate, and sea level; do we know what is happening? In *Ice in the Climate System* (W. R. Peltier, Ed). NATO ASI Series I 12. Berlin Heidelberg: Springer-Verlag, p. 141–160.

Paterson, W. S. B. (1972) Laurentide Ice Sheet: estimated volumes during late Wisconsin. *Reviews of Geophysics and Space Physics,* **10:** 885–917.

Shook, K., D. M. Gray and J.W. Pomeroy (1993) Temporal variation in snowcover area during melt in prairie and alpine environments. *Nordic Hydrology,* **24:** 183–198.

Stauffer, D. and A. Aharony (1991) *Introduction to Percolation Theory,* Second Edition. London: Taylor and Francis, 181 p.

Warrick, R.A. and J. Oerlemans (1990) Sea Level Rise. In *Climate Change, the IPCC Assessment* (J.T. Houghton, G.J. Jenkins and J.J. Ephraums, Eds.). Cambridge: Cambridge University Press, p. 257–281.

Warrick, R.A., C. LeProvost, M.F. Meier, J. Oerlemans and P.L. Woodworth (in press) Changes in Sea Level. In *Second Assessment Report of the Intergovernmental Panel on Climate Change—Contribution of Working Group I* (J.T. Houghton, L.G. Meira Filho, B.A. Callander, N. Harris, A. Kattenberg, and K. Maskell, Eds.) Cambridge: Cambridge University Press.

Zhurovlyev, A.B. (1985) Korrelyatsionniy metod ozenky zapasov l'da v lednikakh. *Materialy Glyatsiologicheskikh Issledovaniy. Khronika. Obsuzhdeniya,* **52:** 241–249.

The Geometry and Stratigraphy of Siple Dome and Implications for its History

N. A. NERESON, C.F. RAYMOND
Geophysics Program, Box 351650, University of Washington, Seattle, WA, 98195

ABSTRACT

The geometry and internal stratigraphy of Siple Dome were investigated using GPS surveying and radio-echo sounding as part of a collaborative project involving the University of Washington, St. Olaf College, and the University of Colorado. Because of its location between Ice Streams C and D, the evolution of Siple Dome through the last glacial maximum to present is closely related to possible changes in the dynamics of these ice streams and larger scale changes of the West Antarctic Ice Sheet along the Siple Coast. The measurements show that, in the vicinity of its summit, Siple Dome is essentially a two-dimensional ridge overlying relatively flat bedrock. Internal layers were detected throughout most of the ice thickness and were continuous over the width of the dome. Under the divide, these layers are warped convex up over a width of about four times the ice thickness of 1 km.

Siple Dome geometry, surface temperature, and accumulation rate were input to a time-independent, two-dimensional finite element model to predict the shapes of the upper surface and internal layers that would be expected under steady-state flow conditions. According to this model, the geometry of Siple Dome's upper surface and internal layers are broadly consistent with steady-state, given the uncertainties in spatial variations of accumulation rate and model simplifications. This result suggests that Siple Dome has been relatively stable for about 10^4 a or longer. However, a 60° deviation from vertical of the axis of the subdivide layer upwarping and other details of internal layer shapes are inconsistent with model predictions, indicating some non-steady-state effects associated with changes in accumulation, the dynamics of the surrounding ice streams, or a combination of these.

A simple two-dimensional kinematic model is used to investigate the effects of divide migration and spatial accumulation rate variations on the shapes of isochron layers in the ice. These effects individually, as well as their combined effects on layer shapes, are quantified and compared to the observed layers. Possible scenarios of divide migration and accumulation rate histories, which explain features of the observed layer geometry, are presented and discussed. A migration of the divide northward away from Ice Stream C toward Ice Stream D of 0.2–0.3 km over the past 10^3 a is strongly indicated by the layer shapes.

Constraints on the Velocity of Ice Streams Imposed by their Widths

C. F. RAYMOND
Geophysics Program, Box 351650, University of Washington
Seattle, WA 98195
ph. 206-543-4914; e-mail: charlie(Ggeophys .washington .edu)

ABSTRACT

The finite width of an ice stream places constraints on the velocity that it can have. I consider an ice stream of given thickness H, slope and corresponding driving stress T. I let U_d represent the standard deformational velocity that would be produced by shearing over H associated with the action of T, assuming Glen's Flow Law for ice with power $n(= 3)$. I let w be the half-width of the ice stream in units of H, which for Siple Coast ice streams lies in the range 10^1 to 10^2. I let u be the ice stream velocity in units of U_d. Then, allowing that conditions at the base of an ice stream would fall between no slip and free slip, u would lie in the range $[1, w^{n+1}]$. In the low part of this range, ice is supported by shear stress at the base. In the high part of the range, support is from the sides with no basal shear stress, like an ice shelf. This very large range in u spanning many orders of magnitude can be narrowed from both above and below in light of hydrological conditions necessary for the fast motion and by consideration of the energy dissipated at the bed by the combination of basal slip and shear stress. The energy dissipation on the bed has been quantified by modeling the flow in the cross section and shows the following properties: low at low velocity (because basal velocity is low), low at high velocity (because basal shear stress is low), and relatively high at intermediate velocity (because neither basal velocity or shear stress are low). If geothermal heat and conduction of heat in the ice cause a negative conductive heat balance at the bed (as at UpB) and a condition for fast motion is net melting at the base (a plausible expectation, since suction of water into an area of freeze-on could drop water pressure and suppress basal motion), then the basal heat generation must exceed a threshold value, and the possible range of u is significantly narrowed. A related implication is that, for a given conductive heat loss at the bed, there is a minimum w that would allow basal melting and fast flow. If it is assumed that the ice stream reaches a velocity that maximizes the melt rate at the base, then a unique velocity is predicted. For a linear relation between basal slip and shear stress and $n = 3$, it is $u = 0.4w^4$ and corresponds to conditions of roughly equal support from the base and sides. Although there are uncertainties in T and thus U_d that complicate comparison of available observations with this prediction, and the prediction does not account for strain softening at ice stream margins that has been inferred from several sets of observations, it appears that $u \leq 0.4w^4$ on Siple Coast ice streams with measured speeds. Speeds less than $0.4w^4$ suggest that velocity is limited by an efficient drainage system rather than dynamic feedback from the sides that reduces basal shear stress and limits basal melting.

Triggering of Eruptions by Release of Overburden Pressure: Theory and Application to Subglacial Volcanoes

FREYSTEINN SIGMUNDSSON
Nordic Volcanological Institute,
Reykjavik, Iceland; ph. +354 525 4494; e-mail: fs@norvol.hi.is

ABSTRACT

Eruptions or dike injections from magma chambers occur when the criterion $p_l + p_e = \sigma_3 + T$ is fulfilled, where p_e is magma pressure in excess of lithostatic pressure p_l, σ_3 is the minimum compressive stress, and T is the tensile strength of the crust (1–6 MPa in Iceland). Excess pressure in a magma chamber, or tectonic stress, causes tensile stress on the chamber margin, σ_T, which lowers the compressive stress from the lithostatic value. The eruption criteria can be written $p_e = \sigma_T + T$. If overburden pressure is released, the magma chamber effectively moves closer to the surface of the earth, carrying with it the same excess pressure. Interaction of the stress field with the free surface causes amplification of the tensile stress on the chamber margins, which depends on the shape of the chamber, and on the aspect ratio R/H, where R is the horizontal radius of a magma chamber roof, and H is its thickness. If $R/H < 1$, the Mogi model is applicable, and the chamber can be modeled as a spherical volume in an elastic halfspace. For this case the release of overburden pressure causes a minor change in σ_T, and is unlikely to trigger eruptions. If $R/H > 1$, the chamber roof can be modeled using plate theory. A change in overburden pressure Δp leads to $0.75(R/H)^2\Delta p$ maximum change in tensile stress in the chamber roof. Some eruptions of the subglacial Grimsvotn volcano, Iceland, have been preceded by outburst floods, releasing overburden pressure by about 1 MPa. If $R/H > 1$ at Grimsvotn, such pressure changes lead to change in tensile stress of similar magnitude or greater, and are therefore able to trigger eruptions if the chamber is close to failure. Seismic undershooting of the subglacial Katla volcano, Iceland, has revealed an aspect ratio $R/H > 1.25$. For such volcanoes, gradual changes in ice thickness may perturb eruption history. A 10-m gradual ice thinning would cause a less than 0.1 MPa increase in tensional stress, may advance a forthcoming eruption, and cause it to be of reduced vigor. Such thinning may have occurred in the first half of this century at Katla, possibly facilitating a low-vigor eruption there in 1955.

Greenland Climate Network: GC-Net

CONRAD STEFFEN, JASON BOX, WALEED ABDALATI

Cooperative Institute for Environmental Sciences, University of Colorado
Campus Box 216, Boulder, CO 80309-0216
lsoni@jpseaice.colorado .edu

INTRODUCTION

The Greenland ice sheet plays a pivotal role in global climate, primarily because of its high reflectivity, high elevation (i.e., as a topographic barrier) and large area, but also because of the substantial volume of fresh water stored in the ice mass. Greenland ice sheet mass balance may exert significant control over sea level rise. Snow accumulation is a critical parameter for determining ice sheet mass balance, but little is known of the regional differences in accumulation over the Greenland ice sheet. A comprehensive assessment of the spatial and temporal variability of accumulation is needed.

Greenland precipitation studies done by Ohmura and Reeh (1991) show that winter contributions to the ice mass of Greenland have their source in cyclonic activity over Baffin Bay, to the west, and Iceland, to the east. In summer a large ridge of high pressure from the northeast to the central region of the ice sheet tends to reduce precipitation. Ohmura and Reeh cite orographic uplift of air from the west and southeast as a cause of higher accumulation in the coastal northwestern region. Recent precipitation trends over the Greenland ice sheet, based on atmospheric analysis, were reported by Bromwich and Robasky (1993). They found a decrease in precipitation since 1963, with a secondary increase over the southern part of the ice sheet starting in 1977. This nonuniform spatial and temporal nature of precipitation over the ice sheet indicates that changes in ice sheet mass balance result from regional interactions requiring studies over a larger sample of sites.

Climatological observations and surface energy balance studies are the keys to the understanding of the surface processes linked with ice sheet mass balance. Long-term climate records at different sites on the ice sheet are needed for the assessment of the snowpack energy and mass balance of the accumulation zone and to gain more complete information on the spatial variation of climate over the ice sheet. A considerable amount of surface energy and mass balance data, as well as some ice cores, have been collected at the ETH/CU research camp since 1990. The camp is located at the ice sheet Equilibrium Line Altitude (ELA), about 89 km east of Jakobshavn at 69°34'N, 49°17'W on the western margin of the Greenland ice sheet (Fig. 1). Six years of detailed climatological and glaciological measurements at the camp provide valuable insight on the magnitude of the seasonal and interannual variability in the equilibrium zone.

On the basis of ETH/CU camp energy flux measurements, a simple climate sensitivity model calculation showed that, during a 3°C temperature increase scenario, approximately 22 km^3 water equivalent of snow would sublimate (Steffen, in press). This equals 4% of today's annual accumulation. Large seasonal and interannual variations in air temperature and wind speed were found for the location of the ETH/CU camp from the 6-year record. Surface temperature anomalies in the order of –3°C along the west coast of Greenland for the winter months have also been reported since 1990 (Halpert et al. 1993). In contrast, a notable increasing trend of 4.5% per year in melt area has been observed between the years 1979 and 1991, which came to an abrupt halt in 1992 after the eruption of Mt. Pinatubo. A similar trend is observed in the temperatures at six coastal stations. The relationship between the warming trend and the increasing melting trend between 1979 and 1991 suggests that a 1°C temperature rise corresponds to an increase in melt area of 85,000 km^2 (Abdalati and Steffen, submitted).

Additional climatological and glaciological information will become available from three NASA-funded Automatic Weather Stations (AWS), which were installed during the 1995 field season along the 2000-m contour line of the western slope of the ice sheet, and one NSF-funded AWS in the northwestern part of the ice. The

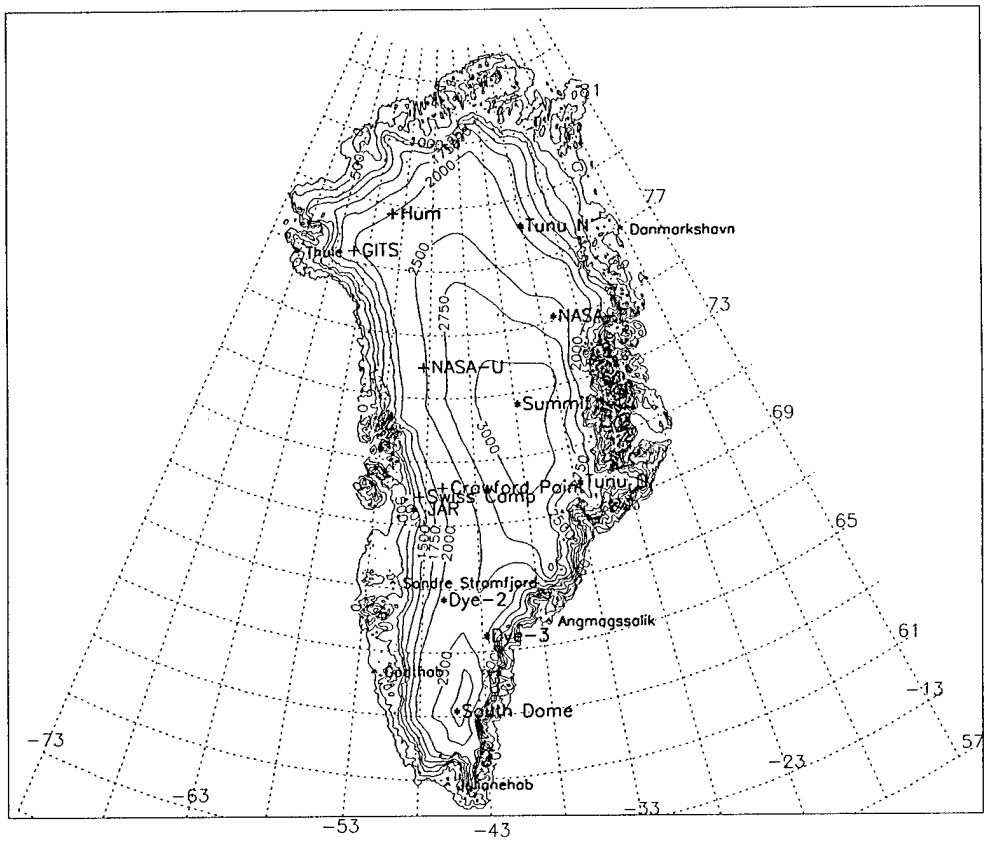

*Figure 1. Existing and proposed climate network stations on the Greenland ice sheet (+ = existing AWS stations, * = proposed AWS stations for 1996–98).*

Greenland Climate Network (GC-Net) is part of the Program for Arctic Regional Climate Assessment (PARCA), a NASA polar initiative with the prime goal of measuring and understanding the mass balance of the Greenland ice sheet.

CURRENT CLIMATE STATION NETWORK

Only a few years of climatological measurements are available from automatic weather stations, mainly from the Summit area for the period 1992–95 (Stearns et al. 1994), and from the Jakobshavn area at the ELA for 1990–present (Steffen, in press). Four additional AWS were installed along the western and northwestern slope of the ice sheet during the 1995 field season (Table 1, Fig. 1). Four of the existing AWS (excluding ETH/CU camp) are transmitting a total of 66 climate and snow parameters hourly via satellite link. The transmission success rate has been 92% as of 15 December 1995. More information on instrument setup and measured parameters can be accessed via the world wide web http://cires.colorado.edu/parca.htrnl. This mosaic page will also enable users to download the AWS data via FTP. Data processing programs have been written to check the quality of the data and to eliminate data outliers.

METHOD

Each instrument tower is equipped with a number of meteorological and glaciologcal instruments (Fig. 2) to measure the following parameters: 1) the accumulation rate at high temporal resolution to identify and resolve individual storms; 2) the radiation balance at the surface; 3) temperature, humidity and wind speed profiles in the air; and 4) the conductive heat flux that also describes the energy dissipation in the snow pack (i.e., from refreezing of melt water). Additional meteorological parameters such as wind direction, pressure,

Table 1. Automatic Weather Station (ASW) network on the Greenland ice sheet as of summer 1995 (existing) and proposed AWS locations for 1996.

	Funding	*Name*	*Latitude*	*Longitude*	*Elevation*
Existing 1995	NASA	ETH/CU Camp	69°34′N	49°18′W	1147
	NASA	Crawford Point	69°51′N	47°07′W	2000
	NASA	NASA-U	73°51′N	49°30′W	2400
	NASA	GITS	77°11′N	61°W	1850
	NSF	Humboldt Site	78°35′N	57°13′W	1985
Proposed 1996	NSF	Tunu-North	78°N	32°W	2000
	NASA	Summit	72°30′N	38°12′W	3220
	NASA	NASA-East	75°N	32°W	2400
	NASA	JAR	69°18′N	49°30′W	650

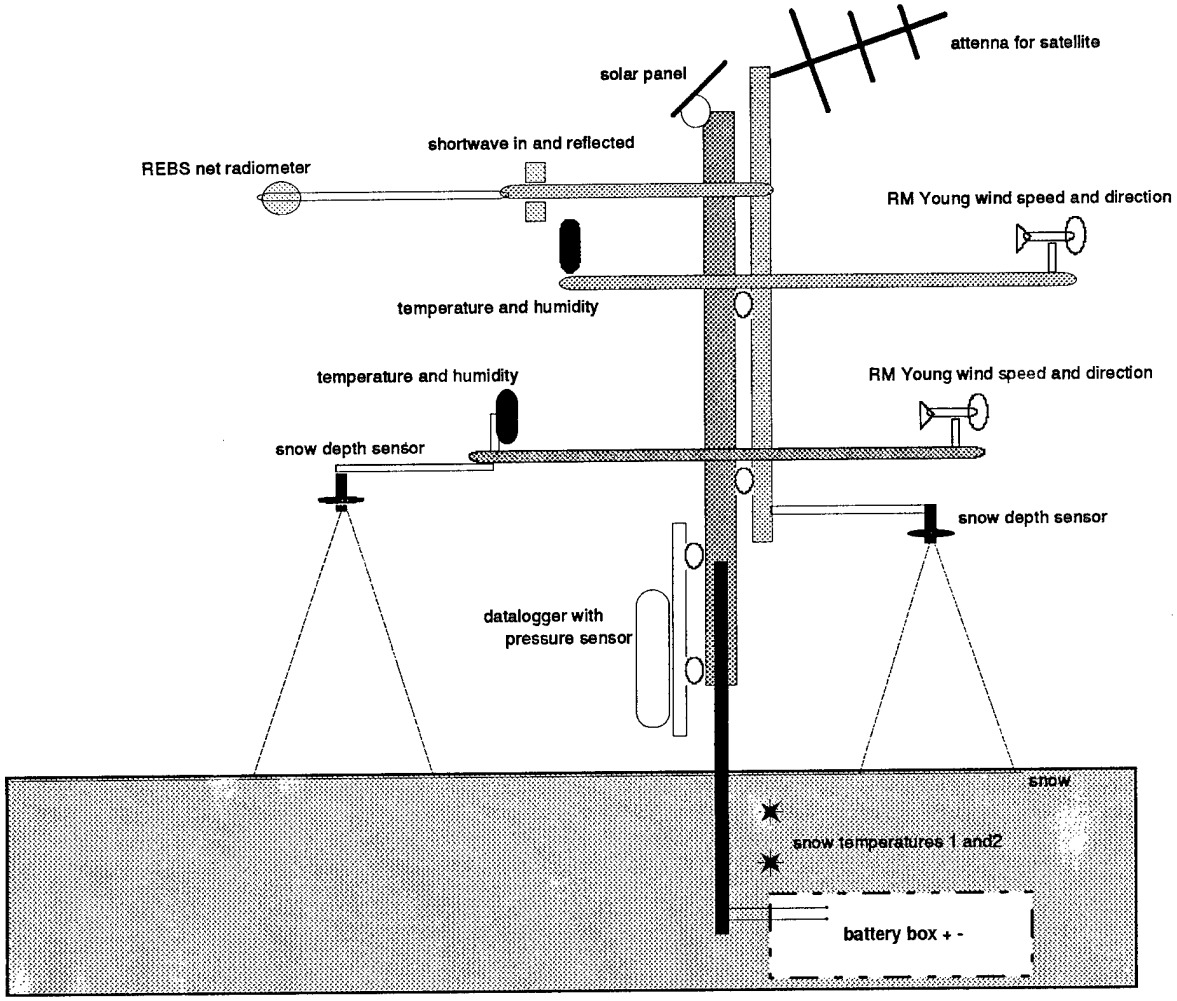

Figure 2. Automatic Weather Station (AWS) with acoustic snow depth sensors and satellite link antenna. The batteries (4 × 100 Ah) will be buried in the snow in a waterproof wooden box. The snow thermocouples will be inserted in a shallow ice core hole to monitor the firn temperatures for the first 10 m.

and short-wave incoming and reflected radiation area also recorded.

The radiation is sampled at 20-second intervals and averaged over 60 minutes. All the other parameters are sampled every 10 minutes and averaged over 60 minutes (Table 2). The data are transmitted via a satellite link (GOES for station location south of 72°N or ARGOS) each hour throughout the year. In addition, all the measurements will be stored in a two-Mb solid state memory device, which can store 36 months of continuous measurements for up to 10 years. The data logger is powered from two 100-Ah batteries, which will be charged from a 20-W solar panel. The satellite link will be powered from two separate 100-Ah batteries connected to a 20-W solar panel. This setup guarantees continuous data recordings and storage, even in the unlikely case of satellite transmission failure.

The mass balance and climate recording stations on the Greenland ice sheet fulfill the following objectives:

1. Assess daily, annual and interannual variability in accumulation rate, surface climatology and surface energy balance at a few locations on the ice sheet where high sensitivity of the ice sheet mass balance to climate anomalies is predicted from modeling results.

2. Assess accurate surface elevation, location, and near-surface density at the AWS location with the option to revisit the locations to get temporal information for dynamic ice sheet modeling.

3. Determine long-term mass balance of the ice sheet and surface climatology from firn and ice cores, and from satellite and aircraft measurements, using automatic recording sites and in-situ studies to calibrate and validate the remote sensing algorithms.

Table 2. Sensor sampling and recording intervals for the ASW on the Greenland ice sheet. The expected lifetime of the instrumentation is approximately 5 years.

Parameter	*Number of sensors*	*Sampling interval/ recording interval*
Air temperature	2	10 min/1 h
Snow temperature	10	10 min/1 h
Wind speed	2	10 min/1 h
Humidity	2	10 min/1 h
Wind direction	2	10 min/1 h
Pressure	1	10 min/1 h
Nat radiation	1	60 s/1 h
Short-wave incoming and reflected radiation	2	60 s/1 h
Acoustic snow depth	2	10 min/1 h

RESULTS

The first 7 months of snow height recordings at the four AWS sites (for location see Fig. 1) reveal quite a variability in snow accumulation along the western slope of the Greenland ice sheet (Fig. 3). The two stations—Crawford and NASA-U—situated between 70–74°N show a similar accumulation rate during the cold months of October through December. It is interesting that the two sites have such a similar accumulation rate, given the fact that they are roughly 450 km apart and that NASA-U is at an elevation of 2400 m, compared to 2000 m for the Crawford site.

Some snow surface lowering of 0.16 m occurred in July at the Crawford site, which can be attributed to snow compacting, snow sublimation, and possibly some melt. Accumulation rates for the two northern sites are markedly different, even though they are only 100 km apart. GITS along the western slope of the ice sheet has a high accumulation rate because of the up-slope effect of the Baffin Bay cyclone, which dominates that region. This area is also known to have the highest an-

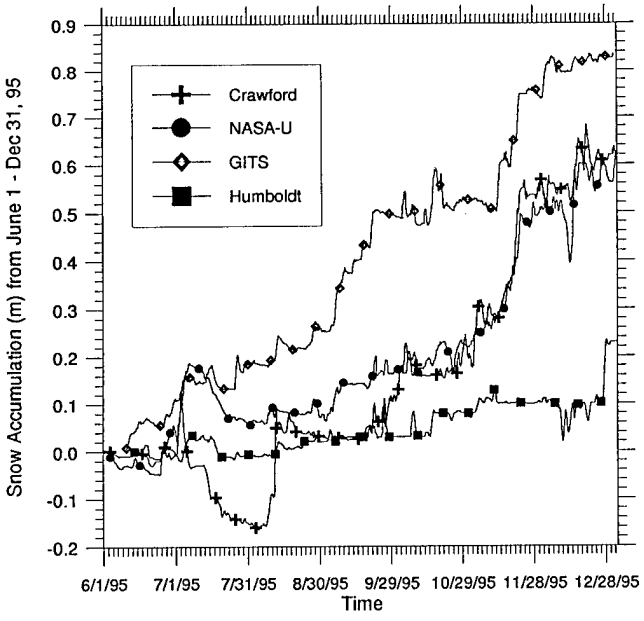

Figure 3. Surface snow accumulation at four AWS sites along the western and northwestern slope of the Greenland ice sheet. For AWS site locations see Figure 1.

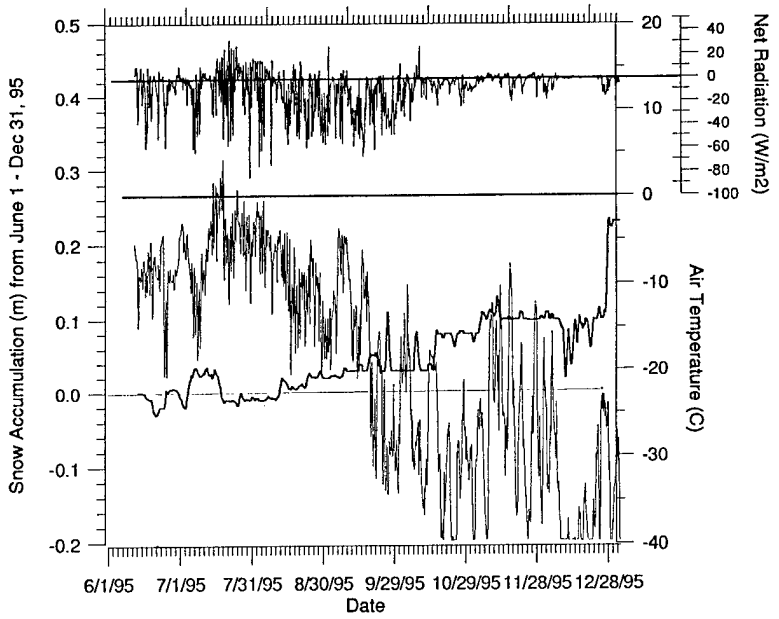

a. Humboldt AWS site for 1 June–31 December 1995. Upper graph shows net radiation with a mean value of –9.0 W m.$^{-2}$ over the 7-month period. The air temperature (thin line) has a mean value of –21.2°C, and the surface elevation change for the same period was 0.2 m (accumulation of snow sublimation). The mean relative humidity was 75% with an average wind speed of 5.8 m s^{-1} (not shown in this figure).

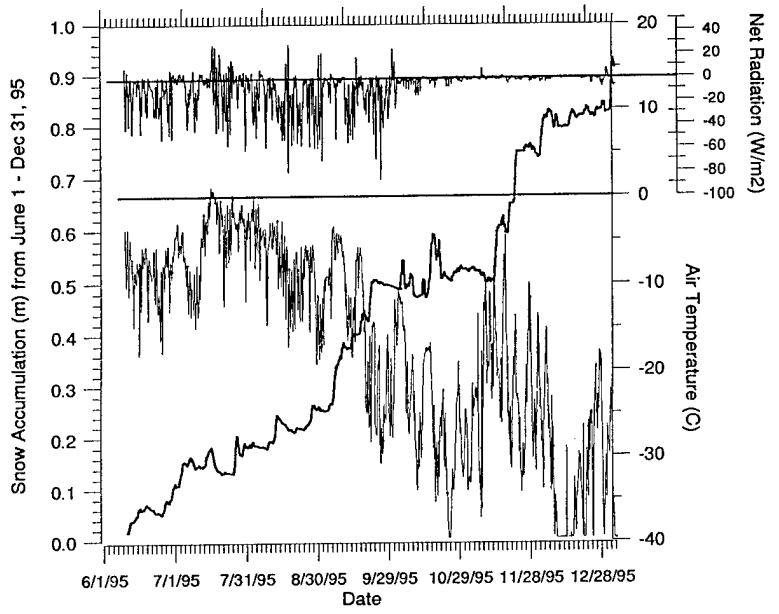

b. GITS AWS site for 1 June–31 December 1995. Upper graph shows net radiation with a mean value of –9.1 W m^{-2} over the 7-month period. The air temperature (thin line) has a mean value of –17.2°C, and the surface elevation change for the same time period was 0.9 m (accumulation of snow sublimation). The mean relative humidity was 77% with an average wind speed of 5.6 m s^{-1} (not shown in this figure).

Figure 4. Surface climatology.

nual accumulation for northern Greenland, exceeding 60 cm water equivalent yearly according to Ohmura and Reeh (1991). The Baffin Bay moisture flux does not reach the Humboldt site in the northwest, as the cyclone path usually does not go that far north, and, consequently, the Humboldt site has a much reduced accumulation rate. Recent ice core analysis from the Humboldt site revealed a mean annual accumulation of roughly 17 cm water equivalent over the past 60 years (R. Bales, personal communication).

The surface climatologies for the Humboldt site and the GITS site are quite similar (Fig. 4). Both locations have a predominantly negative net radiation balance during the summer months, with values between –40 to –60 W m^{-2} under clear sky conditions. The radiation balance was only slightly positive (10 W m^{-2}) during a 1-week period in July, when the air temperature rose above 0°C. Sky radiation and longwave emission from the snow surface were of equal magnitude in the absence of solar radiation during the months November and December. The mean value over the 7-month period was –9 W m^{-2}. Both air temperature records are highly correlated, and show a general cooling trend from summer to winter, with variations as large as 30°C. These temperature fluctuations are caused by strong catabatic winds, as a result of turbulent mixing of energy from the temperature inversion to the surface.

ACKNOWLEDGMENTS

This research was supported by NASA Polar Program grant NAWG-2158, and by the National Science Foundation, Office of Polar Program grant OPP-0423530.

LITERATURE CITED

Abdalati, W. and K. Steffen (submitted) Snow melt on the Greenland ice sheet as derived from passive microwave satellite data, *J. Climate.*

Bromwich, D.H. and F.M. Robasky (1993) Recent precipitation trends over the polar ice sheets. *Meteoroid Atmos. Phys.*, **51:** 259–274.

Halpert, M.S., G.D. Bell, V.E. Kousky and C.F. Ropelewski (1993) Climate Assessment 1993. U.S. Dept. Of Commerce, National Weather Service, National Meteorological Center.

Ohmura, A. and N. Reeh (1991) New precipitation and accumulation maps for Greenland. *Journal of Glaciology,* **37**(125): 140–148.

Stearns, J., M. Seefeldt and G.A. Weidner (1994) Greenland Field Report: 1994 Field Season. Madison: University of Wisconsin, Space Science and Engineering Center, p. 12.

Steffen, K. (in press) Surface energy exchange at the equilibrium line on the Greenland ice sheet during onset of melt. *Annals of Glaciology,* **21.**

Regional and Local Influences on Borehole Measurements of Subglacial Water Pressure

D. B. STONE
INSTAAR, University of Colorado, Boulder, CO 80309; 303-492-5800
e-mail: dstone@spot.colorado.edu

J. KOEHLER
Dept. of Applied Mathematics, University of Colorado at Denver
Denver, CO 80217; 303-556-4805

ABSTRACT

Hot-water drilling permits direct access to the glacier bed, and is now a widely used technique in studies of subglacial processes. Because basal water pressure affects both sliding and the deformation of subglacial debris, boreholes connected to the subglacial water system are often instrumented to measure fluctuations in the borehole water column. Simultaneous measurements at different locations sometimes show similar variations of water level, indicating that the boreholes involved are connected to a common part of the basal water system. In this situation, the generally uniform excursions indicate a widespread response to forcings originating further up-glacier, so called "regional" influences. On a more detailed scale, however, frequent deviations from the general trend and discrepancies between individual pressure records can be discerned. Irregular, small-amplitude fluctuations, which differ from borehole to borehole, likely reflect "local" influences on water pressure, such as input from an englacial conduit intersecting the borehole or changes in cavity volume at the borehole base. We are using statistical models and time-series methods, including spectral analysis and lagged correlations, to separate regional and local influences on borehole pressure records. We describe how isolating these components enables a more detailed examination of physical phenomena that not only give rise to the observed pressure variations, but contribute to basal water system dynamics.

A Maximum Resolution Glacier-Bed Surface Obtained by Radio-Echo Sounding

BRIAN C. WELCH, W. TAD PFEFFER
INSTAAR, University of Colorado, Boulder, CO 80309

JOEL T. HARPER, NEIL F. HUMPHREY
Dept. of Geology and Geophysics, University of Wyoming, Laramie, WY 82071

ABSTRACT

A 5-MHz radio echo sounding system was used to accurately map a portion of the bed topography of the Worthington Glacier, Alaska. The array of longitudinal profiles was resampled to create cross-glacier profiles to constrain the echo source direction along the profiles. Conventional seismic processing routines, including two-dimensional phase-shift migration, were applied to the profiles. A three-dimensional topography of the glacier bed was created using the constraints of the horizontal and vertical resolution of the field equipment. The bed topography of the glacier, as mapped by radar, closely resembles the surface topography above. Ice thicknesses measured by the radar agree with depths determined in boreholes drilled through the ice.

INTRODUCTION

Radio-echo sounding has been a common technique used to determine temperate glacier depth and bed topography since the 1970s (Watts et al. 1975). Frequencies around 5 MHz are sufficient to yield strong bed returns for temperate glaciers.

The Worthington Glacier Project is a multi-year effort to directly measure the deformation of ice by means of a borehole network (Pfeffer et al. 1994). An accurate bed topography is needed to interpret the deformation results. While many studies have produced maps of glacier and ice sheet beds, most have interpolated between radar profiles spaced beyond the resolution of the equipment (Björnsson 1981, 1988; Brown et al. 1986). The Worthington Project radar array was established to maximize the resolution of the mapped bed surface using a relatively inexpensive radar system.

The Worthington Glacier is a temperate valley glacier in the Chugach Mountains of Alaska. It is approximately 7 km long and as much as 1.5 km wide. The broad accumulation ends at the bottom of an ice fall. Below these falls, the glacier flattens out into a Lower Bench, with a low rise running along the center axis (Fig. 1). The Worthington Glacier Project is located on this bench. Below the bench the glacier steepens sharply and is split into two termini by a bedrock ridge.

INSTRUMENTATION

The radar configuration used is similar to that described by Narod and Clarke (1994). The transmitter has a frequency of 50 MHz. Two 10-m dipole antennas give a center frequency of 5 MHz (center wavelength of 33.8 m in ice). The vertical resolution of the field equipment is 7.8 m, or $^1/_4$ times the center wavelength (Yilmaz 1987). Horizontal resolution of unmigrated profiles decreases with increasing ice thickness. Migrated sections can resolve features with a radius roughly equal to the 33.8-m center wavelength of the radar equipment (Yilmaz 1987).

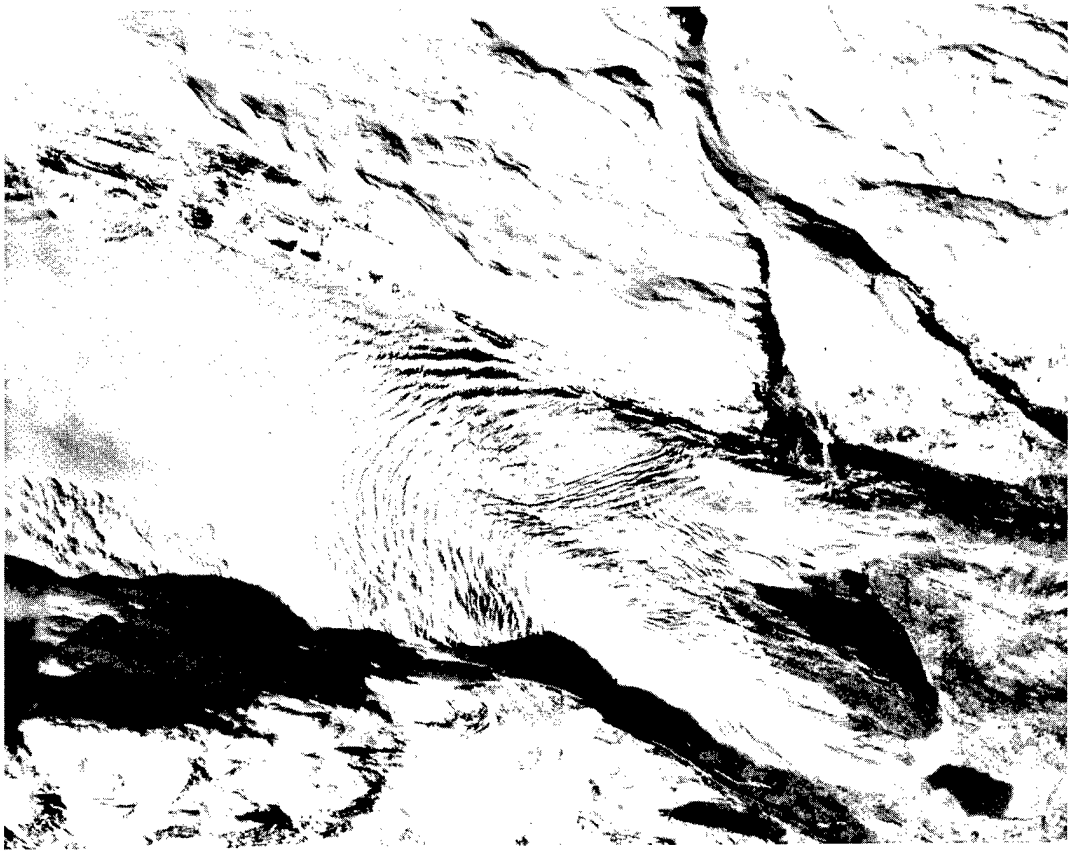

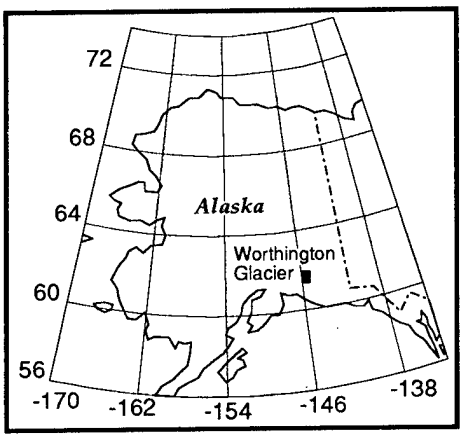

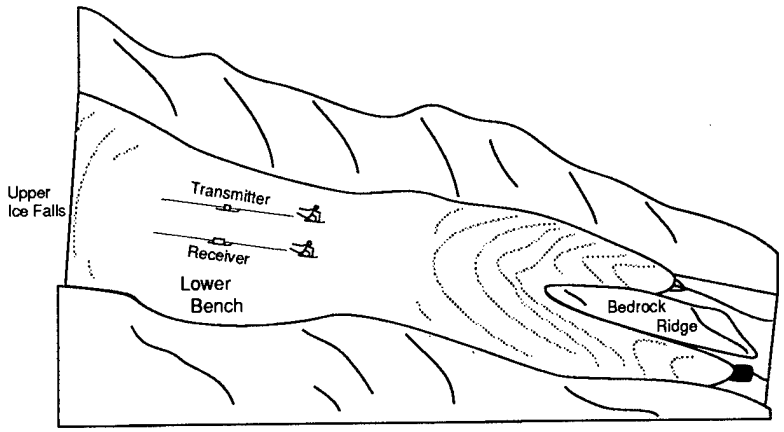

Figure 1. Worthington Glacier. Cartoon showing the configuration of radio-echo sounding equipment (bottom right). The receiver and transmitter were in the center of 10-m antennas. They were towed parallel to one another with a 30-m separation. 1993 air photo of the lower bench and lower ice falls (top). Note the bedrock ridge that splits the glacier terminus into two tongues.

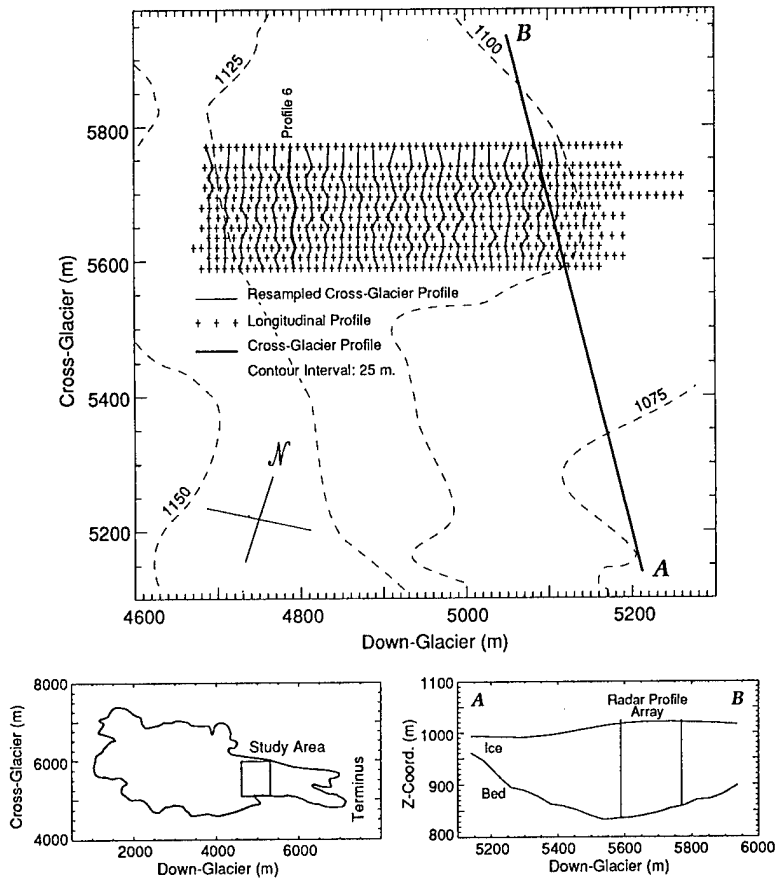

Figure 2. Array of radar profiles on the Worthington Glacier. Longitudinal profiles were resampled to create cross-glacier profiles (Glacier map from Case 1958). Profile AB was recorded as a cross-glacier profile.

The transmitter sits on a sled between the two 10-m antennas and is pulled by two skiers in a direction coaxial to the antennas (Fig. 1). The receiver sits between two 10-m antennas oriented parallel to the transmitter antennas. The signals are received by a Fluke voltmeter–oscilloscope and recorded on a PC-compatible laptop computer. The instruments are mounted on a sled and towed by means of a rope attached to the front antenna. Both the transmitter and receiver sleds are pulled by researchers on skis.

The radar instruments were dragged along profiles parallel to the longitudinal glacier axis, with an antenna separation of approximately 30 m. The profile spacing was 15 m, except for the northernmost profile, which was 30 m from the rest of the array. Traces were recorded every 10 m along the profiles. A total of 12 profiles was recorded over the summer of 1994 (Fig. 2). A single cross-glacier profile was also recorded (AB in Fig. 2) with a trace spacing of roughly 40 m.

Examination of the land topography around the glacier indicates that there is a ridge of bedrock that extends from between the two termini through the study area roughly along the axis of the glacier (Fig. 1). Evidence of this center ridge can be seen in the ice topography in the study region as well as where it is exposed at the terminus. The local bedrock is predominantly mica-schist. Borehole video observations have shown that the majority of entrained debris is within 1 m of the bed (Harper and Humphrey 1995). Such a thin layer does not significantly affect the bed returns.

DATA PROCESSING

A single radar profile along the center of a glacier with a parabolic cross-section should record returns from the bed directly below the profile as well as from the valley walls. The addition of a

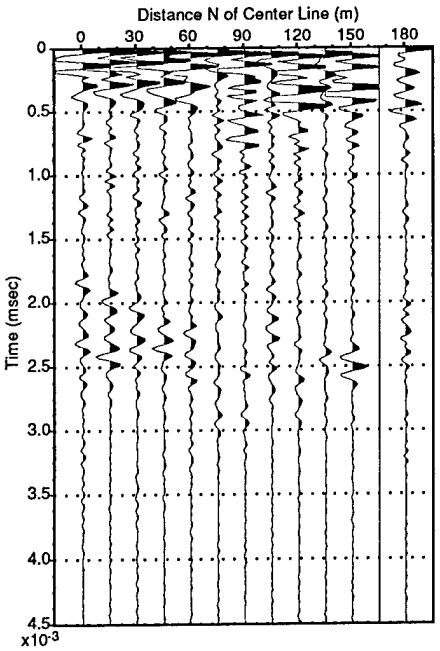

a. SeisUnix output of Profile 6 raw data after static corrections for elevation, ablation, ice movement and antenna separation.

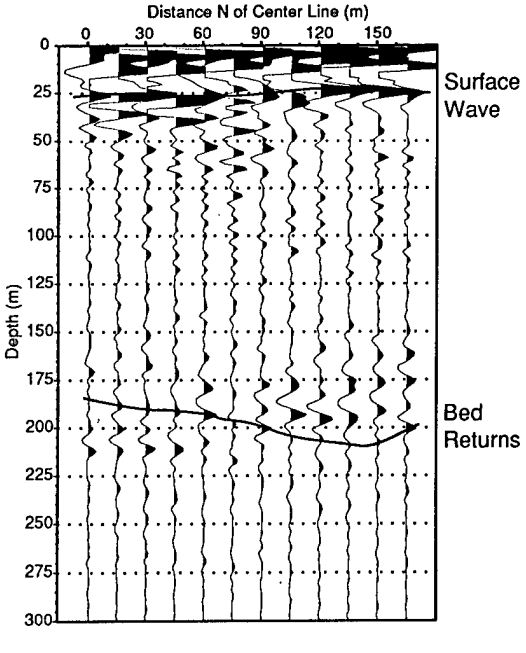

b. Two-dimensional phase-shift migration of Profile 6. Note the surface wave and bed returns. The bed return is chosen based on the adjacent profiles.

Figure 3. Profile 6.

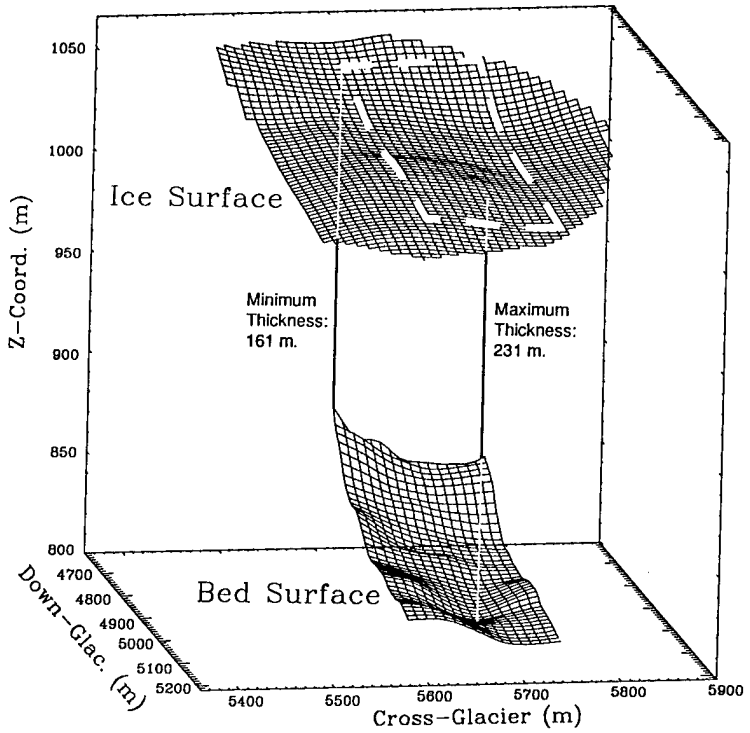

Figure 4. Three-dimensional surface plots of the bed and ice surface showing the location of minimum and maximum depths. The ice surface is interpolated from an optical survey during the summer of 1994.

ridge of bedrock as found in the Worthington Glacier adds more returns to the profile. A difficulty arises in determining the position of the reflector that produced the recorded return. Observations of the valley geometry indicate that the returns for a longitudinal profile come from reflectors located primarily to either side of the profile direction. However, to resolve the ambiguity of reflector location, the majority of the returns must be along the profile axis. Therefore, the array of longitudinal profiles was resampled to create an array of cross-glacier profiles.

Topographic, ablation, ice movement and antenna separation corrections were calculated for each profile (Fig. 3a). The profiles were then passed through a band pass digital filter of 7.5 to 22 MHz to remove background noise. Two-dimensional phase-shift (frequency-wavenumber) migration was applied to each profile to resolve the remaining multiple returns and to correct the slopes and positions of the reflector surfaces (Fig. 3b). The filtering and migration routines are part of a free seismic processing software package developed by the Colorado School of Mines, called SeisUnix. The software requires constant trace spacing, so a null trace was inserted between the two northernmost traces of each profile to create a constant 15-m spacing.

As SeisUnix was developed to process acoustic seismic data, some adjustments were made to accommodate radio-echo sounding data. The software expects all times to be measured in milliseconds rather than the nanoseconds recorded in radio-echo sounding. Adaptations were made to the processing code to accommodate the timing differences and to produce true depth sections.

By recording traces with the transmitter parallel to the receiver, the arrival of the surface wave was recorded. On the migrated section it appears at 30 m, which is representative of the antenna separation (Fig. 3b). The presence of an approximately constant surface wave arrival eliminates concerns of significant triggering errors.

RESULTS

The bed returns were picked by hand from each migrated profile. Adjacent profiles were used to minimize unreasonable changes in bed shape in the third dimension. Although the procedure is not true three-dimensional seismic processing, it represents a simple form of three-dimensional control on the profiles. The recorded bed returns were interpolated to create a rough surface plot (Fig. 4). The horizontal resolution of the radar equipment can resolve a feature with a radius of 33.8 m after the profiles have been migrated. A boxcar filter with a 68-m window was used to smooth any features that are too small to be resolved by the field equipment. Because of the much lower resolution in the horizontal plane, the boxcar filtering eliminated the need to smooth in the vertical direction.

The resulting surface closely resembles the ice topography above. The regions of steeper bed slope are covered with thinner ice, as would be expected from ice flow physics. The thinnest ice, 131 m, is located in the southwest corner. The flatter region where the borehole network is situated is thicker. A maximum ice thickness of 231 m was recorded near the west edge of the data set. The ice thicknesses as measured by the radar are confirmed to within a few meters by the borehole depths.

The center ridge of bedrock is apparently the slope seen along the south side of the radar surface. The profiles did not extend far enough across the glacier to record the entire ridge. The cross-glacier profile AB (Fig. 2) does not show evidence of the bedrock ridge. This profile was processed in the same manner as the resampled profiles. The trace spacing of 40 m is beyond even the resolution of the radar equipment. At best, this profile could only resolve a feature that is 80 m across. Therefore, the lack a bedrock ridge in this profile does not preclude its existence. It is also important to note that the slope of AB dips in the opposite direction from the surface slope mapped by the array of radar profiles. These discrepancies show that interpolating beyond the resolution of radar equipment can be misleading. While a minimal data set may yield bed surfaces that are generally correct, mapping of the bed surface to the maximum resolution of the radar equipment will produce an accurate map of the glacier bed features.

ACKNOWLEDGMENTS

This work was supported by NSF Grant no. OPP-9122916. Field work was aided by D. Bahr, K. Lewis, B. Raup and C. Stevenson. Assistance with data processing was provided by W. Clemment, J. Stockwell, Jr. and R. Jacobel. SeisUnix is currently available at http://timna.Mines.EDU/cwpcodes/ and runs on most workstation platforms.

LITERATURE CITED

Björnsson, H. (1988) Hydrology of ice caps in volcanic regions. *Societas Scientarum Islandica*, p. 30–40.

Björnsson, H. (1981) Radio-echo sounding maps of Storglaciären, Isfallsglaciären and Rabots Glacier, Northern Sweden. *Geografiska Annaler*, **63A**(3–4): 225–231.

Brown, C.S., L.A. Rasmussen and M.F. Meier (1986) Bed topography inferred from airborne radio-echo sounding of Columbia Glacier, Alaska. In Studies of Columbia Glacier, Alaska. USGS Professional Paper 1258-G.

Case, J. (1958) Worthington Glacier, Alaska; precise maps of certain North American glaciers. Amer. Geog. Soc., Special Publication No. 34.

Harper, J.T. and N.F. Humphrey (1995) Borehole video analysis of a temperate glacier's englacial and subglacial structures: Implications for glacier flow models. *Geology*, **23**(10): 901–904.

Narod, B.B. and G.F.C. Clarke (1994) Miniature high-power impulse transmitter for radio-echo sounding. *Journal of Glaciology*, **40**(134): 190–194.

Pfeffer, W.T., N.F. Humphrey, D.B. Bahr, J.T. Harper, B. Raup and B. Welch (1994) Observed velocity structure at depth in Worthington Glacier, Alaska [abs.], *Eos* (Transactions, American Geophysical Union), **75**: 222.

Watts, R.D., A.W. England, R.S. Vickers and M.F. Meier (1975) Radio-echo sounding on South Cascade Glacier, Washington, using a long-wavelength, mono-pulse source. *Journal of Glaciology*, **15**(73): 459–461.

Yilmaz, Ö. (1987) Seismic data processing. In *Investigations in Geophysics*, Vol. 2. Soc. of Exploration Geophysics, p. 250–260, 470–475.

Mapping of 10-m Firn Temperature in the Dry Snow Zones of Greenland and Antarctica Using the Scanning Multichannel Microwave Radiometer

DALE P. WINEBRENNER
Applied Physics Laboratory, University of Washington, Seattle, WA 98105
ph. 206-543-1393; e-mail: dpw@apl.washington.edu

ABSTRACT

Microwave emission at 4.5-cm wavelength from perennially dry polar firn is determined predominantly by the physical temperature at 10- to 30-m depths and the properties of centimeter-scale density layering in the upper 15 m of firn. Evidence for this comes from a ground-based study presented previously and from new comparisons of dual-polarized emission at 14 sites in Greenland and Antarctica, at which 10-m firn temperatures are known from direct measurement. Theory for the emission process and observations show that dual-polarization observations may be used to estimate an effective emissivity of polar firn (that is, the ratio of vertically polarized brightness temperature at 50° incidence angle to the 10-m firn temperature). Thus, dual-polarization observations may be used to infer 10-m firn temperatures in the dry snow zones of Greenland and Antarctica.

I present here a refined, extended comparison of observations made using the Scanning Multichannel Microwave Radiometer (SMMR) with electromagnetic emission theory for a randomly layered medium, taking into account the recent NASA Pathfinder processing improvements to the SMMR data set. The observations are consistent with the theory and show a linear relationship between the polarization ratio and the effective emissivity, to within scatter attributable to the instrument footprint size and uncertainties in some 10-m firn temperatures measured 10–15 years prior to the satellite observations. The scatter in the observed relationship suggests a measurement error of 1–3 K. I present maps of 10-m firn temperature estimates based on this relationship for the dry snow zones of both Greenland and Antarctica and compare them with earlier maps based on parameterizations with elevation and latitude. The satellite-derived maps are consistent with the earlier maps on scales of hundreds of kilometers, but indicate greater (nonrandom) structure in the temperature field, especially on the east Antarctic plateau.

A Retracking Algorithm for Satellite Radar Altimetry Over an Ice Sheet and its Applications

D. YI, C. R. BENTLEY
Geophysical and Polar Research Center, University of Wisconsin-Madison,
Madison, WI 53706

ABSTRACT

Both surface scattering and volume scattering contribute energy to satellite-radar-altimeter return waveforms over a continental ice sheet. Here, we present a retracking algorithm that includes surface scattering and volume scattering, and, for the first time, also includes the surface topography, the satellite pointing angle and the curvature of the earth in both the surface-scattering and volume-scattering models. Our algorithm can yield surface elevation values for individual waveforms. At the same time, quantitative estimates of the surface roughness and signal penetration and their regional and seasonal variations can be obtained. We have applied the algorithm to Geosat data over a section (69°S–72.1°S and 80°E–140°E) of East Antarctica. Generally, the spatial variation of the parameters is not a function of elevation, but is related to the drainage systems. Seasonal variations show clearly from 80°E to 95°E but are not very clear from 96°E to 140°E. We compare our results with those of previous retracking systems.

INTRODUCTION

Studying polar ice sheets is an important part of understanding global climate change and sea-level change. Because of the remoteness and vastness of the Antarctic ice sheet, its surface properties and dynamics are still poorly known. If algorithms for extracting the pertinent measurements from remotely sensed data can be developed, satellite-remote-sensing data can provide quick, accurate, and inexpensive information about the ice sheets.

Since the launch of the Seasat in 1978, great progress has been made in the application of satellite radar altimetry to the study of polar ice sheets. Satellite radar altimetry data have been used to map ice margins and grounding lines (Thomas et al. 1983, Partington et al. 1987, Zwally et al. 1987). Surface elevation maps acquired by radar altimeter can be used in long-term ice-sheet–mass-balance studies (Brooks et al. 1978, Zwally et al. 1989, Bentley and Sheehan 1992). However, the precision of current satellite altimetry data is not ideal for ice-sheet–mass-balance studies because the satellite radar altimeter was designed for ocean studies. The range detector on board the satellite can react quickly enough to track the small changes in the mean height of the ocean surface, but over a polar ice sheet, whose surface elevation varies laterally much more rapidly, it often loses track of the surface echo. Over the ice sheets, therefore, satellite radar altimeter measurements need to be "retracked"—that is, the original echo pulses must be reanalyzed to determine the time of flight of the echoes.

On the basis of a surface scattering model, NASA's Goddard Space Flight Center retracked all the Seasat and Geosat data over the Antarctic and Greenland ice sheets to an overall precision of about 1.6 m (Martin et al. 1983, Zwally et al. 1990). Ridley and Partington (1988) showed that volume scattering as well as surface scattering affects the waveform over Antarctica and that neglecting volume scattering can introduce an error in elevation as large as 3 m, depending on the retracking method and location. Davis and Moore (1993) introduced a retracking algorithm that includes a volume scattering term. The model they used yields an algorithm that fitted the waveform better than the NASA retracking algorithm (Davis and Moore 1993), but it still does not include the curvature of the earth or the effect of an off-nadir pointing angle. Yi and Bentley (1994) introduced an algorithm that includes the curvature of the earth and pointing angle in

the surface scattering model but not in the volume scattering model. Here, we introduce an algorithm that includes those factors in both the surface-scattering and volume-scattering models. Our algorithm can yield surface elevation values for individual waveforms. At the same time, quantitative estimates of the surface roughness, the proportion of volume scattering and penetration, and the regional and seasonal variations in those parameters can be obtained.

SURFACE BACK SCATTERING MODEL

The surface scattering model is given by (Yi and Bentley 1994)

$$p_s(\delta) = A'\left[1+\mathrm{erf}\left(\frac{\delta}{\sqrt{2\sigma_c}}\right)\right]/2 \qquad \delta < 0$$

$$p_s(\delta) = A'\exp(-\alpha\delta)I_0(\beta\delta^{1/2})\left[1+\mathrm{erf}\left(\frac{\delta}{\sqrt{2\sigma_c}}\right)\right]/2 \qquad \delta \geq 0.$$

This is a Brown model (Brown 1977) modified to include the earth curvature (Rodriguez 1988). α and β are coefficients related to the speed of light, satellite height, antenna beamwidth, and off-nadir pointing angle effect, A' will be eliminated during a normalization process, σ_c is related to surface roughness, and $\delta \equiv t - 2h/c$. (For more details see the paper by Yi and Bentley [1994].)

VOLUME-SCATTERING MODEL

To study of how penetration into the ice sheet affects the elevation measurement, we developed a volume-scattering model. The effect of the antenna pattern, surface roughness, earth curvature, surface slope, and satellite pointing angle are included in this model.

First, consider a one-dimensional model—a plane wave incident on a half-space. Let p_i be the incident power, p_{s0} the surface-scattered power, p_{t0} the transmitted power, R the reflection coefficient, and T the transmission coefficient. Then

$$p_{s0} = Rp_i$$

$$p_{t0} = Tp_i.$$

Since

$$T + R = 1$$

we have

$$p_{t0} = p_{s0}.$$

The energy from the satellite altimeter that penetrates the snow surface will be attenuated by the snow volume. The reduction in power density is defined by the equation (Davis and Moore 1993)

$$dp_t = -k_e p_{t0} dl$$

where dp_t is the incremental attenuation of the power p_t, l is the path length in snow, and k_e, which is assumed to be independent of depth, is the extinction coefficient in the snow. Integrating this equation and using the boundary condition $p_t = p_{t0}$ at $l = 0$, we have

$$p_t(l) = p_{t0}\exp(-k_e l).$$

The power scattered back from the depth increment l to $l + dl$ is

$$dp_b(l) = \sigma_v p_t(l) dl.$$

σ_v is the volume scattering coefficient. Let $p_{b'}(l)$ be the corresponding power when it arrives back at the snow surface, then

$$dp_{b'}(l) = \sigma_v p_{t0}(l)\exp(-k_e l) dl$$

i.e.

$$dp_{b'}(l) = \sigma_v p_{t0}(l)\exp(-2k_e l) dl.$$

After passing the surface the second time

$$dp_v(l) = \sigma_v T p_{t0}\exp(-2k_e l) dl$$

or, in terms of the surface-scattered power,

$$dp_v(l) = \sigma_v \frac{T^2}{R} p_{so}\exp(-2k_e l) dl.$$

$p_v(l)$ is the volume-scattered power.

At time t, the depth interval 0 to L contributes to the volume back scattering power; $L = 1/2c_s t$ is the snow depth at time t, above which volume scattering contributes to the received energy; and c_s is the speed of the light in snow. Because the incident angle within the AGC footprint is small

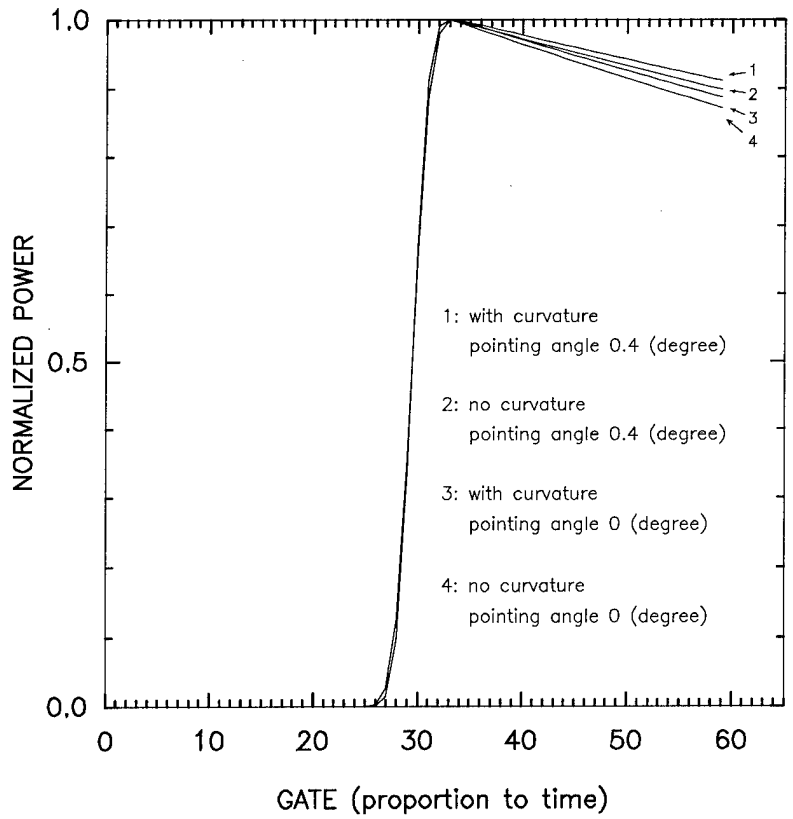

Figure 1. Normalized surface scattering waveforms showing the effect of the corrections for the Earth's curvature and the satellite pointing angle. The surface roughness is 0.5 m for all waveforms.

(< 0.5°), the variation in penetration depth over the range of the incident angles is small and can be ignored. By use of the above relations, the surface-scattering model can be introduced into the calculation of the volume-scattered power. The received volume-scattered power from a layer at depth l is

$$dp_v(t,l) = \sigma_v \frac{T^2}{R} p_s\left(t - \frac{2l}{c_s}\right)\exp(-2k_e l)dl.$$

The received volume-scattering power from the depth range $0 \rightarrow L$ is

$$p_v(t) = \int_0^L dp_v(t,l)$$

whence

$$p_v(t) = A'' \int_0^L p_s\left(t - \frac{2l}{c_s}\right)\exp(-2k_e l)dl$$

where $A'' = \sigma_v \frac{T^2}{R}$. The depth of penetration is defined as $1/k_e$.

COMBINED MODEL

The combined surface-scattering and volume-scattering model is

$$p^*(n) = \varepsilon + B\,[(1 - v_b)\,p_s(n)/p_{s_{max}} + v_b p_v(n)/p_{v_{max}}]$$

in which ε is the noise level, v_b is the proportion of volume-scattering ($0 \le v_b \le 1$), B is an amplitude coefficient adjusted to make $p^*(n)$ fit the observed waveform, n is the range bin (gate) number, $p^*(n)$ is the modeled power, $p_{s_{max}}$ is the maximum value of $p_s(n)$ for the particular waveform, and $p_{v_{max}}$ is the corresponding maximum value of $p_v(n)$. By taking the power ratios, the effects of A' and A'' were eliminated. The normalized powers $p_s(n)/p_{s_{max}}$ and $p_v(n)/p_{v_{max}}$ are used because the

absolute value of the surface-scattering power and the volume-scattering power were both unknown. The two powers were normalized so that the shapes of the two powers can be used to determine the contribution of each to the combined waveform through fitting the combined waveform to the observed waveform.

Davis and Zwally's (1993) model does not include the pointing angle or the earth curvature. They include an artificial weighting function in their model that probably weights the leading edge of the waveform more than the trailing part, like the weighting function used in NASA's model (Zwally et al. 1990). This probably helps to compensate in their method for not considering the pointing angle and the earth curvature. The inclusion of a constant pointing angle and the earth curvature in our model makes a weighting function unnecessary. Although adding the earth curvature removes a known error source, adding a constant pointing angle can only improve the result in an average sense. However, when we know the surface topography or satellite pointing better, further improvement can be made by applying this model. Figure 1 shows an example of how the two factors affect the surface scattering model. Without considering the two factors, the trailing part of the power will be underestimated; hence, the model parameter will be affected.

MODEL APPLICATION

A nonlinear-least-square fitting method was used to fit the model to the radar-altimeter waveforms over East Antarctica. Five steps were followed during the fitting process:

1. Assume an initial estimate for the unknown model parameters.
2. Obtain a first-order Taylor series expansion around the initial estimated values.
3. Find the least-square solution for the correction to the initial estimated values.
4. Use the revised parameter values for a new estimate.
5. Repeat steps 2, 3, and 4 until some exit criterion is satisfied.

Because the problem is nonlinear, the procedure can be numerically unstable. A record will be discarded if it does not converge after 15 iterations.

Four parameters of interest were calculated: 1) the extinction coefficient, which reflects the grain size and density of snow and therefore is affected by the accumulation rate, temperature, and wind; 2) the proportion of volume scattering, which describes the relative contribution of volume scattering to the waveform amplitude; 3) the surface roughness, which describes the variation of surface height within the altimeter footprint; and 4) the elevation difference, which shows the difference between this retracking model and NASA's (Zwally et al. 1990) retracking model.

The model has been applied to the section of East Antarctica bounded by 80°E, 140°E, 69°S, and 72.1°S. We chose latitudes between 69°S and 72.1°S because the highest latitudes (Geosat coverage extended to 72.1°S) contains the densest measurements and because the surface in that band is smoother than at lower latitudes so the waveforms are better behaved. The data used were from the Geosat Exact Repeat Mission between November 1986 and September 1989. To detect regional and seasonal changes, the region was divided into cells measuring 0.5° or 0.6° of latitude by 1° of longitude between 71°S and 72.1°S and into 1° by 1° cells between 69°S and 71°S. A surface elevation map taken from Zwally et al. (1983) that covers the study region is shown in Figure 2. Figure 3 shows examples of observed waveforms and corresponding modeled waveforms and maps of the four parameters over the region are shown in Figure 4.

RESULTS

There is no apparent relationship between elevation and any of the four parameters. The extinction coefficient values acquired here are similar to the value, 0.14 m^{-1}, measured by Hofer and Matzler (1980) on cold Alpine snow. The elevation difference is strongly correlated with the proportion of volume scattering: higher elevation differences correspond to higher proportions of volume scattering (Fig. 5); the correlation coefficient between the two is 0.89. Temporal changes in the proportion of volume scattering are shown in Figure 6; seasonal variations clearly show from 80°E to 95°E but are not very clear from 96°E to 140°E.

Davis and Zwally (1993) found that the extinction coefficient decreases as elevation increases on a smaller section (71.5°S–72.1°S and 80°E–94°E) of East Antarctica, but over the larger area considered here the correlation disappears.

An automatic gain control (AGC) loop was implemented in the altimeter to maintain a constant output level and to ensure operation of all receiver stages within the linear region. A digital attenuator in the receiver provides for a gain varia-

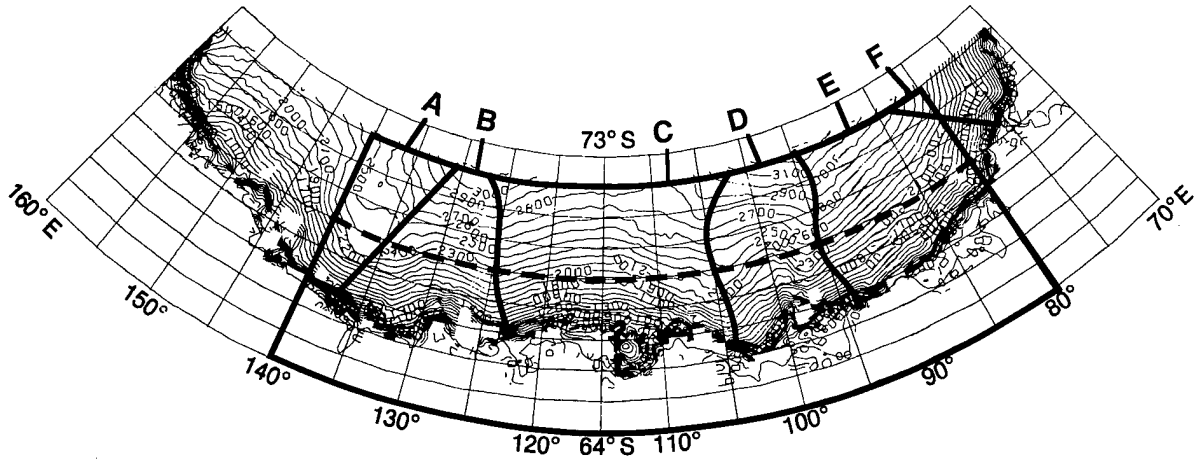

Figure 2. Map of a part of East Antarctica that includes our study area (69°S–72.1°S and 80°E–140E). The map with surface contours is from Zwally et al. (1983). Latitude and longitude are in degrees south and east, respectively. The ice divides were added by Bentley and Sheehan (1992).

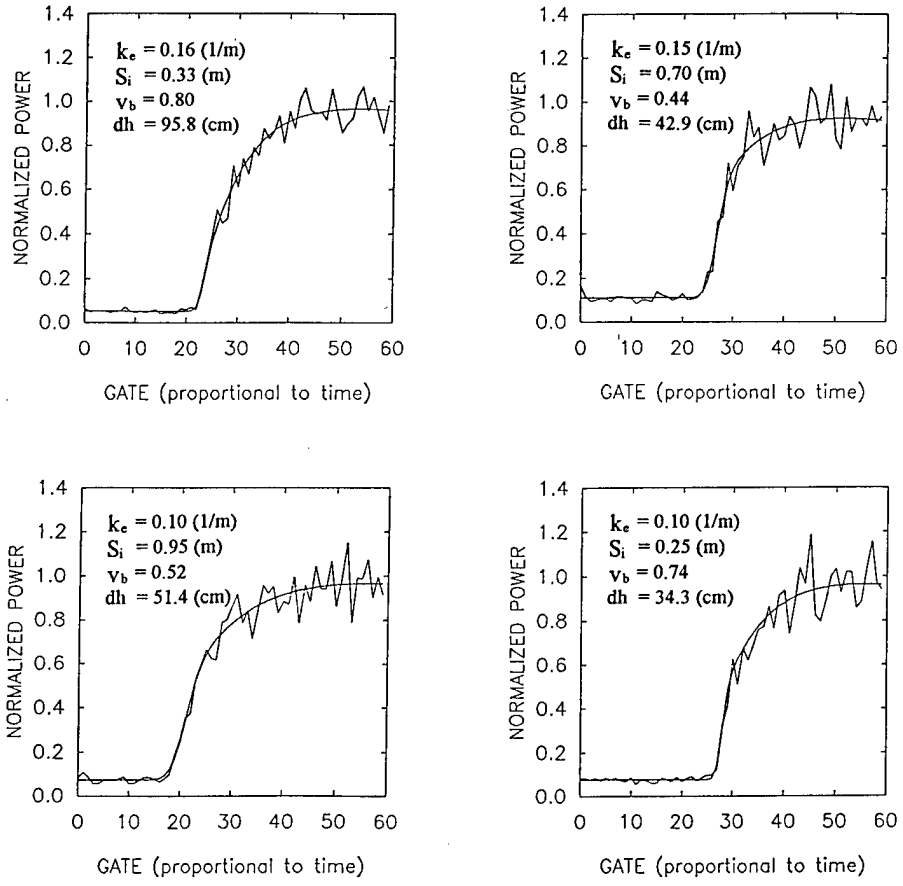

Figure 3. Sample waveforms (jagged lines) together with the fitted model curves (smooth lines). The parameters that correspond to each waveform are listed in each plot.

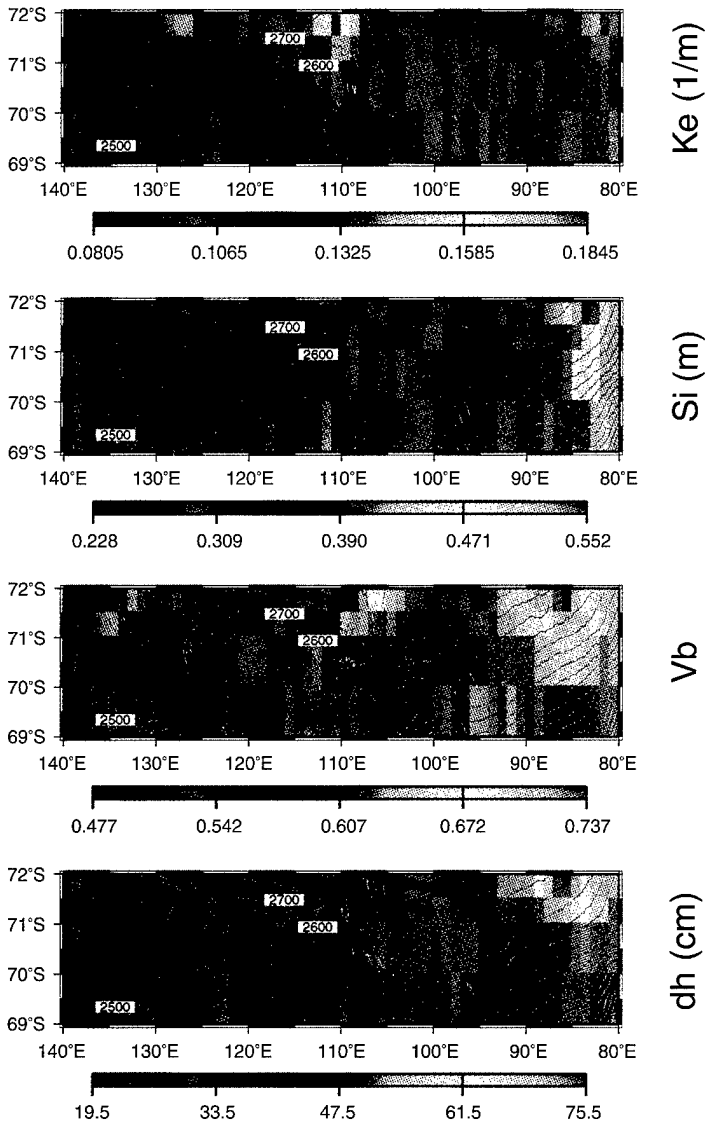

Figure 4. Thirty-five-month-mean parameters in each cell (0.5°, 0.6° or 1.0° of latitude by 1.0° of longitude). The spatial variations of the parameters are clearly shown in these maps. The contour lines are surface elevations.

tion of 0–63 dB. The AGC values provide a very good estimate of the return signal strength. Figure 7 shows the variation of AGC value with longitude. From 80°E to 98°E, the AGC value decreases as the extinction coefficient decreases. This is similar to the result described by Davis and Zwally (1993) from a comparison of waveform amplitudes with extinction coefficients in the same region. However, the correlation does not extend over the entire region. Our results show, therefore, that variations in neither the extinction coefficient nor the AGC over a large region correlates in a simple way with surface elevation.

Katabatic winds, which are gravity driven and so are directed down the steepest slopes, might be expected to affect grain size and the surface roughness and hence the AGC. Comparing the AGC value with the katabatic wind (Parish and Bromwich 1987), we find that large AGC values correspond to small wind speeds, while small

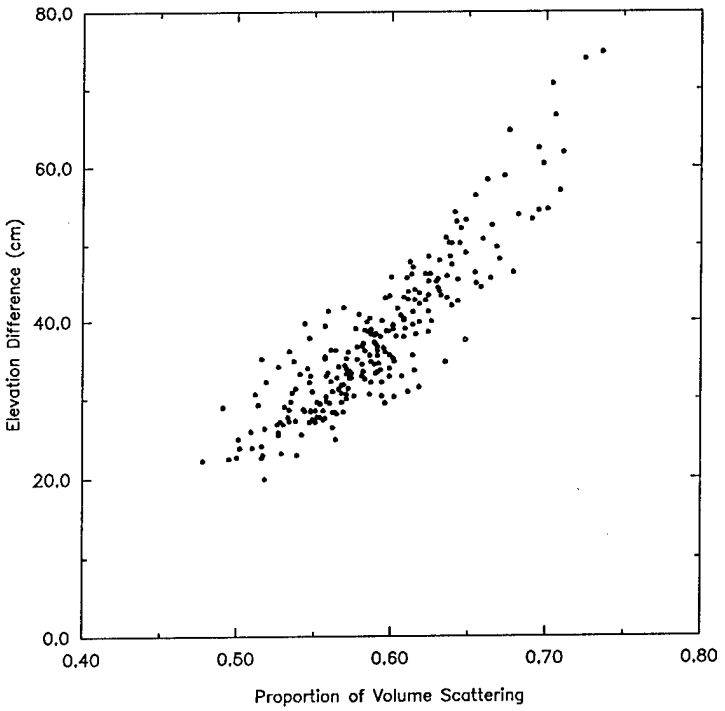

Figure 5. Thirty-five-month-mean proportion of volume scattering vs. elevation difference for 240 cell values in Figure 4. The correlation coefficient between the two is 0.89.

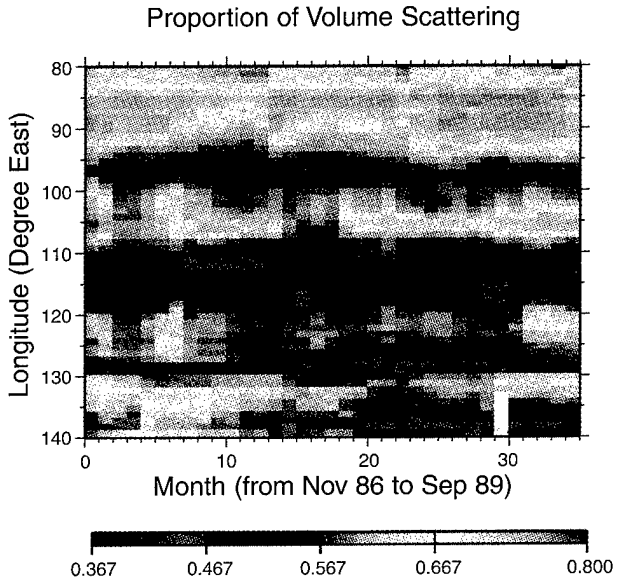

Figure 6. The proportion of volume scattering (v_b) averaged over each month and over cells measuring 0.6° latitude (71.5°S– 72.1°S) by 1.0° longitude (the top row of cells in Figure 4). The mean v_b values are plotted as a function of longitude (ordinate) and calendar month (abscissa). Clearly the spatial variations are stronger than the seasonal variations.

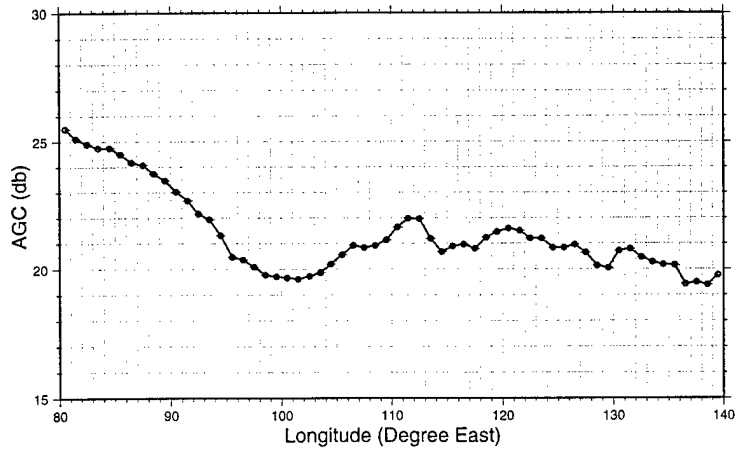

Figure 7. Thirty-five-month-mean AGC values as a function of longitude. The cells are the same as in Figure 6 (the top row of cells in Figure 4).

AGC values correspond to large wind speeds. This agrees with the result of Remy et al. (1990) that AGC is correlated with katabatic wind intensity, although our AGC value distribution and theirs are slightly different. That difference may arise because Remy et al. (1990) used only Seasat data, which lasted only 100 days. However, when we compare our data with a katabatic wind map published later by the same authors (Parish and Bromwich 1991), the correlation disappears. The reason for this may be that the katabatic wind was calculated from an elevation input with a larger grid size in the latter paper than in the former. The lack of detailed surface elevation input makes it difficult to resolve confluence features under 200 km in linear dimension (Parish and Bromwich 1991). Without a katabatic wind model based on detailed elevations, it is very difficult to make a good comparison.

CONCLUSION

Both surface scattering and volume scattering are important in the dry snow region. Their contributions to the returned power are of the same order of magnitude. Models that neglect either one of them will introduce bias in the results.

ACKNOWLEDGMENTS

This work was supported by NASA grant NAGW-1773. We wish to thank Anita C. Brenner and John DiMarzio at Hughes-STX for providing the GEOSAT ERM data. We also wish to thank Sion Shabtaie and Mark D. Stenoien at University of Wisconsin-Madison for the useful discussions.

LITERATURE CITED

Bentley, C.R. and D.D. Sheehan (1992) Comparison of altimetry profiles over East Antarctic from Seasat and Geosat, an interim report. *Z. Gletscherkd, Glazialgeol.*, **26**(1): 1–9.

Brooks, R.L., W.J. Campbell, R.O. Ramseier, H.R. Stanley and H.J. Zwally (1978) Ice sheet topography by satellite altimetry. *Nature*, **274**(5671): 539–543.

Brown, G.S. (1977) The average impulse response of a rough surface and its applications. *IEEE Trans. Antennas Prop.*, **AP-25**(1): 67–73.

Davis, C.H. and R.K. Moore (1993) A combined surface and volume-scattering model for ice-sheet radar altimetry. *Journal of Glaciology*, **39**(133): 675–686.

Davis, C.H. and H.J. Zwally (1993) Geophysical and seasonal variations in the surface properties of the ice sheets by satellite-radar altimetry. *Journal of Glaciology*, **39**(133): 687–697.

Hofer, R. and C. Matzler (1980) Investigations on snow parameters by radiometry in the 3- to 60-mm wavelength region. *Journal of Geophysical Research*, **85**(c1): 453–460.

Martin, T.V., H.J. Zwally, A.C. Brenner and R.A. Bindschadler (1983) Analysis and retracking of continental ice sheet radar altimeter wave-forms.

Journal of Geophysical Research, **88**(c3): 1608–1616.
Parish, T.R. and D.H. Bromwich (1987) The surface wind field over the Antarctic ice sheets. *Nature,* **328:** 51–54.
Parish, T.R. and D.H. Bromwich (1991) Continental scale simulation of the Antarctic katabatic wind regime. *Journal of Climate,* **4:** 135–146.
Partington, K.C., W. Cudlip, N.F. McIntyre and S. King-Hele (1987) Mapping of Amery Ice Shelf, Antarctica, surface features by satellite altimetry. *Annals of Glaciology,* **9:** 183–188.
Remy, F., C. Brossier and J.F. Minster (1990) Intensity of satellite radar-altimeter return power over continental ice: a potential measurement of katabatic wind intensity. *Journal of Glaciology,* **36**(123): 133–142.
Ridley, J.K. and K.C. Partington (1988) A model of satellite radar altimeter return from ice sheets. *International Journal of Remote Sensing,* **9**(4): 601–624.
Rodriguez, E. (1988) Altimeter from non-Gaussian ocean: height biases and estimation of parameters. *Journal of Geophysical Research,* **93**(c11): 14,107–14,120.
Thomas. R.H., T.V. Martin and H.J. Zwally (1983) Mapping ice-sheet margin from radar altimetry data. *Annals of Glaciology,* **4:** 283–288.
Yi, D. and C.R. Bentley (1994) Analysis of satellite radar-altimeter return wave forms over the East Antarctic ice sheet. *Annals of Glaciology,* **20:** 137–142.
Zwally, H.J., R.A. Bindschadler, A.C. Brenner, T.V. Martin and R.H. Thomas (1983) Surface elevation contours of Greenland and Antarctic ice sheets. *J. Geophys. Res.,* **88**(c3): 1589–1596.
Zwally, H.J., S.N. Stephenson, R.A. Bindschadler and R.H. Thomas (1987) Antarctic ice-shelf boundaries and elevations from satellite radar altimetry. *Annals of Glaciology,* **9:** 229–235.
Zwally, H.J., A. C. Brenner, J.A. Major, R.A. Bindschadler and J.G. Marsh (1989) Growth of Greenland ice sheet: Measurement. *Science,* **246**(4937): 1587–1589.
Zwally, H.J., A. C. Brenner, J.A. Major, T.V. Martin and R.A. Bindschadler (1990) Satellite radar altimetry over ice. Vol. 1, Processing and corrections of Seasat data over Greenland. Washington, DC: National Aeronautics and Space Administration. (NASA Ref. Publ. 1233, 1.)

REPORT DOCUMENTATION PAGE

Form Approved
OMB No. 0704-0188

1. AGENCY USE ONLY (Leave blank)	2. REPORT DATE	3. REPORT TYPE AND DATES COVERED
	October 1996	

4. TITLE AND SUBTITLE
Glaciers, Ice Sheets and Volcanoes:
A Tribute To Mark F. Meier

5. FUNDING NUMBERS

6. AUTHORS
Samuel C. Colbeck

7. PERFORMING ORGANIZATION NAME(S) AND ADDRESS(ES)

8. PERFORMING ORGANIZATION REPORT NUMBER
Special Report 96-27

9. SPONSORING/MONITORING AGENCY NAME(S) AND ADDRESS(ES)

U.S. Army Cold Regions Research and Engineering Laboratory
72 Lyme Road
Hanover, New Hampshire 03755-1290

10. SPONSORING/MONITORING AGENCY REPORT NUMBER

11. SUPPLEMENTARY NOTES

12a. DISTRIBUTION/AVAILABILITY STATEMENT
Approved for public release; distribution is unlimited.
Available from NTIS, Springfield, Virginia 22161

12b. DISTRIBUTION CODE

13. ABSTRACT (*Maximum 200 words*)

This volume is dedicated to the professional contributions of Mark Meier. It contains a mixture of papers on snow, glaciers, ice sheets and volcanoes, and therefore reflects his interests and research contributions. The papers were presented at the 1995 Fall meeting of the American Geophysical Union.

14. SUBJECT TERMS
Glaciers, Ice, Snow, Glaciology, Ice sheets, Volcanoes

15. NUMBER OF PAGES
132

16. PRICE CODE

17. SECURITY CLASSIFICATION OF REPORT	18. SECURITY CLASSIFICATION OF THIS PAGE	19. SECURITY CLASSIFICATION OF ABSTRACT	20. LIMITATION OF ABSTRACT
UNCLASSIFIED	UNCLASSIFIED	UNCLASSIFIED	UL